DISSERTATION

BIO-INSPIRED DESIGN FOR ENGINEERING APPLICATIONS: EMPIRICAL AND FINITE ELEMENT STUDIES OF BIOMECHANICALLY ADAPTED POROUS BONE ARCHITECTURES

Submitted by

Trevor Gabriel Aguirre

Department of Mechanical Engineering

In partial fulfillment of the requirements

For the Degree of Doctor of Philosophy

Colorado State University

Fort Collins, Colorado

Summer 2020

Doctoral Committee:

Advisor: Seth W. Donahue

Kaka Ma
Paul Heyliger
Steven Simske

ABSTRACT

BIO-INSPIRED DESIGN FOR ENGINEERING APPLICATIONS: EMPIRICAL AND FINITE ELEMENT STUDIES OF BIOMECHANICALLY ADAPTED POROUS BONE ARCHITECTURES

Trabecular bone is a porous, lightweight material structure found in the bones of mammals, birds, and reptiles. Trabecular bone continually remodels itself to maintain lightweight, mechanical competence, and to repair accumulated damage. The remodeling process can adjust trabecular bone architecture to meet the changing mechanical demands of a bone due to changes in physical activity such as running, walking, etc. It has previously been suggested that bone adapted to extreme mechanical environments, with unique trabecular architectures, could have implications for various bioinspired engineering applications. The present study investigated porous bone architecture for two examples of extreme mechanical loading.

Dinosaurs were exceptionally large animals whose body mass placed massive gravitational loads on their skeleton. Previous studies investigated dinosaurian bone strength and biomechanics, but the relationships between dinosaurian trabecular bone architecture and mechanical behavior has not been studied. In this study, trabecular bone samples from the distal femur and proximal tibia of dinosaurs ranging in body mass from 23-8,000 kg were investigated. The trabecular architecture was quantified from micro-computed tomography scans and allometric scaling relationships were used to determine how the trabecular bone architectural indices changed with body mass. Trabecular bone mechanical behavior was investigated by finite element modeling. It was found that dinosaurian trabecular bone volume fraction is positively correlated with body mass

like what is observed for extant mammalian species, while trabecular spacing, number, and connectivity density in dinosaurs is negatively correlated with body mass, exhibiting opposite behavior from extant mammals. Furthermore, it was found that trabecular bone apparent modulus is positively correlated with body mass in dinosaurian species, while no correlation was observed for mammalian species. Additionally, trabecular bone tensile and compressive principal strains were not correlated with body mass in mammalian or dinosaurian species. Trabecular bone apparent modulus was positively correlated with trabecular spacing in mammals and positively correlated with connectivity density in dinosaurs, but these differential architectural effects on trabecular bone apparent modulus limit average trabecular bone tissue strains to below 3,000 microstrain for estimated high levels of physiological loading in both mammals and dinosaurs.

Rocky Mountain bighorn sheep rams (*Ovis canadensis canadensis*) routinely conduct intraspecific combat where high energy cranial impacts are experienced. Previous studies have estimated cranial impact forces up to 3,400 N and yet the rams observationally experience no long-term damage. Prior finite element studies of bighorn sheep ramming have shown that the horn reduces brain cavity translational accelerations and the bony horncore stores 3x more strain energy than the horn during impact. These previous findings have yet to be applied to applications where impact force reduction is needed, such as helmets and athletic footwear. In this study, the velar architecture was mimicked and tested to determine suitability as novel material architecture for running shoe midsoles. It was found that velar bone mimics reduce impact force ($p < 0.001$) and higher energy storage during impact ($p < 0.001$) and compression ($p < 0.001$) as compared to traditional midsole architectures. Furthermore, a quadratic relationship ($p < 0.001$) was discovered between impact force and stiffness in the velar bone mimics. These findings have implications for the design of novel material architectures with optimal stiffness for minimizing impact force.

ACKNOWLEDGEMENTS

1.1 Professional Acknowledgements

The author thanks Dr. Peter Bishop at the Royal Veterinary College (London, England, UK) for his assistance in procuring CT scans of *Troodon*, Caenagnathid, Ornithomimid, and *Falcarius utahensis*.

The author thanks Dr. Don Henderson and Mr. Brandon Strilisky at the Royal Tyrrell Museum of Palaeontology (Drumheller, Alberta, CA) for allowing access to their Caenagnathid (TMP 1986.036.0323) and Ornithomimid (TMP 1999.055.0337) specimen CT scans.

The author also thanks Dr. John Scannella and Ms. Amy Atwater at the Museum of the Rockies at Montana State University and the land management agencies from whose land the specimens were collected, for allowing access of their Troodontid (MOR 748) specimen CT scans.

Courtesy of Natural History Museum of Utah, UMNH VP 12360, the authors thank Dr. Randall B. Irmis at the Natural History Museum of Utah for allowing us access to their *Falcarius utahensis* specimen CT scans.

The author thanks Dr. Laura Vietti and Dr. Mark Clementz in the Geology and Geophysics Department at the University of Wyoming for allowing us to collect trabecular cores from their *Camarasaurus* (UW20519) and *Apatosaurus* (UW20501) specimens.

The author thanks Ms. Jessica Lippincott and Mr. William Wahl at the Wyoming Dinosaur Center for allowing us to collect a sample from their *Supersaurus* specimen, Jimbo (WYDICE DMJ-0021 05).

The author thanks Dr. Marieka Arksey in the Department of Anthropology at the University of Wyoming and the University of Wyoming Archaeological Repository for allowing us to collect the *Mammuthus columbi* specimen sample (48WA322-9). Additionally, the authors

thank Ms. Rebecca Brower at the Washakie Museum in Worland Wyoming for coordinating with the authors to collect a sample from the mammoth fossil.

Specimens sampled at the Denver Museum of Nature & Science are part of the Hankla Family Collection, generously donated for the preservation and promotion of science.

The authors thank Dr. Ann Hess in the Department of Statistics at Colorado State University for her assistance with statistical methods utilized in this study.

The author thanks two scientists from Oak Ridge National Laboratory, Dr. Corson L. Cramer and Dr. Amy M. Elliott, for facilitating the optical microscopy, scanning electron microscopy, and energy dispersive x-spectroscopy analyses of the *Diplodocus*, *Apatosaurus*, and *Camarasaurus* specimen during my ASTRO program tenure at Oak Ridge National Laboratory.

The author thanks Steve Johnson in the Mechanical Engineering Department at Colorado State University for design assistance, manufacturing the mobile core drilling device used in this study, and helping collect the trabecular cores from the fossils previously mentioned.

The author thanks the State of Colorado Department of Natural Resources for providing the Scientific collection license for the bighorn sheep material.

The author thanks Dr. Karen Fox from Colorado Parks and Wildlife and Drs. Susan Kraft and Angela J. Marolf at the Colorado State University Veterinary Teaching Hospital for allowing us access to the CT scanner to image the bighorn sheep used in this study.

The author also thanks Dr. Christopher Weinberger in the Colorado State University Mechanical Engineering Department for his input on modeling techniques utilized in this study.

1.2 Personal Acknowledgements

There are numerous people who have provided mentorship, physical, mental, and, emotional support during my life whose efforts and time are not forgotten. The individuals listed below are the few that I would like to thank personally.

I give thanks to my advisor, Dr. Seth Donahue, for taking me as a student and for the mentorship and guidance he provided over the last 3 years. I know it wasn't easy at times and I thank you for helping me develop as a scientist and engineer.

Thank you to my committee members, Dr. Kaka Ma, Dr. Steven Simkse, and Dr. Paul Heyliger. I appreciate your feedback, time, and guidance. Dr. Susan James, thank you for helping manage the grant that funded my research, for serving on my qualifying exam committee, and your guidance outside of this project. In addition, I would like to thank my lab-colleagues Dr. Samantha Wojda, Timothy Seek, Emily Mulawa, Luca Fuller, and Dr. Aniket Ingrole for all assistance during my research. I would like to also acknowledge Dr. Benjamin Wheatley at Bucknell University for all his assistance during this project.

I thank my family and friends, for the support over the last 12 years of my education. Your support over the years has meant the world to me.

I would like to thank my high school maths teacher for not believing in me. You were very outspoken about how I had neither the motivation nor skills, needed to finish an associate's degree. Because of your doubt I would like to say thank you. For the number of years that I was extrinsically motivated your doubt pushed me to study more, learn more, and ultimately successfully earn two associates', a bachelor's, a master's, and doctoral degrees.

To my pre-school teacher, Marietta West, thank you for reminding me where my education started and thus allowing me to realize how far I have come. "Wow, you're earning a PhD, and to

think you learned how to read in the little yellow schoolhouse down the street!" This simple sentence helped me, for the first time, to be truly proud of my accomplishments.

Thank you to my high school physics teacher, Dr. Lori Miller, for recognizing my abilities in maths and science. I appreciate you allowing me to explore and experiment in in your lab and I apologize for all the things I broke when I was learning about circuitry. (Turns out I was an experimentalist before I knew what that word meant). Without your encouragement I would not have studied engineering and would not be here today. I wish I could have told you this in person. May you rest in peace.

Last, and far from the least, I thank my mother, Yvette Aguirre. Thank you for everything. Most importantly, for not letting me quit. When my father passed, and the hospital bills were beginning to pile up you were unsure how you were going to pay them. My plan was to drop out of school to get a job so I could help you pay them. Your plan was different, and quitting was not something you would allow me to do. In 2010, before I had finished my associates' degree, you convinced me to continue my education. Life would have been very different if that conversation would not have occurred. Thank you for not letting me quit. Thank you for telling me you are proud me. Thank you for being there for me when I needed you, thank you for helping me even when it was difficult for you to do so, and most of all thank you for believing in me. Without your support and belief, I do not think I would have made it this far and some days that belief is the only thing that helped me continue.

TABLE OF CONTENTS

Chapter 1: Introduction: Trabecular architecture in large mass animals

1.1 Trabecular bone

Trabecular bone is a porous, strong, stiff, and lightweight structure. Trabecular bone is composed of a network of highly interconnected beam-like struts and is found in the ends of long bones, vertebrae, and between the dense outer and inner layers of the skull [1] and is shown in Figure 1-1.

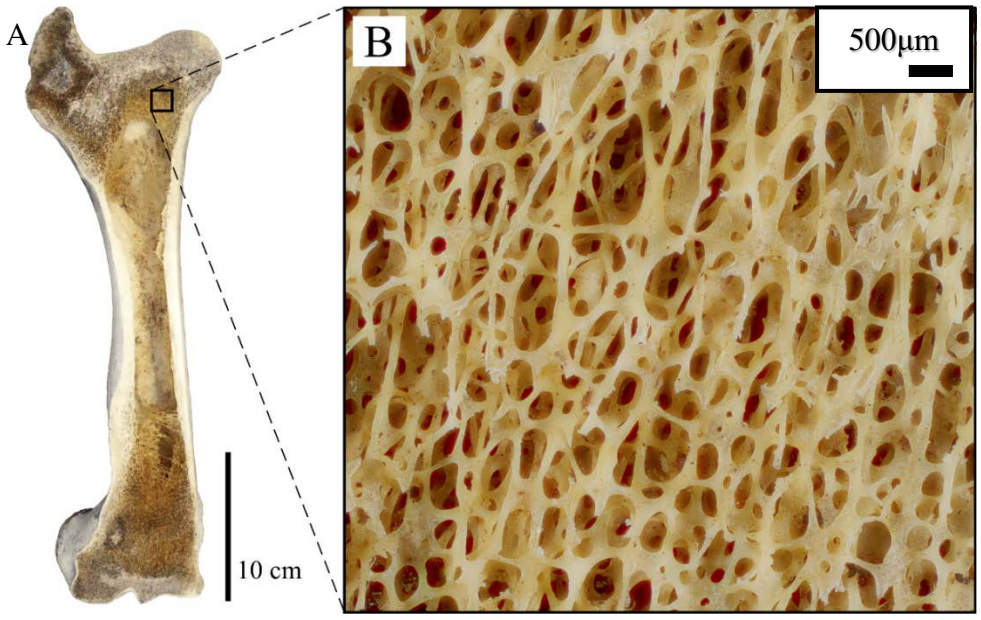

Figure 1-1: A) Femoral trabecular bone with a close up shown in B). Image adapted from [2]

Trabecular bone is adapted to the mechanical needs of the whole bone, where there is evidence showing the individual trabecula are oriented in the directions of the principal stresses [3], [4]. Bones need to be sufficiently strong and tough enough to resist fracture for habitual physical activity. It is known that bones have different mineral content to optimize strength and toughness needed for the loading condition of the bone [1]. However, the cellular maintenance (e.g., bone remodeling) and transport (e.g., during locomotion) of bone is metabolically expensive. Thus, bony architecture must achieve mechanical competence while maintaining light weight. If

an individual bone was so large that the mechanical strains were low during routine activities such as walking and running, then the animal would expend unnecessary energy to move an unnecessarily heavy skeleton during these activities. However, if mechanical loading becomes too large the risk of failure increases [5], [6].

The physiological process of bone remodeling helps achieve a balance between bone weight and mechanical competence, and repairs and limits the accumulation of fatigue damage [7]. The remodeling process consists of the coordinated resorption and formation of the boney material due the response of mechanical forces. This resorption happens at the microstructural level where osteoclasts destroy unneeded tissue and osteoblasts rebuild the new trabecular structure [4]. However, this remodeling comes at a metabolic cost and the energy needed for remodeling must be prioritized based on the availability of fuel to drive the remodeling process [8]. Therefore, it is been suggested that bone has a highly optimized structure to meet mechanical demands and while maintaining lightweight [9].

1.2 Trabecular bone architectural indices

To assess trabecular architecture several indices have been established [10]. Bone volume fraction (BV/TV) is defined as the bone volume (BV) normalized by the total volume (TV) of the region of interest (ROI). The trabecular thickness (Tb.Th) is the average thickness of all trabeculae within the ROI. Similarly, trabecular spacing (Tb.Sp) is the average linear distance between trabeculae within the ROI. The trabecular number (Tb.N) is the number of trabecular intersections per unit line length and connectivity density (Conn.D) is the number of connected structures in the ROI divided by the total volume (TV). Examples of the structural indices are shown in Figure 1-2. Changes in these indices have been associated with changes in trabecular strength [4].

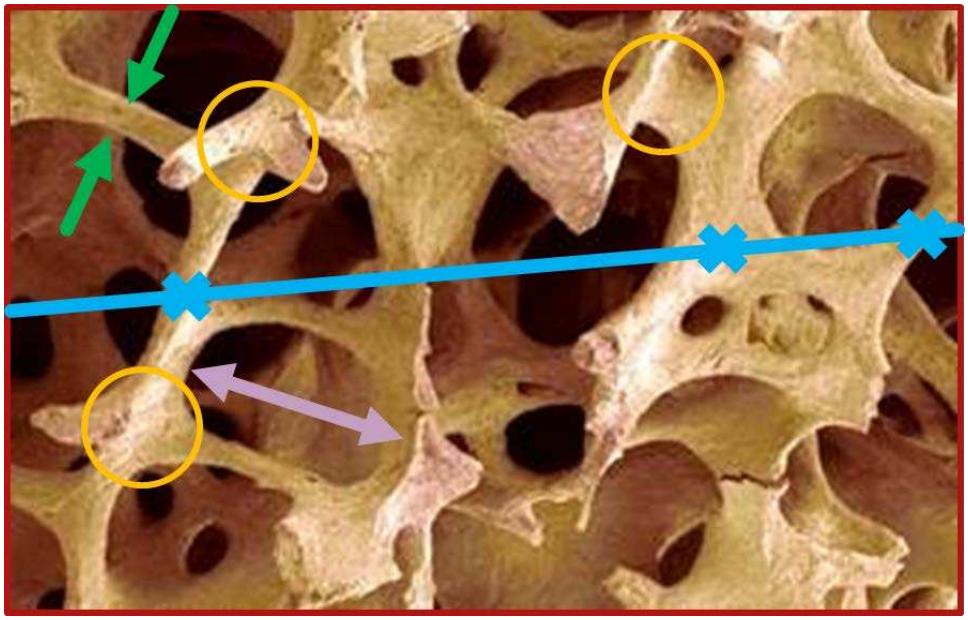

Figure 1-2: Trabecular bone architectural indices: trabecular thickness, Tb.Th (green arrows), trabecular separation, Tb.Sp (purple arrow), trabecular number, Tb.N (blue lines and crosses), TV (red square), and Conn.D (orange circles)

1.3 Allometric scaling

Allometry is the study of the relationship of body size to shape, anatomy, physiology, and behavior. One study [11] has shown that trabecular bone architectural indices in the femoral head and lateral condyles scale with increasing femoral head radius in mammalian, avian, and reptilian species. At the time of the study the body mass of each specimen was not known so femoral head radius was used as a surrogate for body mass. In that study the trabecular bone structural indices in the femoral head and the lateral femoral condyle were quantified for 72 terrestrial mammals, 18 birds, and 1 crocodile, spanning six-orders of magnitude of body mass ranging from 3 grams to 3 tonnes. A full list of these species can be found at [12]. This study showed that there was no significant correlation with the bone volume fraction and increasing femoral head radius, positive correlations for both trabecular spacing and trabecular thickness with increasing femoral head radius, and negative correlation between connectivity density and increasing femoral head radius (Figure 1-3).

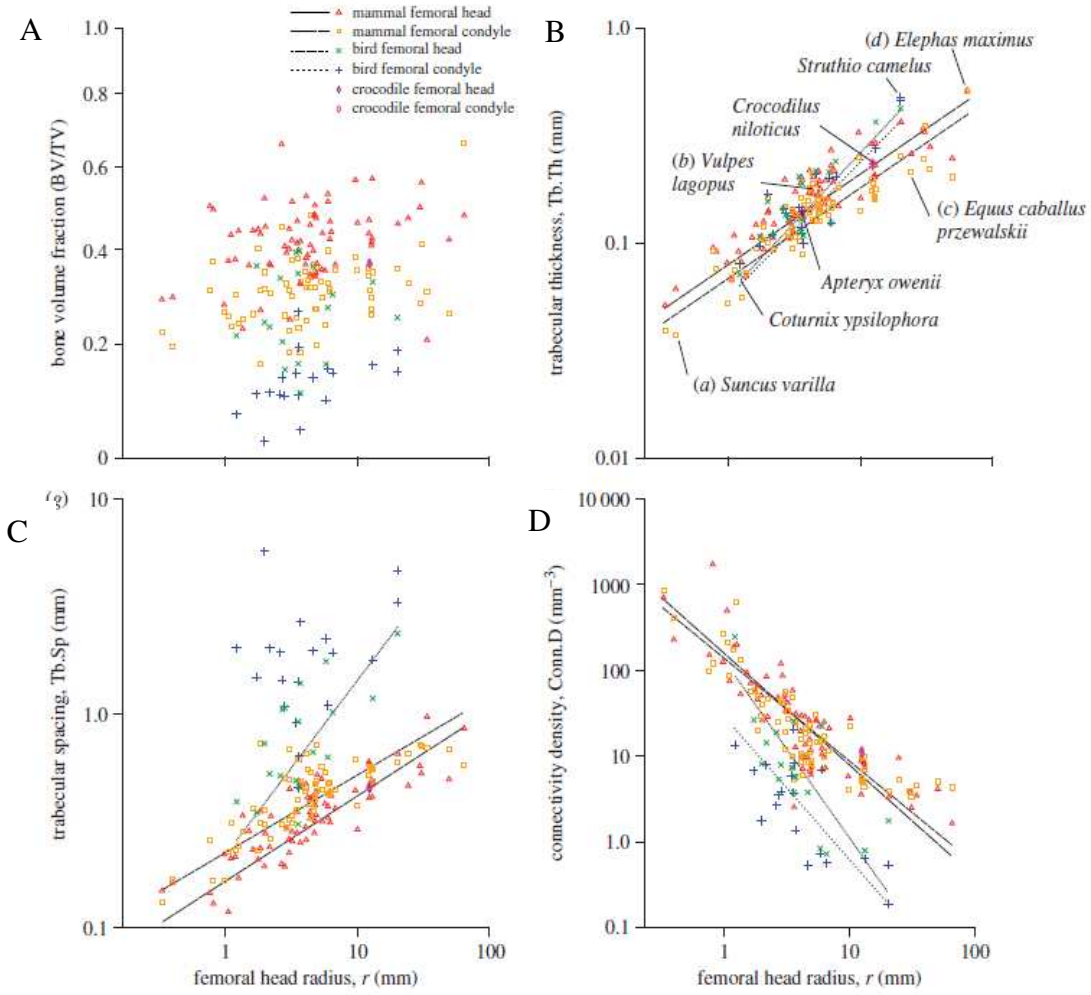

Figure 1-3: Double logarithmic plots of A) bone volume fraction, B) trabecular thickness, C) trabecular spacing, and d) Connectivity versus increasing femoral head radius. Image adapted from [11]

A similar study [13] investigated how the structural indices of trabecular bone scaled with body mass in various mammalian bones. In this study trabecular bone from the mandibular condyle, humerus, radius, metacarpal bones, vertebrae, femur, iliac crest, tibia, and calcaneus for 12 different species were analyzed. The study showed weak but significant negative correlation between body mass and trabecular number and connectivity density and positive correlation between trabecular spacing and trabecular thickness. There was no correlation between body mass and bone volume fraction Figure 1-4.

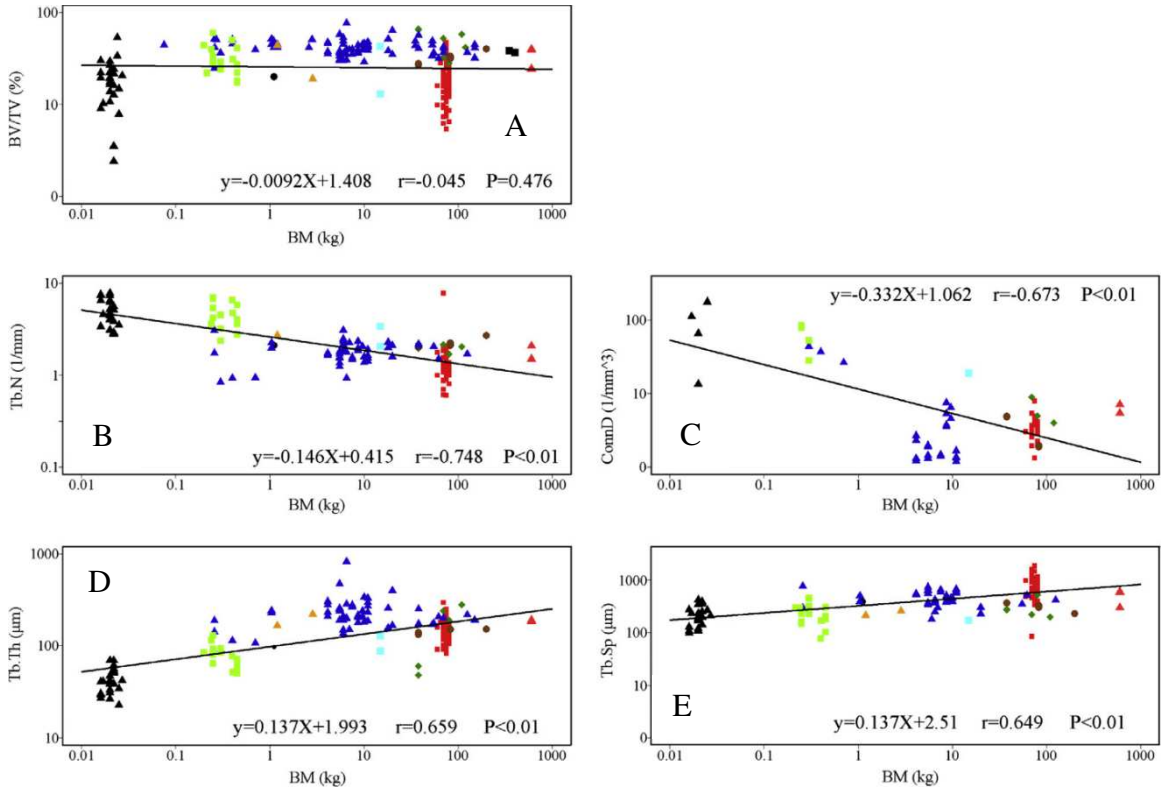

Figure 1-4: Double logarithmic plots of A) bone volume fraction, B) trabecular number, C) connectivity density, D) trabecular thickness, and E) trabecular spacing versus increasing body mass. Image adapted from [13]

Synthesizing the results of these studies [11], [13] show that there are significant relationships between the trabecular bone architectural indices and increasing body mass. This is important because trabecular bone mechanical properties are heavily dependent on architecture. Bone strength decreases with age due to decreased trabecular number, trabecular thickness, and connectivity density [14]–[16]. Furthermore, the lack of correlation between bone volume fraction and body mass is interesting to because bone strength decreases with decreasing volume fraction [17].

1.4 Mechanics of cellular solids

A cellular material is define is a porous body composed of repeatable units (or cells) that are used to build a structure [17]. Cellular materials can be open- or closed-cell. Examples of cellular materials include the honeycomb structure in cork, the foam structure found between external layers of plant leaves, the interior of porcupine quills, and trabecular bone. The mechanical response of these materials is heavily dependent on the cell shape and the volume fraction of these structures where any measured property (mechanical/thermal/electrical) decreases quadratically or cubically with decreased volume fraction [17]. Figure 1-5 shows how trabecular bone apparent elastic modulus decreases with decreasing volume fraction.

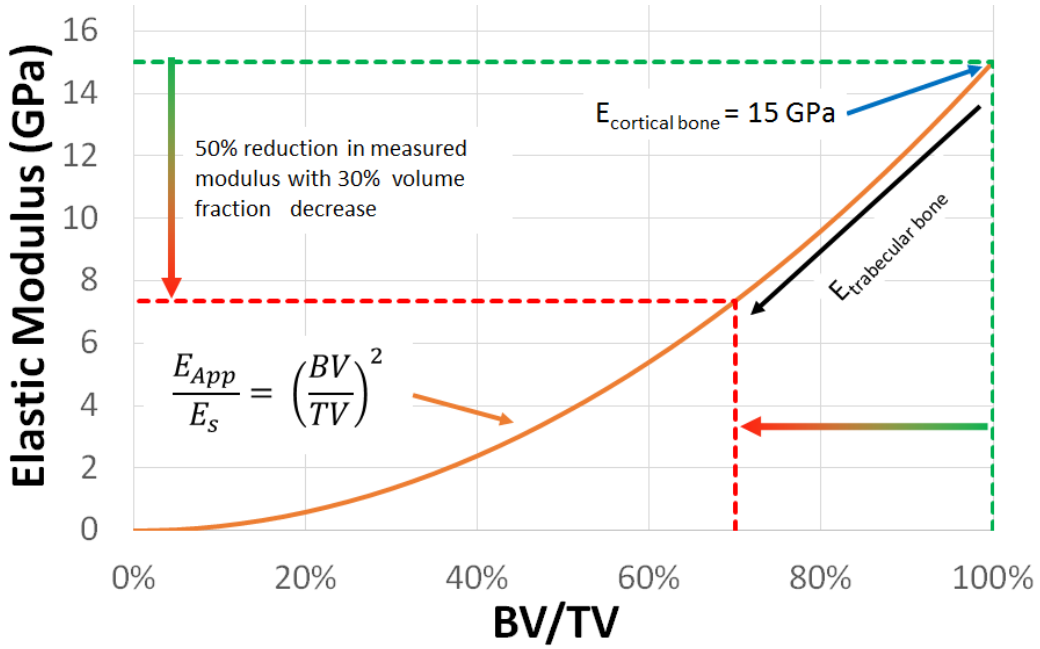

Figure 1-5: Measured apparent elastic modulus versus volume fraction

Shown in Figure 1-5 is the governing equation for elastic modulus with decreasing or increasing volume fraction. In this equation E_{App} is the apparent elastic modulus measured from stress strain curve measured on the porous body, E_s is the elastic modulus of the solid, i.e. the

material that the porous body is made from, and BV/TV is the volume fraction. Deformation in open cell foams is primarily due to bending of the cell edges. Applying this to trabecular bone it been previously observed that the strength of trabecular bone is not only dependent on bone volume fraction but also the trabecular architecture. [18], [19]. The primary cause for decreases in bone volume fraction are attributed to decreases in trabecular thickness [14]. Finite element studies have shown that decreasing trabecular number has been shown to cause between a 2 to a 5 fold reduction in bone strength [20] and strength increases have been observed with increasing connectivity density [19], [21].

1.5 Finite element modeling and trabecular bone risk assessment

Finite element modeling is technique where solutions to the equations governing a physical process are numerically approximated [22]. Finite element modeling has countless applications in engineering including thermal analysis [23], fluid dynamics [24], and solid mechanics [25]. Finite element modeling is most useful when equation solutions are difficult/impossible to obtain and has been a useful tool for understanding the mechanics of trabecular bone [26], [27], [27]–[31], where failure of risk of important concern. Failure risk is typically assed using a multi-axial failure theory, where failure is the onset of yielding [32]. The distortion energy theory has been used with finite element models to predict failure fracture in the proximal femur [33]. Though failure was accurately predicted, the distortion energy theory does not account for trabecular bone mechanical property anisotropy [34], [35]. This further excludes the maximum normal stress, maximum shear stress, maximum principal strain, maximum strain energy density theories due to the inherent assumption of material isotropy. Tsai-Wu [36] theory has been be suggested for bone [37] and has shown reasonable accuracy [38] but it was later shown that planar failure envelopes were uncoupled from each other during biaxial [39] and triaxial [38] loading of bovine trabecular bone.

This has been observed in other cellular materials [40]–[42], where different failure mechanisms (rupture due to tensile stress or crushing/buckling of the cell walls) occur at different stress levels in different directions. Expanding on previous works, the modified super ellipsoid failure theory was developed to account for material anisotropy [26]. This approach showed great accuracy for trabecular bone but has limited utility. According to the authors, the analysis is anatomic site specific, thus limiting applicability to a single site in a single patient, let alone patients of the same species and furthermore, other species. [43]. Figure 1-6 displays the modified super ellipsoid , Von Mises, and Tresca failure envelopes (converted to strain). These data are shown here to establish the differences between the modified super ellipsoid, Von Mises, and Tresca failure envelopes and how these failure theories apply to experimental data.

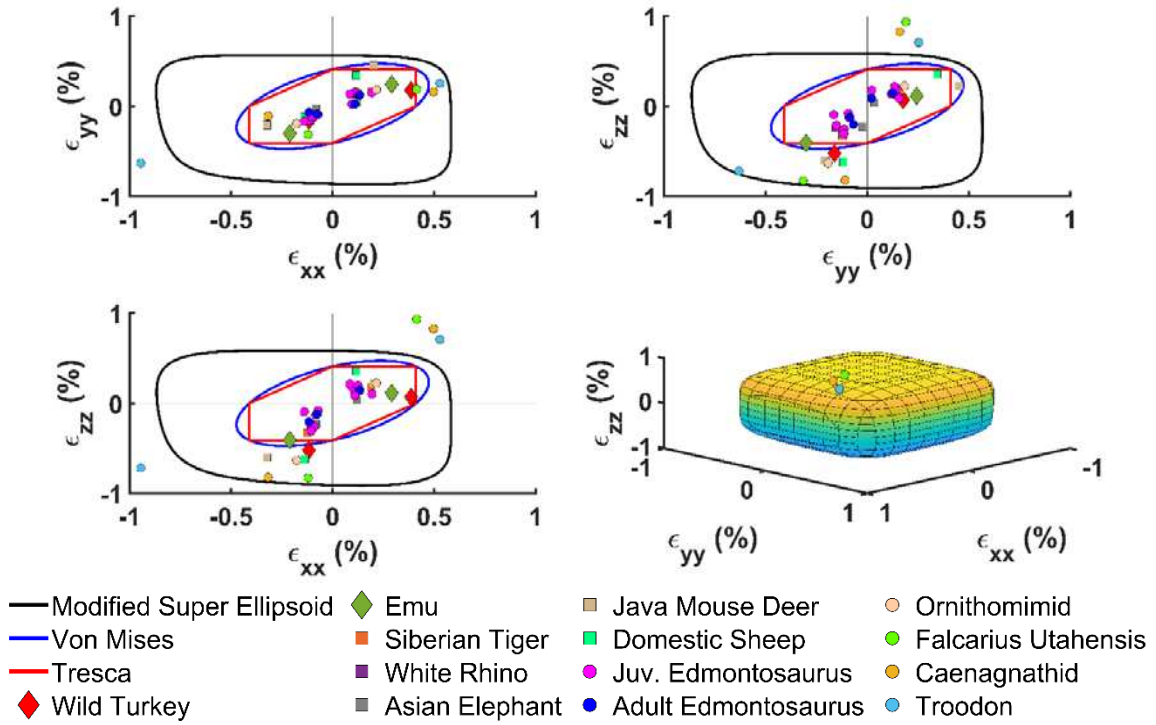

Figure 1-6: Yield envelopes for the (top left) $\boldsymbol{\varepsilon_{xx} - \varepsilon_{yy}}$, (top right) $\boldsymbol{\varepsilon_{zz} - \varepsilon_{yy}}$, and (bottom left) $\boldsymbol{\varepsilon_{zz} - \varepsilon_{xx}}$ normal strain planes, and (bottom right) three-dimensional modified super ellipsoid yield surface

Plots of this nature are interpreted by identifying data points outside the failure envelopes. If a data point falls outside of the envelope the strain experienced has exceeded the failure criterion (often the yield stress or strain). For data points who are inside the envelope the strain has not exceeded the failure criterion and thus did not fail. From Figure 1-6, the modified super ellipsoid, Von Mises, and Tresca failure theories show agreement for some species of this study and disagree on others. Since these theories disagree on several specimen there is motivation to find better methods for evaluating failure risk in trabecular bone.

1.6 Dinosaurs and their bones

Dinosaurs were massive animals that placed exceptional mechanical demands on their bones and were the largest animals to walk the Earth. Allometric relationships estimate that dinosaurs weighed in excess of 40,000 kg. *Edmontosaurus annectens* 7,936 kg [44], *Edmontosaurus regalis* 420 kg [44], *Supersaurus* 40,000 kg [45], *Camarasaurus* 47,000 kg [46], [47], *Apatosaurus* 22,400 kg [48], *Diplodocus* 20,000 kg [48] are examples of exceptionally massive animals. Several finite element analysis studies have been able to successfully investigate the biomechanics of dinosaur limbs. These studies primarily focus on the locomotor behavior the limbs [49]–[58]. There have also been numerous studies into the bite mechanics of dinosaurs [59]–[64]. One study [65] utilized finite element models to "rebuild" the skull of a Diplodocus using topological optimization to minimize mass and maximize strength. Making a few a priori assumptions about the location of eye sockets and the bite force of Diplodocus this study was able reconstruct the skull with reasonable accuracy. A recent finite element study [2], [66], [67] investigated the trabecular architecture of the hind limbs of Theropod dinosaurs. Though closely related to birds the trabecular bone architecture in plesiomorphic theropods was found to more closely resemble the trabecular architecture of modern humans, implying similar biomechanics as

humans. These conclusions were made based on the oblique nature of the trabeculae in the diaphysis of the femur being like that of humans. This study investigated the trabecular architecture and the effect it has on the behavior of the whole bone. There has been extensive research into the locomotor behavior and the whole bone strength of dinosaur bones there has been no investigation into the strength of dinosaur trabecular bone.

1.7 Motivation for research

The motivation for this research was to investigate the trabecular architecture of large mass animals as potential novel lightweight stiff material. According to the FAA 15,800,000+ flights are handled annually and is estimated that in 2017 there were 7,309 commercial planes in the United States alone [68]. It is estimated that $3,000 in fuel costs is saved annually per kilogram in reduced weight of a commercial plane [69], totaling an estimated annuals savings of $21,927,000 across the commercial airline industry. Furthermore, it is costs ~$10,000 per pound to send a payload into earth's orbit [70]. Independent of fuel costs it is estimated that the maintenance cost of an airplane is twice the initial purchase price over a 30 year life time of an aircraft [71]. The reduction of weight without sacrificing strength and reducing maintenance costs in structural components has been the main driving force for advances in aerospace components. 2000 series aluminum alloys are mainly used for aircraft structural frames where a key feature of this alloy are Al_2Cu and Al_2CuMg phases that increase fracture toughness and strength [72]. Higher strength alloys such as 7000 series aluminum alloys are commonly used in aircraft structural elements because of their high strength to weight ratios as compared to other aluminum alloys. However, because of the chemical composition these alloys suffers from corrosion, which is an important concern because of the environments (oil, hot/cold temperature, and high/low humidity) aircraft components are subjected to [73] and it is estimated that corrosion has cost $276 billion annually

to the aerospace industry [74]. Attempts to solve these problems and while maintaining high strength to weight ratios the aerospace and other industries have turned to fiber reinforced polymer matrix composites. An example of such composites are carbon fiber thermoset composites where these materials satisfy the needs of high operating temperatures, rigid design, and high strength to weight ratios [75]. However, these composites are prone to processed induced distortion due to mechanical property anisotropy in materials and high processing temperatures [76]. This combined with shortages of skilled composites workers [77], [78] there is significant motivation for aerospace materials development. For aluminum and other metals and metal alloys to stay competitive weight reduction and improvement in structural performance is imperative [71].

1.8 Hypotheses

It is hypothesized that trabecular architectures from large body mass animals have adapted to maximize stiffness while minimizing mass and therefore could be used as novel structures with high strength-to-weight ratio. The hypotheses of this study are as follows:

1. The apparent modulus of the trabecular bone in the long bones of animals will show positive correlation with body mass.
2. The trabecular architecture in the long bones of large mass extinct animals will show morphological changes like extant animals to accommodate increases in apparent modulus.
3. The trabecular architecture in the long bones of large mass animals will show similar levels of strain as smaller body mass animals under anatomic levels of strain for extant animals.

Chapter 2: Strong and light weight structures from dinosaur trabecular architecture [1]

2.1 Methods

2.1.1 ***Species analyzed in study***

The species used in the study were chosen to cover a wide range in body mass, from 1 to 47,000 kg, and are listed in Table 2-1. The CT and μCT scans from previous studies are indicated in Table 2-1 and for the mammoth, *Edmontosaurus*, *Apatosaurus*, *Camarasaurus*, and *Supersaurus*, new bone samples were obtained and scanned with μCT for the current study.

Table 2-1: Species used in the finite element models of this study

Study	Common Name	Specimen Number	Scientific Name	Body mass (kg)
[11]	Java Mouse Deer	UMZC H15013	*Tragulus javanicus*	1
[11]	Wild Turkey	RVC turkey 1	*Meleagris gallopavo*	4
[2]	Troodontid	MOR 748	*Troodontidae*	23
[11]	Emu	RVC emu_1	*Dromaius novaehollandiae*	27
[2]	Caenagnathid	TMP 1986.036.0323	*Caenagathidae*	49
[11]	Domestic sheep	RVC sheep2	*Ovies aries*	57
[2]	Ornithomimid	TMP 1999.055.0337	*Ornithomimidae*	100
[2]	Therizinosaur	UMNH VP 12360	*Falcarius Utahensis*	128
[11]	Siberian Tiger	RVC tiger_2	*Panthera tigris*	130

[1] This dissertation chapter was adapted with permission from Aguirre, T. G.; Ingrole, A; Fuller, L.: Seek, T. W.; Fiorillo, A. R.; Sertich, J. J. W.; Donahue, S.W. Differing trabecular bone architecture in dinosaurs and mammals contribute to stiffness and limits on bone strain, PLOS One, *In review*.

Funding was provided by the National Science Foundation Office of Polar Programs (OPP 0424594), as well as the National Geographic Society (W221-12) for the collection of Alaska Edmontosaurus materials used here. And, the Arctic Management Unit of the Bureau of Land Management provided administrative support. The specimens discussed here were collected under BLM permit number AA−86367. Travel funding for Mammuthus columbi sample collection was provided by the George C. Frison Institute of Archaeology and Anthropology.

Current	Hadrosaur	PMNS 22386	*Edmontosaurus sp.*	420
Current	Hadrosaur	[1]DMNH 22231	*Edmontosaurus sp.*	420
Current	Hadrosaur	[1]DMNH 22235	*Edmontosaurus sp.*	420
Current	Hadrosaur	[1]DMNH 2012 25-57	*Edmontosaurus sp.*	420
Current	Hadrosaur	[1]DMNH 22228	*Edmontosaurus sp.*	420
Current	Hadrosaur	[1]DMNH 22242	*Edmontosaurus sp.*	420
[11]	White Rhino	RVC french_rhino	*Ceratotherium simum*	3,000
[11]	Asian Elephant	RVC gita	*Elephas maximas*	3,400
Current	Hadrosaur	[2]DMNH 44398	*Edmontosaurus regalis*	7,936
Current	Hadrosaur	[2]DMNH 42169	*Edmontosaurus regalis*	7,936
Current	Mammoth	WA322-9	*Mammuthus columbi*	9,980
Current	Sauropod	UW20501	Apatosaurus sp.	22,000
Current	Sauropod	WYDICE DMJ-0021 05	Supersaurus	40,000
Current	Sauropod	UW20519	Camarasaurus	47,000

University Museum of Zoology Cambridge (UMZC), Royal Veterinary College (RVC), Museum of the Rockies (MOR), Royal Tyrrell Museum of Palaeontology (TMP), Natural History Museum of Utah (UMNH), Perot Museum of Nature and Science ([1]DMNH), Denver Museum of Nature & Science ([2]DMNH), University of Wyoming (UW), Wyoming Dinosaur Center (WYDICE). 48WA is the archaeological site identification code per the Smithsonian trinomial system. The specimen was obtained from the University of Wyoming Archaeological Repository (UWAR) fossil collection.

The body mass estimations for the extinct species of this study are as follows: *Edmontosaurus regalis* 7,936 kg [44], *Edmontosaurus sp.* 420 kg [44], *Supersaurus* 40,000 kg [45], *Camarasaurus* 47,000 kg [46], [47], *Apatosaurus* 22,400 kg [48], *Troodontid* 23kg [79], Caenagnathid 49kg [80], *Falcarius utahensis* 128 kg [81], Ornithomimid 100 kg [82], and *Mammuthus columbi* 9,980kg [83]. For the *Mammuthus columbi* and *Supersaurus*, the body mass estimations are for the specific specimens used in this study. For the other species, the body masses were obtained from the published estimates shown above and were assumed to be the same for all specimens of a given species.

2.1.2 **Fossilized bone verification through optical microscopy and energy dispersive x-ray spectroscopy**

To verify trabecular bone in Apatosaurus, Supersaurus, and Camarasaurus samples used for μCT were comprised of fossilized bone tissue, the samples were imaged using an optical microscope, scanning electron microscope (SEM), and elemental analysis was performed using energy-dispersive x-ray spectroscopy (EDS). The bone samples were sectioned and polished to a mirror finish using a 1-micron polycrystalline diamond suspension. Samples were imaged using a Hitachi S-4800 SEM equipped with an x-ray energy dispersive spectrometer (EDAX Genesis). Samples were coated with ~ 10 nm of carbon to prevent charging of the sample surface. Bone specimen collected for this study were imaged with 20 μA probe current and 15 keV excitation voltage. Planar maps of the elemental composition were obtained and confirmed the bone tissue contained high percentages of calcium and phosphorous.

2.1.3 **Computed tomography scanning**

For the species in this study, trabecular bone samples from the medial portion of either the proximal tibia or distal femur were analyzed based on availability (Figure 2-1). These locations were selected because of similarities in the trabecular bone architectural indices in these two regions [84]. Archival μCT scans of trabecular bone from the lateral femoral condyles were accessed via a public database (Doube, 2018). High-resolution CT scans of fossilized dinosaur limbs were provided by Dr. Peter Bishop at the Royal Veterinary College in the United Kingdom [2], [66], [67]. Sections of trabecular bone were virtually cropped from the lateral femoral condyle in the CT scans. Additionally, cylindrical cores of trabecular bone were collected from several fossilized specimens. Two adult hadrosaur (*Edmontosaurus annectens*) tibiae were provided by the Denver Museum of Nature & Science. Six juvenile hadrosaur (*Edmontosaurus* sp.) tibiae were

provided by the Perot Museum of Nature and Science. A tibial core was collected from the *Supersaurus* in the Wyoming Dinosaur Center fossil collection. Samples from a *Camarasaurus* tibia and *Apatosaurus* lateral femur were collected from the University of Wyoming Geology and Geophysics Department fossil collection. A femoral core was collected from a Columbian mammoth (*Mammuthus columbi*) in the University of Wyoming Archaeological Repository fossil collection. Figure 2-1 displays the anatomical locations from which cores for this study, and from previous studies [2], [11], [12], were obtained. Trabecular cores collected for this study were 8 mm diameter and 50–75 mm long and were harvested using a diamond sintered coring bit. During drilling, water was pumped through the center of the coring bit to cool the sample/bit and flush out debris. The trabecular cores were scanned with a SCANCO micro-computed tomography machine (SCANCO μCT 80) at high resolution, 8W, and 70 kV peak excitation voltage to produce 10-micron voxels. To prevent image distortion fossilized trabecular bone cores were scanned through a copper filter [85]. The trabecular bone volume fraction (BV/TV), trabecular thickness (Tb.Th), trabecular spacing (Tb.Sp), and connectivity density (Conn.D) for each CT scan [2], [11] were measured using BoneJ [86] and the trabecular number (Tb.N) was computed using the methods in [87].

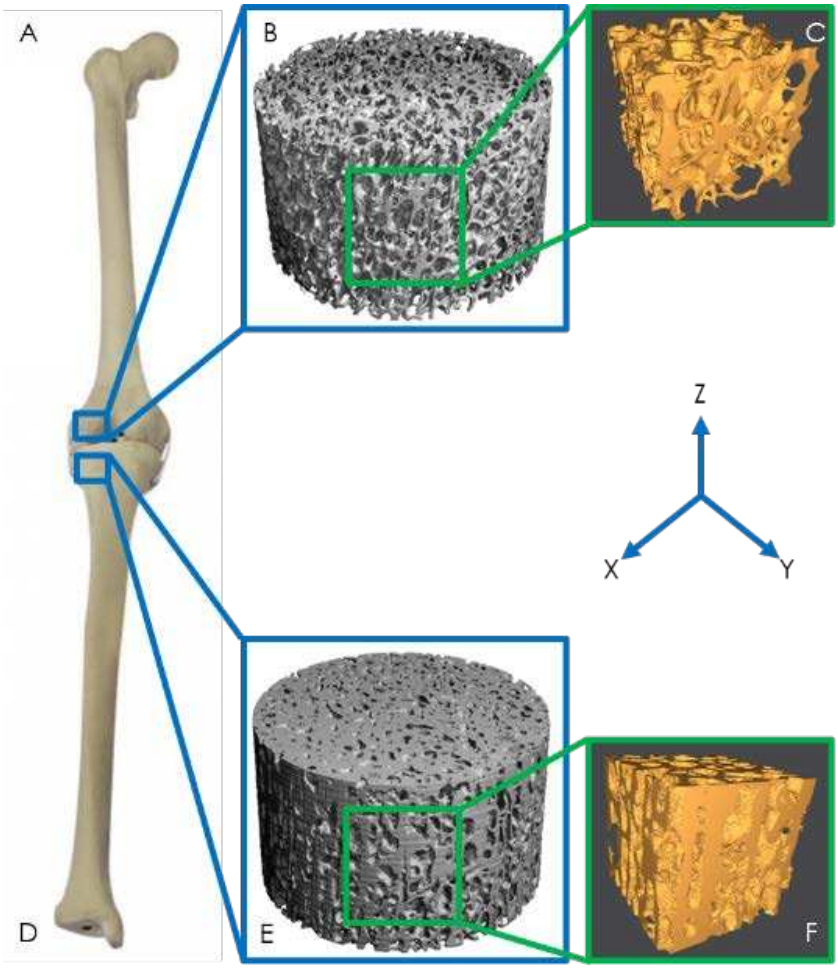

Figure 2-1: A) Femoral core location, B, E) µCT scans of trabecular cores, C, F) finite element models of trabecular bone, D) Tibial core location.

2.1.4 **Finite element model generation**

The CT and µCT DICOM files were binarized with Seg3D to separate the bony material from the marrow space. Cubes were cropped from the center of the cylindrical scan volume to generate the finite element models (Figure 2-1 C & F). This location was chosen so that peripheral damage from cutting the cylindrical cores was not included in the finite element models. The bulk dimensions of the finite element models varied due to differences in the available µCT scan regions of intact bone (e.g., some *Edmontosaurus* and the *Mammuthus* samples had irregular geometries due to the coring process). However, all finite element models had the dimensions required to treat trabecular bone as a continuum, which is 5-10 trabecular spacings [88]. Sample image files were

exported in the ASCII STL file format for further file preparation. The STL files were opened using MeshMixer to create a solid volume from the surface model exported from Seg3D and to repair any errors during surface triangulation. The files were then meshed in ICEM CFD to generate a linear tetrahedral element mesh, and finite element models were generated using ABAQUS. Shown in Figure 2-2 is an example of a meshed trabecular bone cube used in this study.

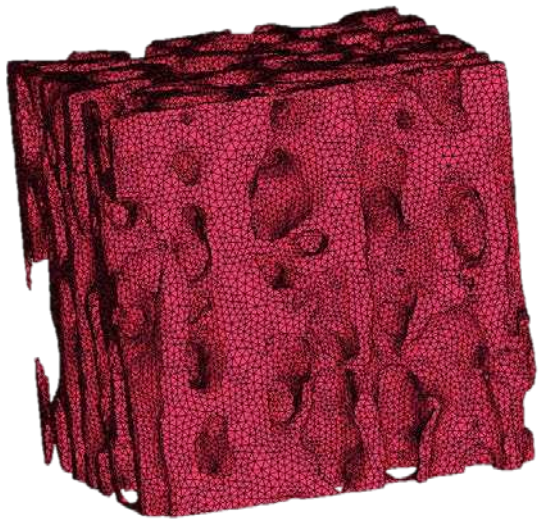

Figure 2-2: Meshed trabecular bone cube used in the finite element models

2.1.5 **Finite element modeling**

2.1.5.1 Mesh Convergence

To determine the optimal mesh for the finite element models a mesh (numerical) convergence study [30], [89] was performed. For this study, five unique mesh densities, ranging from 50,797 to 1,019,808 elements per cubic millimeter, were created for the trabecular bone specimen with the smallest average trabecular thickness and the models were subjected to a strain of 0.415%. To determine whether the mesh had converged, the change in strain energy between

each mesh was analyzed and compared to the finest mesh as a percent difference using Equation 1.

$$\Delta = \frac{X_N - X_i}{X_N} 100\% \quad (2 - 1)$$

Where Δ is the percent difference and X is strain energy. X_N is strain energy for the finest mesh in the mesh convergence study and X_i is the strain energy for the other meshes used in the study.

2.1.5.2 Quasi-static compression finite element models

The FEM size for each specimen was chosen to be between 5 and 10 trabecular spacing's, depending on the available size of the scanned bone. However, for each model the minimum dimensions were greater than 5 trabecular spacing's and are therefore within the range of continuum dimensions for trabecular bone [88]. Because each specimen used in the FEA study had a different physical size and different bone volume fraction, an apparent stress of 9.36 MPa was applied to each FEM. This applied stress is equal to one-half of the yield stress for human femoral trabecular bone [31]. This stress was converted to a force using the bulk specimen geometry for each FEM and was chosen because it is within the ranges of stress that occur in trabecular bone for physiological activities [65], [90]. All FEM were assigned an elastic modulus of 15 GPa and Poisson's ratio of 0.3 [10], [31] and modeled as linear elastic with linear (4 node) tetrahedral elements and parallel processed using 8 CPUs. An example finite element model is shown in Figure 2-3.

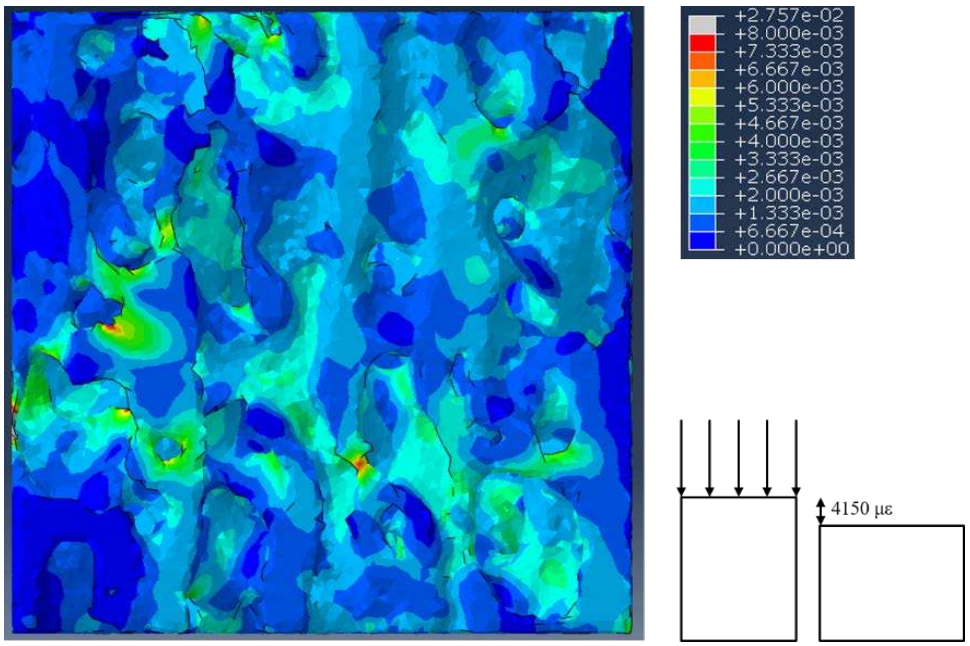

Figure 2-3: Example finite element model after compression to a macroscopic strain of 4,150 microstrain (με). The color gradient corresponds to the max principal strain in each element. Dark blue regions with zero strain correspond to the marrow spaces.

2.1.6 **Apparent and Specific Apparent Modulus**

The effect of the trabecular bone architecture on the apparent elastic modulus was determined from the linear region of the stress-strain curve from each finite element model. To account for differences in BV/TV between each cube, the specific apparent elastic modulus was computed by dividing the apparent elastic modulus by the product of the bone volume fraction and a trabecular bone tissue density of 1.874 grams/cm^3 [4]. This was done because the bone tissue density of the fossilized samples could not be accurately measured due to the fossilization process.

2.1.7 **Risk of failure assessment**

To assess the likelihood of failure of the samples in this study, trabecular principal strains were analyzed. The normal and shear strain components were collected from element centroids for every element in each finite element model using a custom Python script. Data were collected from

the centroids of the elements because the Gauss (integration) point is located at the element centroid for a linear tetrahedral element [91]. A custom MATLAB script was used to compute the principal strains for each model by computing the eigenvalues of the 3D strain tensor [92]–[94]. The average tensile and compressive principal strains (of all the elements) were computed for each finite element model. Additionally, the average tensile and compressive principal strains were computed for each finite element model only considering elements that had strain values that exceeded the tensile ($\varepsilon_y = 0.41\%$) and compressive ($\varepsilon_y = -0.83\%$) yield strains of human trabecular bone. The yield strains for human trabecular bone were used because the yield strains are narrowly distributed [26], [95], [96]. These four strain parameters were regressed against body mass.

2.1.8 **Allometric scaling**

To determine how the trabecular bone architectural indices of the specimen of this study scale with body mass, log-log plots for these properties were created and compared to mammalian and avian species [11], [13]. Allometric scaling relationships were created for the trabecular bone architectural indices versus body mass by linearization of the equation $y = a \cdot x^b$ [97] through a base-10 logarithmic transformation such that:

$$log_{10}(y) = log_{10}(a) + b \cdot log_{10}(x) \quad (2 - 2)$$

In Equation 2 $log_{10}(y)$ and $log_{10}(x)$ are the logarithmically transformed trabecular bone architectural indices and body mass, respectively and $log_{10}(a)$ and b are the y-intercept and slope, respectively, from the linear regressions performed on base-10 logarithmically transformed values for the trabecular bone architectural indices and body mass [98].

2.1.9 **Statistical analyses**

Linear regressions between trabecular bone architectural indices and body mass were made to determine allometric scaling relationships for mammalian, avian, and dinosaurian species. Pairwise comparisons were made between regression slopes of the mammalian, avian, and dinosaurian species. In the pairwise comparisons, species was used as a categorical predictor with dinosaurian species used as the reference level. Stepwise regressions were used to determine if the trabecular bone architectural indices predict the apparent and specific apparent elastic moduli. The candidate independent variables were Tb.Th, Tb.Sp, and Conn.D, and the dependent variables were apparent elastic modulus and specific apparent elastic modulus. Trabecular number and bone volume fraction were excluded from stepwise regression models to avoid collinearity since both of these parameters are dependent on trabecular thickness and trabecular spacing [87]. For the stepwise regressions the mammalian and dinosaurian apparent and specific apparent elastic moduli data from the finite element models were analyzed separately. Similarly, the apparent elastic modulus, specific apparent elastic modulus, and principal strains for the dinosaurian and mammalian species were analyzed separately for linear regressions versus body mass. Pairwise comparisons were made between the regression slopes for data from the finite element models. Linear regressions, pairwise comparisons, and stepwise regressions were computed using Minitab. Due to the imbalance between the numbers of dinosaurian samples the average values for *Edmontosaurus regalis* and *Edmontosaurus sp.* were used in all regressions. Due to the low number of dinosaur samples we let $\alpha = 0.1$ to reduce the chance of Type II error [99]–[101].

2.2 Results

2.2.1 Fossilized bone verification

Figure 2-4 shows optical images of the trabecular architecture of the *Camarasaurus*, *Supersaurus*, *Apatosaurus*, and *Diplodocus* show heavy sedimentation within the trabecular architecture. Specimen were imaged using the appropriate light polarization angle to best show the trabecular architecture and sedimentation. The diplodocus specimen shows that the trabecular architecture has been shattered and is indicated by the red arrow shown in Figure 2-4. This eliminated this specimen from the EDS and histological studies.

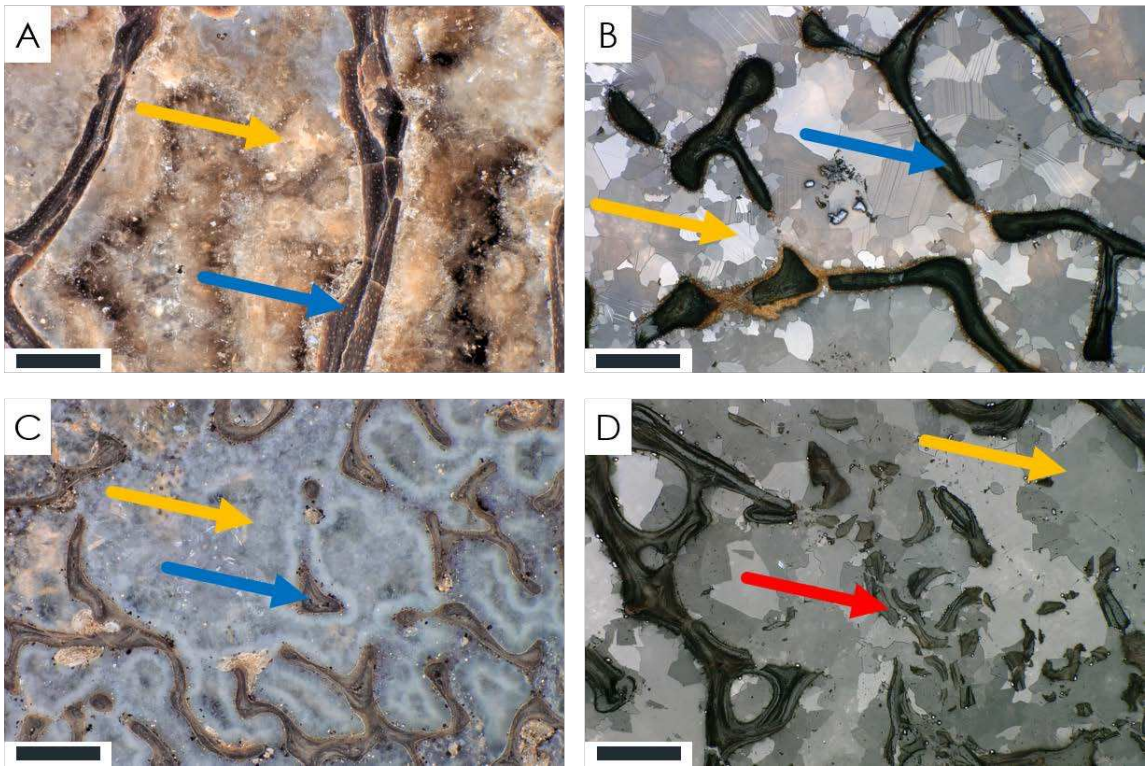

Figure 2-4: Optical microscopy images of the trabecular architecture A) *Apatosaurus*, B) *Supersaurus*, C) *Camarasaurus*, D) *Diplodocus*. Scale bars are 500 microns. The blue arrows indicate trabeculae and orange arrows indicate sedimentation in the marrow space.

Figure 2-5 shows the elemental maps from EDS imaging of *Apatosaurus*, *Supersaurus*, and *Camarasaurus* specimens. The elemental mapping shows high concentrations of calcium and phosphorous occur concurrently indicating the structures shown are indeed fossilized bone tissue.

Similarly, previous EDS analyses of *Edmontosaurus* samples established that the structures demonstrating calcium and phosphorous concurrently were similar to the trabeculae imaged with μCT, without the mineralized material in the marrow space [102]. *Apatosaurus* and *Supersaurus* specimens show high calcium concentrations surrounding trabeculae, which is indicative of a mineral containing high amounts of calcium such as calcium bentonite or fluorite in the marrow space. The sedimentation within the marrow space of the *Camarasaurus* specimen is composed of mineral that contains neither calcium nor phosphorous and therefore does not show up in these EDS maps.

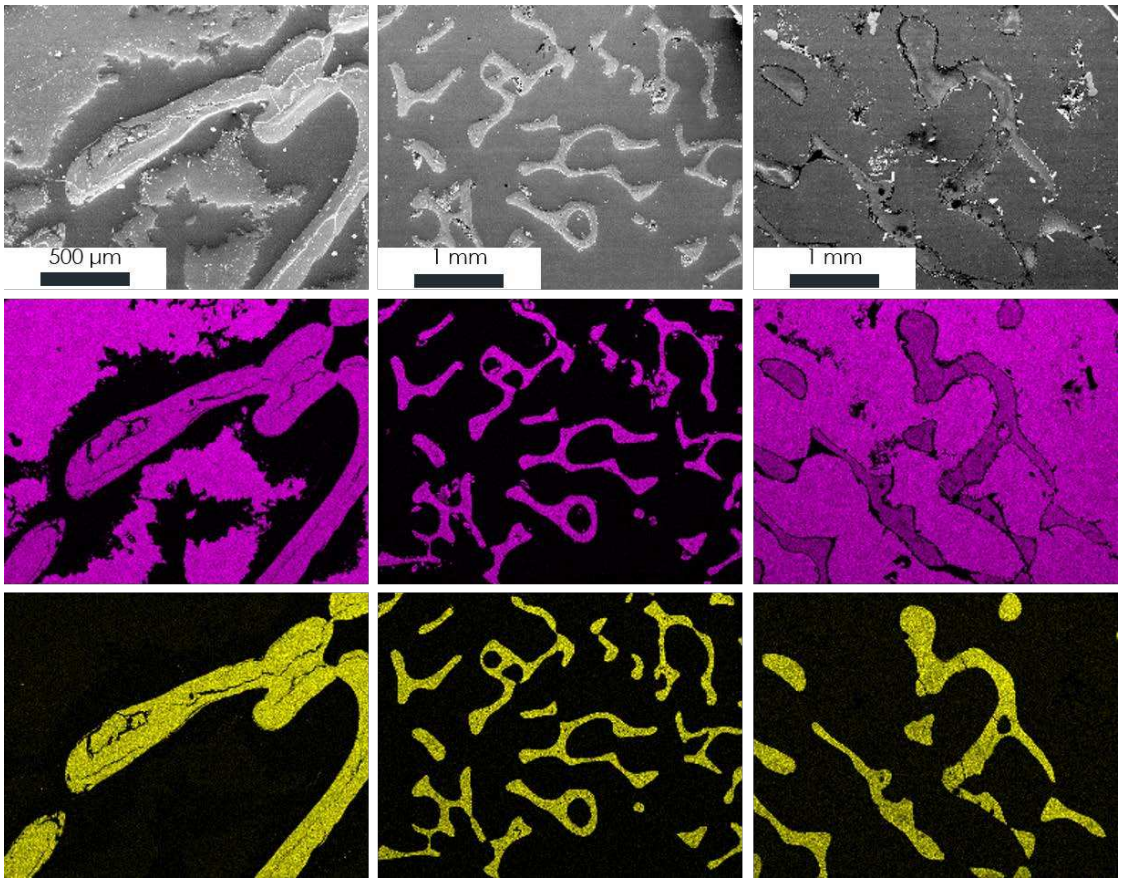

Figure 2-5: SEM and EDS elemental maps of the trabecular architecture from dinosaur trabecular bone that was harvested for this study. Left) *Apatosaurus*, Middle) *Camarasaurus*, Right) *Supersaurus*. In the images pink = calcium and yellow = phosphorous

2.2.2 **CT scan segmentation**

Shown in Figure 2-6, Figure 2-7, and Figure 2-8 are the segmented CT scans for *Camarasaurus*, *Supersaurus*, and *Apatosaurus*, respectively. From these figures the marrow space sedimentation was unable be separated from the CT scans as indicated by the yellow arrows. Furthermore, evidence of artifacts from the CT scanning process are observed in all images. Since the trabecular structure could not be segmented all these specimens were not used to generate finite element models.

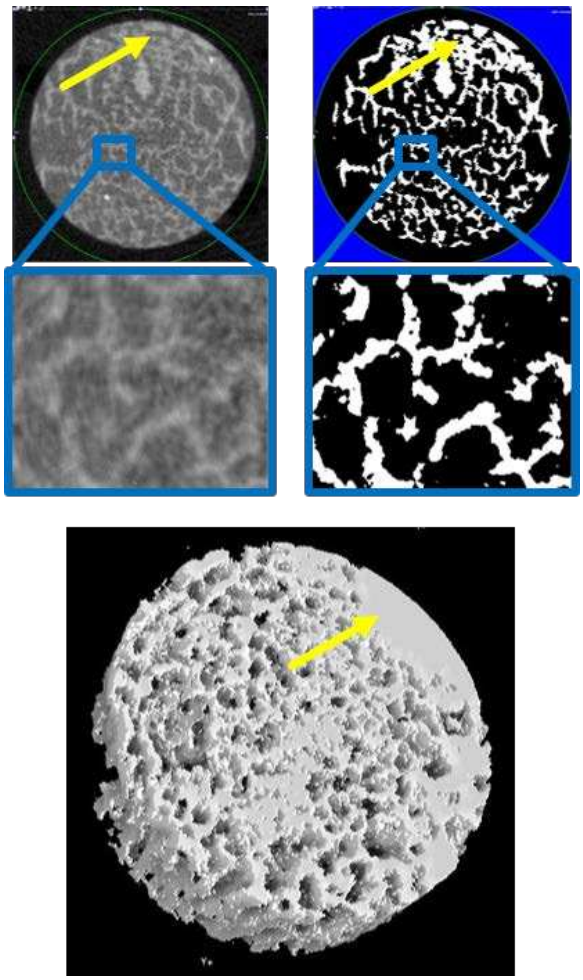

Figure 2-6: Segmented Camarasaurus CT scan

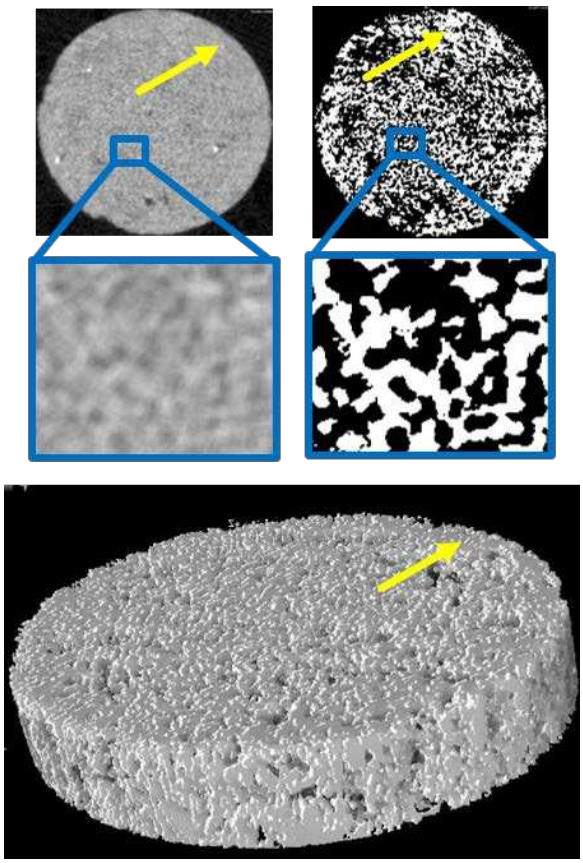

Figure 2-7: Segmented Supersaurus CT scan

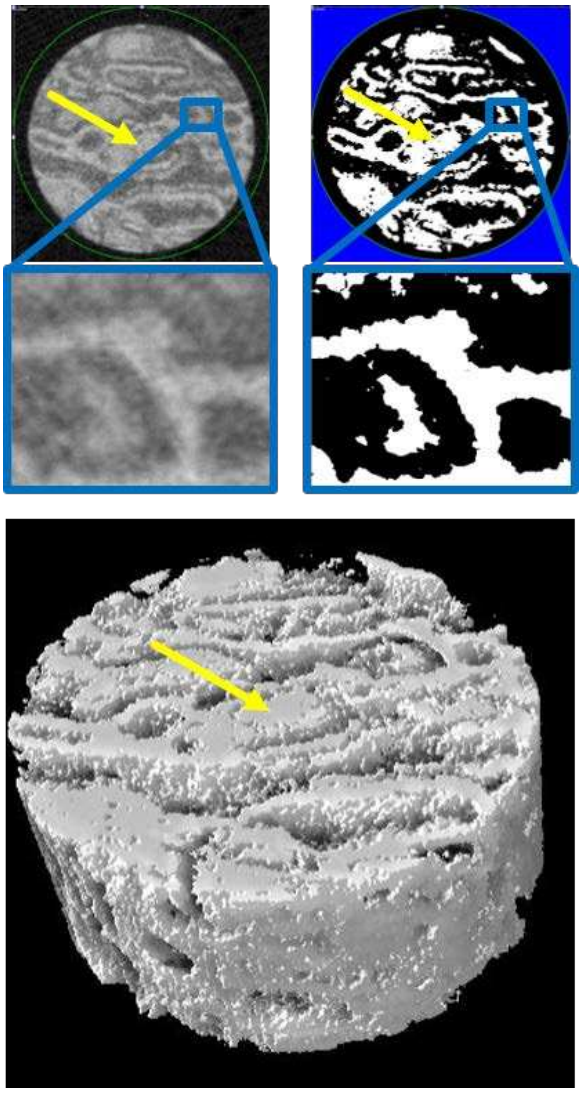

Figure 2-8: Segmented Apatosaurus CT scan

2.2.3 **Trabecular indices and allometric scaling**

The average and standard deviation for the mammalian, avian, and dinosaurian architectural indices are shown in Table 2-2. Allometric scaling relationships are shown in Figure 2-9 - Figure 2-13 and Table 2-3. The regressions indicate that for mammals, bone volume fraction, trabecular thickness, and trabecular spacing show positive correlation with body mass, and trabecular number and connectivity density show negative correlation with body mass. For the avian data, the regressions indicate that bone volume fraction, trabecular thickness, and trabecular

spacing show positive correlation with body mass, and trabecular number and connectivity density show negative correlations with body mass. For the dinosaurian species, positive correlation with body mass is observed for trabecular number and connectivity density and negative correlation with body mass for bone volume fraction, trabecular thickness, and trabecular spacing. The data for the trabecular bone architectural indices covers seven orders of magnitude of body mass.

Table 2-2: Trabecular bone architectural indices (mean ± standard deviation_

	Mammalian	Avian	Dinosaurian
BV/TV (%)	29.31 ± 8.75	12.97 ± 5.45	37.21 ± 6.47
Tb.Th (µm)	145.84 ± 80.43	180.95 ± 111.98	335.98 ± 122.49
Tb.Sp (µm)	428.48 ± 165.91	2030.37 ± 1310.46	452.11 ± 221.32
Tb.N (mm^{-1})	2.15 ± 1.24	0.62 ± 0.39	1.55 ± 0.78
Conn.D (mm^{-3})	54.17 ± 126.71	4.75 ± 5.26	19.01 ± 28.16

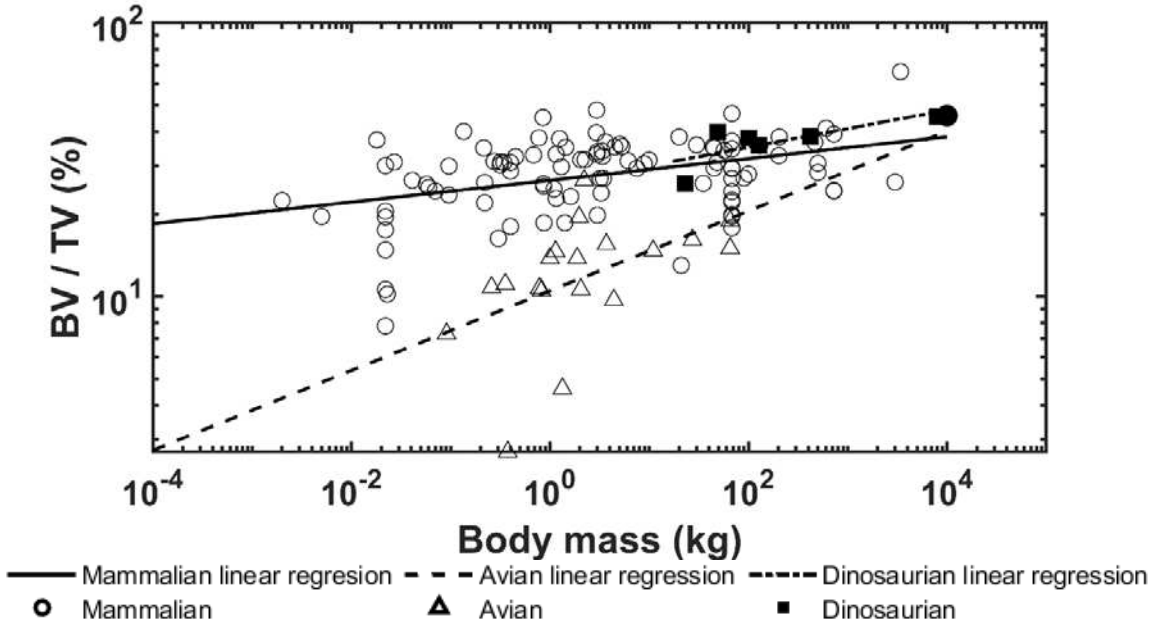

Figure 2-9: Logarithmically scaled plots of the bone volume fraction (BV/TV) versus body mass. Pairwise comparisons indicate the dinosaur regression slope is not different from the mammalian (p = 0.352) and avian (p = 0.695) slopes. The solid circle indicates the mammoth.

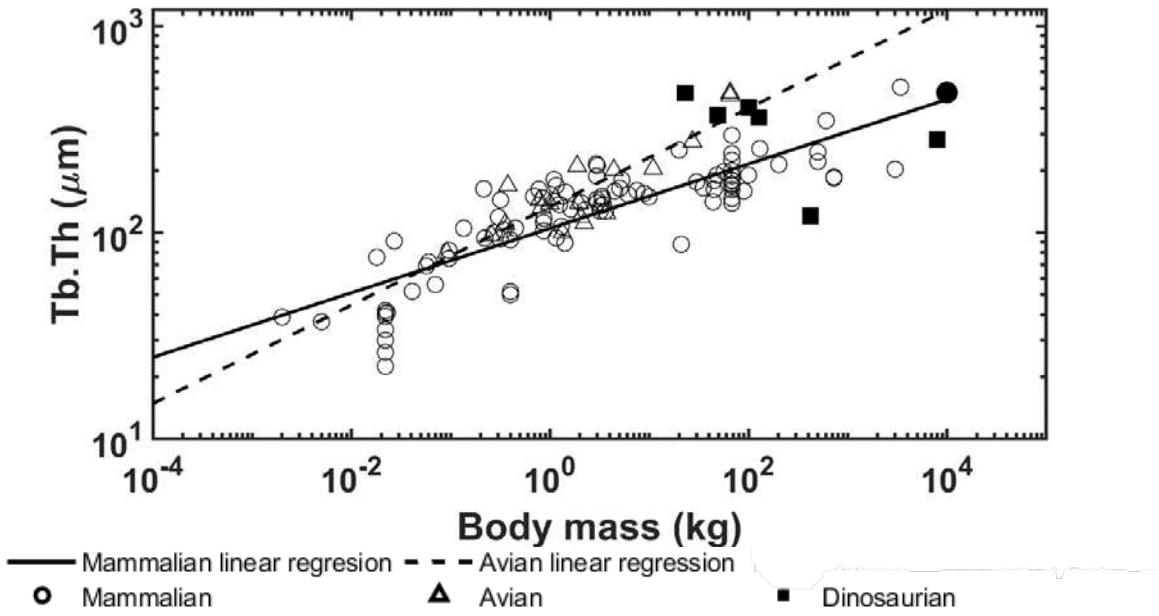

Figure 2-10: Logarithmically scaled plots of the trabecular thickness (Tb.Th) versus body mass. Pairwise comparisons indicate the dinosaur regression slope is different from the mammalian ($p < 0.001$) and avian ($p < 0.001$) slopes. The solid circle indicates the mammoth.

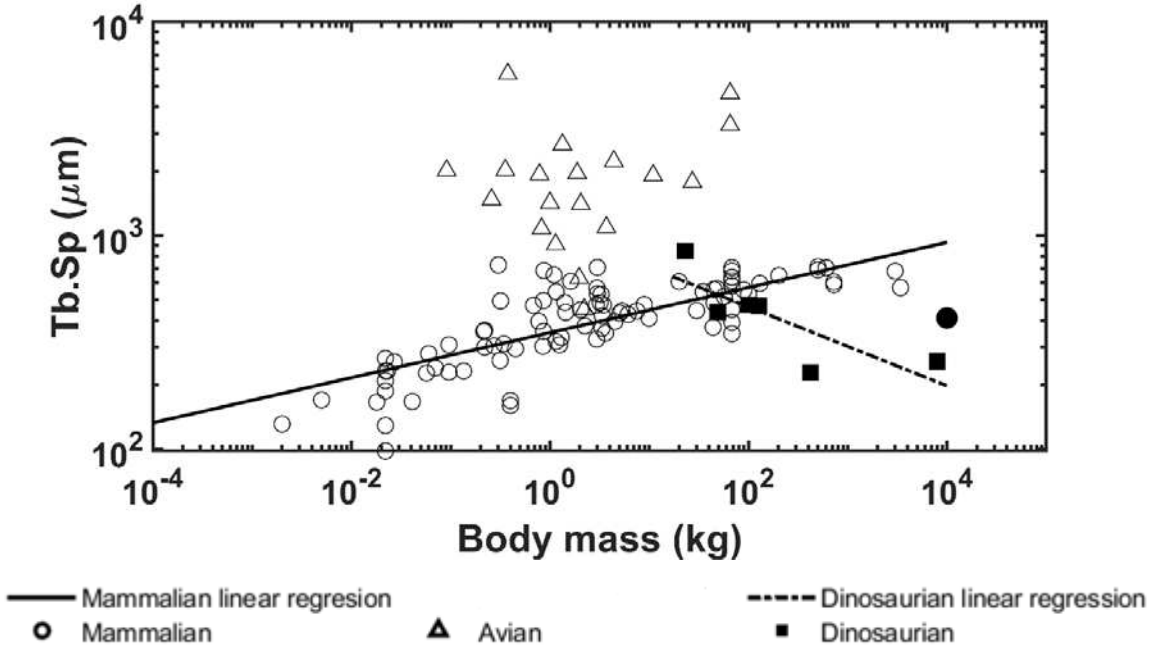

Figure 2-11: Logarithmically scaled plots of the trabecular spacing (Tb.Sp) versus body mass. Pairwise comparisons indicate the dinosaur regression slope is different from the mammalian ($p < 0.001$) and avian ($p = 0.007$) slopes. The solid circle indicates the mammoth.

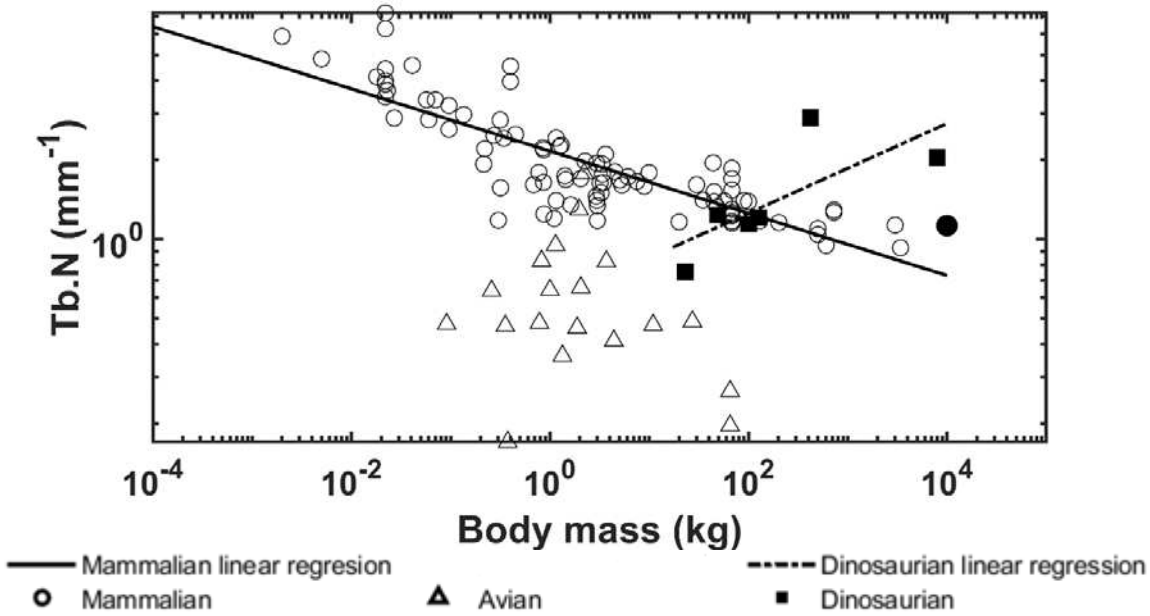

Figure 2-12: Logarithmically scaled plots of the trabecular number (Tb.N) versus body mass. Pairwise comparisons indicate the dinosaur regression slope is different from the mammalian ($p < 0.001$) and avian ($p = 0.004$) slopes. The solid circle indicates the mammoth.

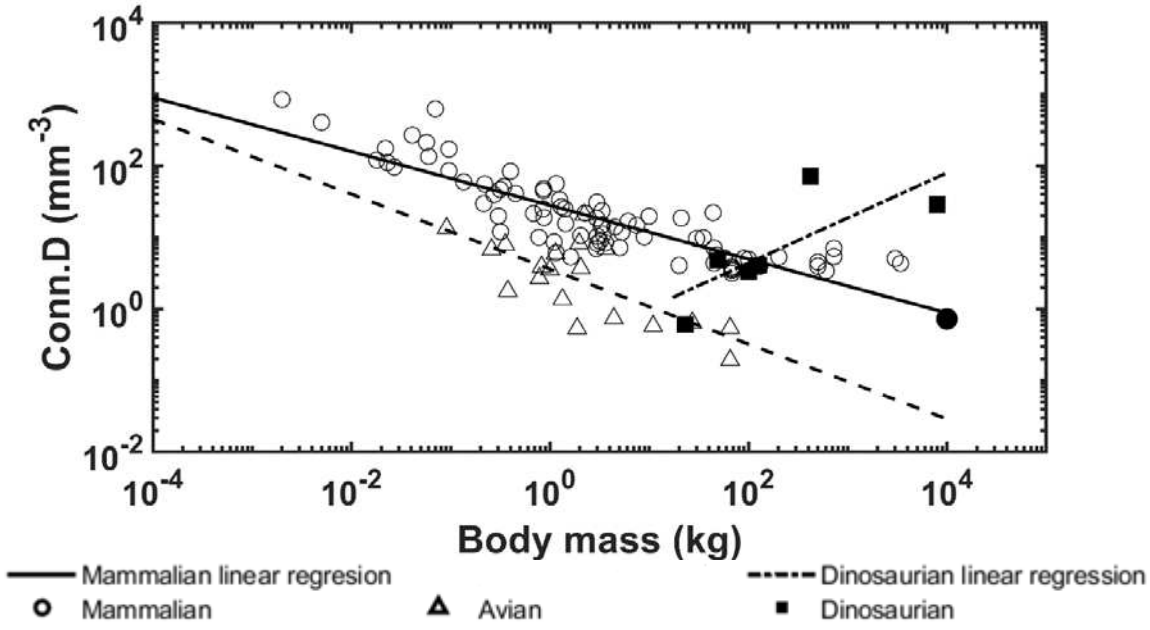

Figure 2-13: Logarithmically scaled plots of connectivity density (Conn.D) versus body mass. Pairwise comparisons indicate the dinosaur regression slope is different from the mammalian ($p < 0.001$) and avian ($p < 0.001$) slopes. The solid circle indicates the mammoth.

Table 2-3: Linear regression results: Slope (b), with 95% confidence intervals (CI), intercept ($log_{10}(a)$), coefficient of determination (R^2), and p-values for the regression slopes.

Class		b	-CI	+CI	$log_{10}(a)$	R^2	p
Mammalian	BV/TV (%)	0.040	0.02	0.06	1.425	0.161	<0.001
	Tb.Th (µm)	0.156	0.14	0.18	2.020	0.726	<0.001
	Tb.Sp (µm)	0.106	0.09	0.12	2.545	0.583	<0.001
	Tb.N (mm^{-1})	-0.118	-0.13	-0.10	0.334	0.698	<0.001
	Conn.D (mm^{-3})	-0.376	-0.42	-0.33	1.449	0.763	<0.001
Avian	BV/TV (%)	0.146	0.02	0.28	1.021	0.249	0.030
	Tb.Th (µm)	0.238	0.17	0.31	2.125	0.761	<0.001
	Tb.Sp (µm)	0.069	-0.11	0.24	3.209	0.039	0.416
	Tb.N (mm^{-1})	-0.081	-0.24	0.08	-0.249	0.061	0.306
	Conn.D (mm^{-3})	-0.524	-0.79	-0.26	0.556	0.513	<0.001
Dinosaurian	BV/TV (%)	0.068	-0.02	0.15	1.410	0.552	0.091
	Tb.Th (µm)	-0.115	-0.40	0.17	2.753	0.235	0.330
	Tb.Sp (µm)	-0.185	-0.37	0.00	3.036	0.649	0.053
	Tb.N (mm^{-1})	0.170	-0.04	0.38	-0.241	0.549	0.092
	Conn.D (mm^{-3})	0.631	-0.10	1.36	-0.619	0.591	0.074

2.2.4 **Finite element modeling**

2.2.4.1 Mesh convergence

Shown in Figure 2-14 and Table 2-4 are the results of the mesh convergence study. Convergence was achieved at a mesh density of 435,725 elements per cubic millimeter, which had a 3% difference from the finest mesh density of 1,019,808 elements per cubic millimeter.

Table 2-4: Mesh convergence study

Study #	Elements per unit volume	Displacement (µm)	Displacement (% difference)	Peak Strain Energy (mJ)	Peak Energy (% difference)	Computation time (hours)
1	50,797	62.34	10.20%	16.5520	10.40%	0.19
2	91,278	65.14	6.17%	16.9810	8.08%	0.35
3	227,742	66.18	4.67%	17.7088	4.14%	0.89
4	435,724	67.43	2.87%	17.9692	2.73%	1.79
5	1,019,808	69.42	0.00%	18.4730	0.00%	4.60

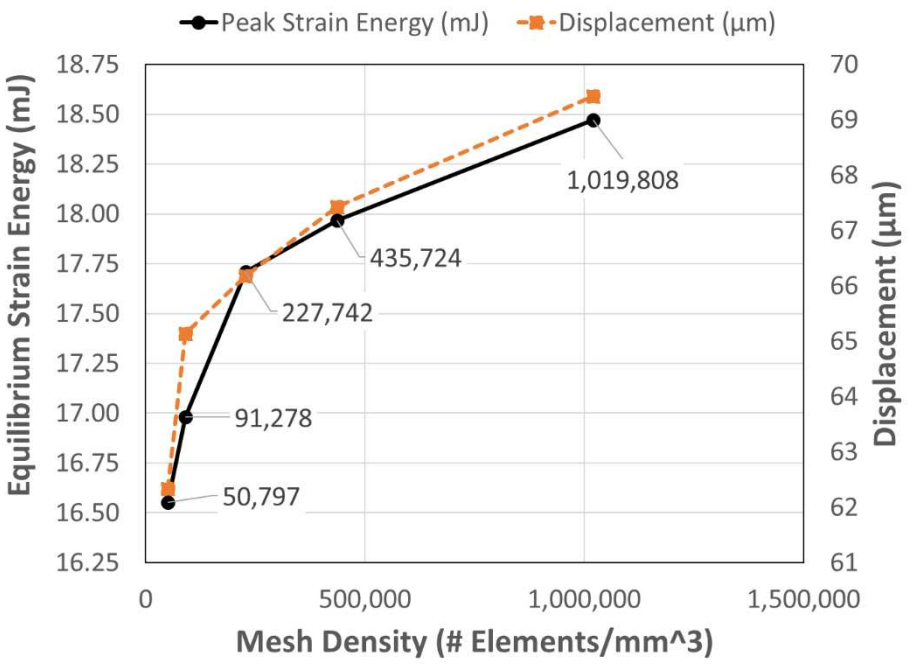

Figure 2-14: Mesh convergence study

2.2.4.2 Apparent and Specific Apparent Modulus

The apparent modulus and specific apparent modulus show positive correlation with body mass (Figure 2-16 & Figure 2-16). For the dinosaurian species, positive correlation with body mass is observed for apparent ($p = 0.007$, $R^2 = 0.865$) and specific apparent modulus ($p = 0.008$, $R^2 = 0.857$). For the mammalian species, no correlation with body mass is observed for apparent ($p < 0.268$) and specific apparent modulus ($p = 0.164$). The apparent and specific apparent moduli were dependent on the trabecular bone architectural indices. For the dinosaurian species, apparent elastic modulus was found to follow the equation $E_{App} = 0.0722 \times Conn.D$ ($p = 0.062$, $R^2 = 0.5337$) and specific apparent modulus was found to follow the equation $E_{App\ Spec} = 0.0974 \times Conn.D$ ($p = 0.056$, $R^2 = 0.5504$). For the mammalian species, apparent elastic modulus was found to follow the equation $E_{App} = 10.67 \times Tb.Th$ ($p < 0.001$, $R^2 = 0.9644$) and specific apparent modulus was found to follow the equation $E_{App\ Spec} = 5.32 \times Tb.Th + 4.65 \times Tb.Sp$ (for the constants, $p = 0.056$ and 0.017, respectively, for the regression, $p = 0.001$ and $R^2 = 0.9741$)

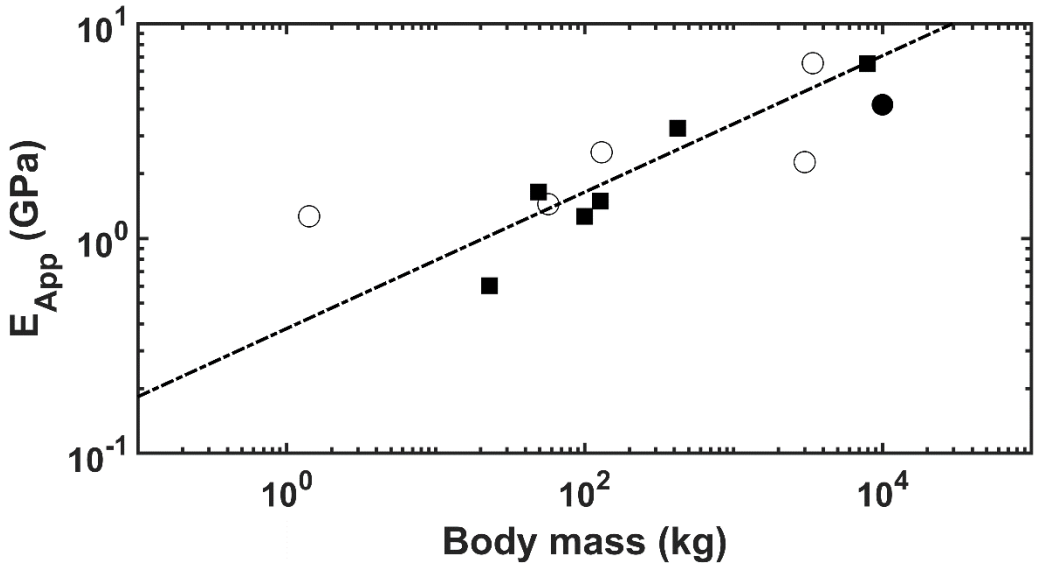

Figure 2-15: Apparent elastic modulus versus body mass. Trabecular bone apparent modulus is positively correlated with body mass in dinosaurs, while for mammalian species no correlation is observed. The solid circle indicates the mammoth.

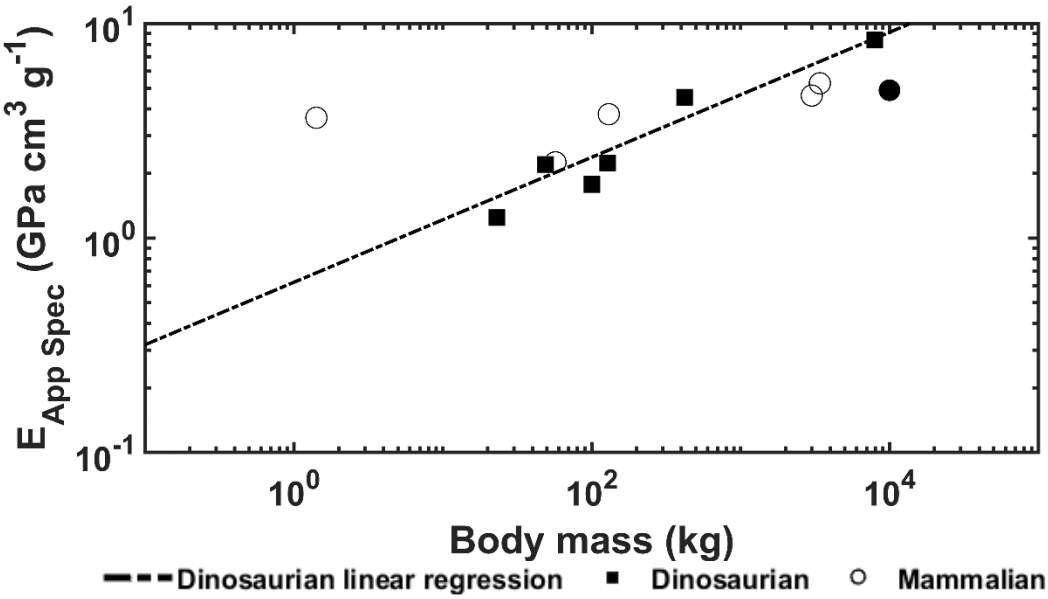

Figure 2-16: Specific apparent elastic modulus versus body mass. The solid circle indicates the mammoth.

2.2.4.3 Principal strains

Average tensile and average compressive principal strains are shown in Figure 2-17, where all strain magnitudes were all less than or equal 2,856 microstrain. For the dinosaurian models no correlation with body mass was observed for the average tensile ($p = 0.403$) or average compressive ($p = 0.156$) principal strains. Similarly, there was no correlation between body mass and the largest tensile (5,394 ± 1,750 microstrain, $p = 0.668$) or largest compressive (10,587 ± 3,099 microstrain, $p = 0.122$) principal strains. For the mammalian models, no correlation with body mass was found for the average tensile ($p = 0.398$) or average compressive principal strain ($p = 0.167$). Similarly, for the mammalian models, no correlation was observed between body mass and the largest tensile (4,992 ± 1,080 microstrain, $p = 0.649$) and compressive (10,018 ± 2,062 microstrain, $p = 0.316$) principal strains.

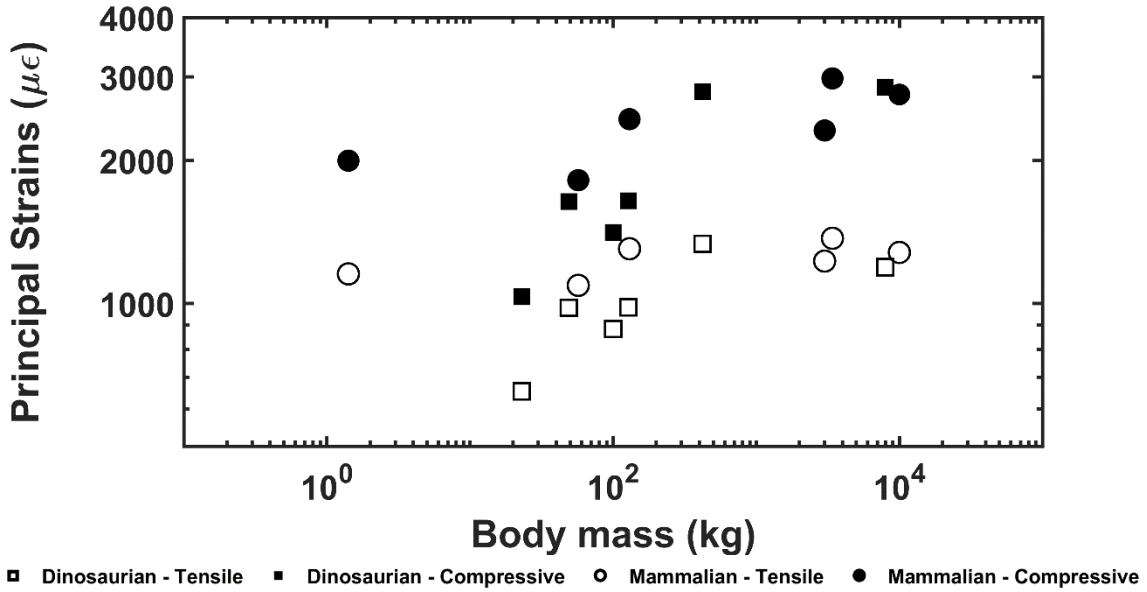

Figure 2-17: Average compressive and tensile principal strains versus body mass. Strains are shown in microstrain (με). There is no correlation between body mass and the compressive/tensile principal strains in both mammalian and dinosaurian trabecular bone.

2.3 Discussion

Allometry and mechanical performance of trabecular bone architecture of extant and extinct species (i.e., dinosaurs and mammoth) were investigated to provide framework for understanding how trabecular bone helped support extremely massive animals. Previous studies of extant mammalian and avian species found no correlation between trabecular bone volume fraction and body mass in animals ranging in body mass from mouse to elephant [11], [13]. This result is surprising since animals with greater mass require stiffer bone structures to support larger gravitational loads and apparent elastic modulus is positively correlated with bone volume fraction [17]. It is possible that the trabecular architecture of extremely massive animals was adapted to accommodate large gravitational loads while minimizing bone mass by maintaining a constant bone volume fraction. The trabecular architecture of dinosaurs has been related to locomotor behavior [2], [66], [67], but relationships between trabecular bone architectural indices and mechanical performance indices were not established. Our results show that dinosaurian trabecular bone volume fraction is positively correlated with body mass unlike what has been observed in extant mammalian and avian species previously. However, when data from mammalian and avian species is limited to trabecular bone from the femoral and tibial condyles for direct comparison to samples in this study, they too demonstrate positive correlation between bone volume fraction and animal mass. Additionally, trabecular spacing is negatively correlated with body mass while connectivity density is positively correlated with body mass in dinosaurs. These trends exhibit opposite behavior of the trends observed for extant mammalian and avian species. Despite these differences, it was found that both mammalian and dinosaurian trabecular bone architectures limit average trabecular tissue strains to under 3,000 microstrain for estimated high levels of physiological loading. Interestingly, mammalian trabecular bone was found to limit strains by

increasing trabecular thickness while dinosaurian trabecular bone limits strains by increasing connectivity density.

One limitation of this study is that human trabecular bone mechanical properties were used in the finite element models because it was impossible to know the mechanical properties of the fossilized bone samples. Despite this assumption, our findings are insightful because using the same mechanical properties across all finite element models allows for direct comparison between the trabecular architectures of these animals. However, it should be recognized the fossilized samples could have had different material properties in life due to factors such as differences in mineral content. Another limitation with this study is the relatively low number of samples. This was due to the limited amount of dinosaur and mammoth bone samples available for assessing trabecular bone architecture. With that said, our results are insightful as this is the first study to assess relationships between trabecular bone architectural indices and mechanical behavior in dinosaurian species. A third limitation is that the exact mass of each species was unknown. While current estimates of species masses likely provide reasonably accurate values for the context of this study, a lack of individual sample masses limits the power of the regression analyses. Despite these limitations, we found the trabecular bone allometry in dinosaurian species exhibits allometric scaling with opposite behavior, except bone volume fraction, compared to extant mammalian and avian species, apparent trabecular bone stiffness is positively correlated with body mass in dinosaurian species, and dinosaurian and mammalian trabecular bone architecture limits average strains to below 3,000 microstrain. These findings provide insight into how trabecular bone in the distal femur and proximal tibia adapted to support extremely large body masses.

The allometric scaling relationships show how the trabecular bone architectural indices scale with body mass in dinosaurian, mammalian, and avian species. Unlike previous studies [13], [86], the present research focused only on the trabecular bone from the distal femur and proximal tibia which uncovered some interesting differences. First, the trabecular bone volume fraction in these locations shows positive correlation with body mass for dinosaurian, mammalian, and avian species (Figure 2-10). These results contrast previous findings that showed no correlation between bone volume fraction and body mass when looking at numerous skeletal locations together [11], [13]. Skeletal locations in previous studies included the calcaneus, femoral condyles, head, trochanter, and neck, proximal and distal tibia, vertebrae, radius, ulna, iliac crest, and humerus. It is possible that our results for the distal femur and proximal tibia differ from previous results due to differences in mechanical loading at each location. Trabecular bone in the distal femur and proximal tibia have been shown to have similar architectural properties [84] and therefore may have adapted differently than trabecular architectures in other bones to accommodate their specific mechanical loading conditions. Second, no correlation between trabecular thickness and body mass was observed for dinosaurs while a positive correlation was observed for mammalian and avian species Figure 2-10. Previously, it has been shown that larger body mass animals have greater trabecular thickness to prevent individual trabeculae from being overly strained [11]. The fact that dinosaur trabeculae do not follow this trend is an interesting result and suggests other trabecular bone indices may adapt to provide increased mechanical competence instead. In support of this theory, we have shown that trabecular spacing and connectivity density were negatively and positively correlated with body mass, respectively, in the dinosaurian species (Figure 2-11 & Figure 2-13). Both trends are opposite of those observed for the avian and mammalian species. Thus, it appears that, as dinosaurs grow larger, decreased trabecular spacing and increased

connectivity density provide sufficient mechanical stability while maintaining a relatively constant trabecular thickness. These trends are further elucidated with results from the finite element models.

Computational models demonstrated positive correlations between body mass and trabecular bone apparent and specific apparent moduli for the dinosaurian species as expected (Figure 2-15 & Figure 2-16). These findings confirm the hypothesis that stiffer trabecular architectures are developed as animal size increases to support greater mechanical loads. Interestingly, this contrasts previous findings which showed no correlation between animal size and apparent modulus of trabecular bone in mammalian species [11]. For dinosaurian species, the apparent and specific apparent moduli are both dependent only on connectivity density. For the mammalian species, trabecular bone apparent modulus is dependent only on trabecular thickness, but specific apparent modulus is dependent on trabecular thickness and spacing together. The dependence of trabecular bone stiffness on trabecular thickness and connectivity density is not novel [17], [19]–[21]. However, it is interesting that increases in bone stiffness were achieved through increased connectivity density in dinosaurs but increased trabecular thickness in mammals. The reason for this is currently unclear, but one explanation could be that high connectivity is a more efficient stiffening mechanism than increased trabecular thickness, especially for the exceptional loads produced by the mass of the largest animals. This idea is analogous to the load sharing utilized by trusses to achieve weight reduction in structural design and may have been used by dinosaurs to constrain whole bone weight and trabecular bone tissue strains.

Despite the allometric scaling of the apparent and specific apparent moduli, we found that the average principal strain magnitudes were not correlated with body mass. Furthermore, average principal strain magnitudes were limited to 3,000 microstrain for all samples in this study. Similar

limits have been previously observed for mammalian bone from a variety of species during routine activities such as running, jumping, walking, and chewing [103]–[108]. Strain limits are achieved as bone remodels in response to mechanical loading [9], [109], [110]. The remodeling process limits high strains to decrease the risk of fracture [107], [111] and low strains to avoid excess bony material in areas where it is mechanically unnecessary [112]. Previous studies on the trabecular architecture in mammalian species suggested that trabecular thickness increased with increasing body mass in order to modulate the strains experienced in individual trabeculae [11]. In the case of dinosaurian species, it appears that an equivalent result is achieved by increasing connectivity density instead of trabecular thickness. This result is like what was observed for the apparent and specific apparent moduli of each species. It is unclear why dinosaur bone adapted to have higher connectivity density instead of increased trabecular thickness; however, as mentioned previously, it's possible that this mechanism of strain modulation more efficiently balances the structures mechanical competence and weight.

The present study provides evidence of how trabecular architecture supported large body masses. However, it must be considered that dinosaurian trabecular tissue may differ from extant mammalian trabecular tissue on a compositional level which would have implications for the mechanical behavior of this tissue [113]–[124]. However, due to the fossilization of dinosaur bones, this cannot be accurately assessed. Either way, using the same material properties in direct comparisons of bone architectures showed that dinosaur trabecular bone apparent modulus and bone volume fraction are positively correlated with body mass. Additionally, the trabecular bone apparent modulus shows strong dependence on trabecular bone connectivity density in dinosaurian species. Taken together, it is concluded that the trabecular architecture in dinosaurs evolved to maintain bone stiffness and modulate strain levels to prevent failure across a wide range of body

masses. Our data also demonstrate that changes in connectivity density were the primary mechanism for dinosaur bone adaptation. However, at this point, it is unclear why dinosaurs altered connectivity density to achieve this result instead of adjusting trabecular thickness like mammals. We suggest that increasing connectivity is a more efficient stiffening mechanism than increasing strut thickness for animals of this extraordinary size. This would have allowed for sufficient mechanical competence to be achieved with less bone material (i.e. minimizing the metabolic cost of maintaining and transporting bony material). These findings have potential implications for novel bioinspired designs of stiff and lightweight structures that could be used in aerospace, construction, or vehicular applications.

2.4 Conclusions

- Distal femur and proximal tibia trabecular bone volume fraction is positively correlated with body mass in mammalian, avian, and dinosaurian species.
- Dinosaurian trabecular spacing, trabecular number, and connectivity density show allometric scaling behavior opposite of extant avian and mammalian species.
- Dinosaurian trabecular bone increases stiffness by increasing connectivity density while mammalian trabecular bone increases trabecular thickness
- Dinosaurian and mammalian trabecular bone was found to limit trabecular tissues strains below 3,000 microstrain for estimated high levels of physiological loading.

Chapter 3: Introduction: Bighorn Sheep velar architecture

3.1 Bighorn Sheep and bioinspired structures

High-energy impact causes substantial damage to structures (e.g., vehicles) and humans (head and joints). Rocky Mountain bighorn sheep (*Ovis canadensis canadensis*) routinely experience repetitive high energy cranial impacts for up to several hours per day during mating season, which lasts several weeks [125]. During impact, the horn experiences forces of up to 3,400 N [126], and bending stresses ranging from 1 to 6 MPa in tension and 1 to 7 MPa in compression [127]. After impact, the ram may seem momentarily stunned but otherwise show no long term ill effects from ramming [125]. The keratinous horn material has been reported to have high work of fracture to prevent catastrophic failure during loading [128]. To supplement the outer keratin layer, the bony horncore has been shown to play a large role in energy absorption during simulated quasi-static [129] and dynamic [130] loading conditions and reduce brain cavity accelerations during impact [130]. The unique architecture of the horncore is made up of a foam-like bone structure composed of sail-like features (i.e. velar bone), which differs from the more rod-like structure of trabecular bone. Trabecular architecture is typically characterized by trabecular thickness, spacing, and number, connectivity density, and bone volume fraction. Analogously, velar bone can be characterized by velar thickness, spacing, and number, connectivity density, and bone volume fraction. Interestingly, velar bone has a volume fraction comparable to typical trabecular bone (approximately 20%), but individual velae have a thickness of 2.87 ± 0.78 mm, which is approximately 26 times higher than typical trabecular bone struts [102]. There are also about 20 times fewer velae per unit length compared to trabeculae, and the separation between velae is about 20 times greater than the separation between trabeculae. Due to the extreme impact forces generated during ramming, these differences suggest that velar bone architecture may be

evolutionarily adapted to absorb energy during dynamic loading to prevent brain damage. Conversely, human head impacts often result in traumatic brain injury (concussions) [131] and chronic traumatic encephalopathy [132], [133]. To help design head trauma prevention materials and mechanisms, researchers have begun to study bighorn sheep keratin horn and bony horncore to better understand the energy absorption and storage capabilities of these materials. The impact properties of horn keratin [134] and other horn-like structures [135] have been studied, but these results have yet to be applied to developing a bio-mimicked material or structure. Bio-mimics for armor and structural applications have been successfully developed for natural impact resistant and energy-absorbing materials such as nacre [135]–[141], mantis shrimp dactyl club [142], [143], woodpecker skull [144], conch shell [145], and beetle shell [146], but not bighorn sheep horns. Thus, mimicking the velar bone architecture may lead to novel structures optimized for weight-efficient energy absorption for impact applications.

3.2 Motivation for research

Helmets are used to prevent injury during almost all sport activities (recreational, occupational), during travel (motorcycles, bicycles), and have additional occupational (construction, military) uses as well. There are approximately 800 million bicycles worldwide and half as many cars. In many countries bicycle related injuries are not recognized as a road safety problem and thus, attract little to no research. In Beijing China one-third of all traffic related deaths occur among cyclists [147]. In Sweden, risk of cyclist injury is 6 times higher than the risk of injury as a motorist where cyclists make up the majority of injured road users since 2008 [148] and in the US cyclist related accidents result in 81,000 emergency room where 77% patients experienced traumatic brain injury [149]. In a study high school football practices and games, it was found that impact accelerations, ranging from 70 to 98g an experienced by defensive line

players [150]. At the collegiate level, impact accelerations are reported to be 103g [151], while concussions have been reported to occur as low as 56g [152] and as high as 146 g [153]. Military helmets see the harshest physical environments and widest range of protection needs. These helmets must provide soldiers with protection from blunt impact as well as stop high velocity projectiles (shrapnel and bullets) [154]. These impact velocities can be as high as 477 m/s for 9mm rounds and 413 for steel ball bearings simulating improved explosive devices [155]. Research to improve impact attenuation of bicycle helmets using aluminum honeycomb has been investigated but suffers from plastic deformation [149] and therefore needs material improvement. Reports of high impact materials in military helmets has been reported but no investigation of the geometry of the structure used [155]. Improvements in material and geometry have been reported in football helmets, however, no data has been provided publicly [156].

Athletic footwear (e.g., running/tennis/basketball shoes and hiking/climbing/military boots) have a variety of purposes and mechanical needs for effective and optimal performance, but all have impact in common. Running generates vertical ground reaction forces of 2.5 - 3x bodyweight [157], [158], and joint reaction forces of 3.6 - 4.2x bodyweight in the knee [159], [160], and as high as 10x bodyweight in the hip [161]. The ground reaction force may be up to 4.6x bodyweight for moderate impact jumping [162] and up to 11.6x bodyweight during higher impact jumping [163]. These impact forces are exacerbated in military personnel whose effective body mass is higher because of additional gear (~22 kg) [164]. These high forces from physical activity have been associated with tibial stress fractures [165], damage to soft tissues [166], and running-related injuries costing between $28.8 and $37.2 billion annually to individuals and insurance companies in the United States [167]. It has been hypothesized that running-related

injuries can be reduced if shoes are better designed to 1) limit excessive forces, 2) support the foot during standing, and 3) guide the foot to the ground [168].

Running shoe midsoles have traditionally been made from ethylene-vinyl acetate (EVA) because of its durability and low density [169] and resistance to degradation [170]. More recently, polyurethane foam has been used in running shoe midsoles because of its long term mechanical properties (low creep) [171], [172]. EVA foams are typically made through traditional foaming techniques where a physical or chemical blowing agent creates gas pockets that produce a random closed-cell architecture [173]. Typical cell sizes in these stochastic foams are on the order of 7-11 microns [174]. It has been shown that the average cell size and uniformity of the cells (distribution and size) are two important parameters to control for mechanical property enhancement [174]. For impact applications, the primary mechanical properties of interest are the maximum impact force and the energy absorption. During typical impact tests performed per ASTM F1976 [175] on EVA foams, the maximum impact force is 985-992 N and the energy absorbed is 2-7 J [176]. That study used whole shoes (size 8.5 US) but only the heel was subject to impact. Other studies have shown that midsoles that are either too stiff or too compliant can increase impact forces during running. Stiffer midsole materials increase impact force because they do not provide enough deformation (i.e. the foot is slowed down too quickly) and more compliant materials increase impact force because the foot is not slowed down sufficiently during impact [177]. Measured under a variety of testing methods and shoe types, midsole stiffness was found to be between 30-439 N/mm [171], [176]–[178]. These studies suggest that lower stiffness midsoles provide better cushioning (i.e. more energy absorbed) but experience high impact forces because the foot is not slowed down fast enough. These findings imply that there is a balance between midsole compliance and impact force minimization.

In the United States fatal crashes had been declining since 2005, but has begun to climb since 2014 [179]. To a degree, these deaths can be mitigated through better passive safety systems in automobiles. One such passive system is the bumper subsystem where, a foam and beam are used to absorb a portion of the kinetic energy during impact [180]. Since the bumper beam absorbs most of the impact energy this component is an ideal candidate for improvement in vehicle passive safety systems. FEA results have shown methods to optimize the external geometry of metallic hollow shape structures used a car bumper beams [181]–[183], however these studies are theoretical with no physical experimentation performed. Other research has shown conceptual methods for improving polymeric bumper beam impact performance [184] and FEM and experimental results show good agreement for functionally graded steel foams [185]. The previously cited student utilized a standard box shape for the external bumper beam geometry filled with the steel foam. Though these results show high impact performance, further research should be performed into designing the cellular structure of these metallic foams for enhanced impact performance.

3.3 Hypotheses

Because Rocky Mountain bighorn sheep routinely engage in high-impact intraspecific combat, it is hypothesized that velar architecture can be biomimicked for use as novel cushioning system. The specific hypothesis of this study are as follows:

1. 3D printed velar mimic structures will reduce impact accelerations compared to commercial materials and will more effectively store energy during impact
2. Finite element models of the velar bone mimics can be utilized to identify a new unit cell to generate new velar bone mimics with improved performance as compared to the initial velar bone mimic design.

Chapter 4: Velar bone mimic development [2]

4.1 Methods

4.1.1 Bighorn sheep velar bone architecture

Velar architectures were obtained from five male bighorn sheep skulls, which were provided for research purposes by the state of Colorado Department of Natural Resources under Colorado Parks and Wildlife scientific collection license number 14SALV2052A2. The skulls were obtained from sheep that were killed by motor vehicle accidents and frozen shortly after death. Thus, Colorado State University's Research Integrity and Compliance Review Office determined the research was exempt from Institutional Animal Care and Use Committee oversight. The skulls were scanned using a Gemini Time-of-Flight Big Bore PET/16 slice CT scanner (Philips Healthcare, Andover, MA, USA). Scan voltage was 140 kV, current was 321 mA, and time was exposure 350 mAs . The architectures for the velar bone mimics (VBMs) were created from the left horn from five different sheep with horn curl lengths ranging from 0.55 to 0.95 meters. Sections of the velar architecture were cropped from the regions of high compressive stress in the horncore [130]. These regions were chosen for the mimics because running shoes experience compressive loading during standing and gait. The region of interest (ROI) for each horncore was

[2] This dissertation chapter was adapted with permission from Aguirre, T. G.; Fuller, L.; Ingrole, A; Seek, T. W.; Wheatley, B. W.; Steineman, B. D.; Haut-Donahue, T. L.; Donahue, S.W. Bioinspired material architectures from bighorn sheep horncore velar bone for impact loading applications, Scientific Reports, *In Review*.
Funding for velar bone mimic development was provided by the Colorado Office of Economic Development and International Trade.

a 45mm cube, which maximized the amount of velar bone that could consistently be utilized from the compressive region of the horncore from each sheep. Bighorn sheep velar architecture and the velar bone ROI are shown in Figure 4-1.

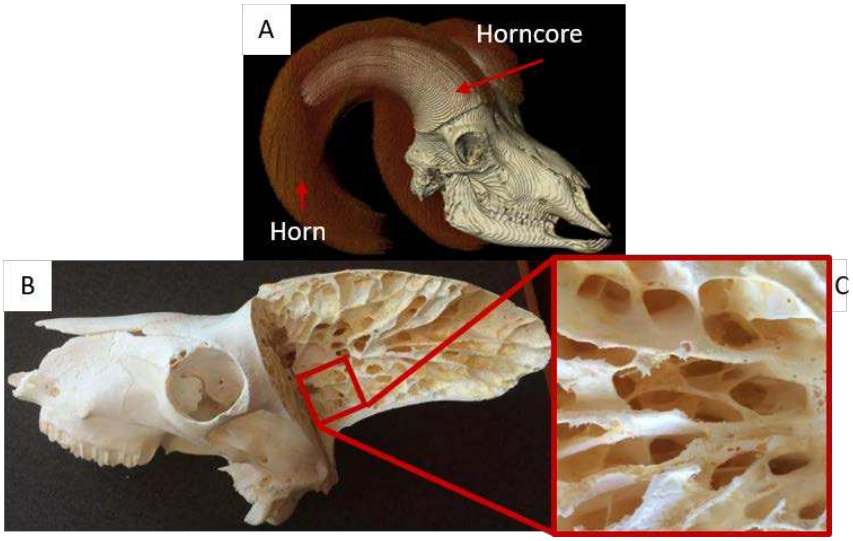

Figure 4-1: A) Horn and horn core spatial arrangement, B) horn core longitudinal-section showing the velar bone inside the thin cortical shell, C) velar structure in the compressive region of the horncore

4.1.2 **Velar architecture quantification**

Velar bone architectural index measurements are depicted in Figure 4-2 and were measured using BoneJ [86]. The velar bone volume fraction (BV/TV) is the volume of bone (BV) normalized by the total volume (TV) of the velar bone ROI. The velar thickness (V.Th) is the average thickness of all velae within the ROI. The velar spacing (V.Sp) is the average linear distance between two velae. The velar number (V.N) is the number of velae per unit line length. The connectivity density is the total number of connections between two or more velae normalized by the volume of the ROI.

Figure 4-2: Velar bone architectural indices: velar thickness, V.Th (green arrows), velar separation, V.Sp (purple arrow), velar number, V.N (blue lines and crosses), TV (red square), and Conn.D (orange circles).

4.1.3 **Bighorn Sheep velar bone mimic generation**

First, velar architecture was isolated in each CT scan from the horncore compressive region (Figure 4-3), which was identified from a finite element model study sheep ramming [130].

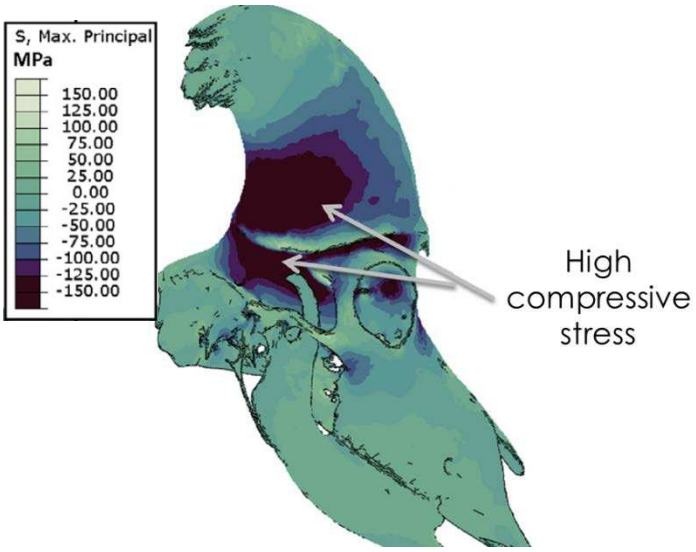

Figure 4-3: Compressive region of horncore during impact. Image adapted from **[130]**

After velar bone architecture was quantified, each ROI was cropped out of the CT scans to generate 3D models of the velar bone mimics (VBMs). First, Seg3D (version 2.2.1, University of Utah, Salt Lake City, UT, USA) was used to separate the bony horncore and horn keratin using manual binary thresholding operations (Figure 4-4A). Due to contrast differences in the images that compose the DICOM files, small perforations in the velar structure were inevitable and needed minor repair Figure 4-4B). These perforations were repaired by manually adding pixel values to the threshold layer (Figure 4-4D & E). VBMs were only repaired in CT scan regions where it was evident that bony material was displayed within the CT images yet there were no pixel values in the threshold layer (Figure 4-4D). Finally, the repaired velar structure (Figure 4-4C) was saved in the ASCII STL file format for further mimic preparation.

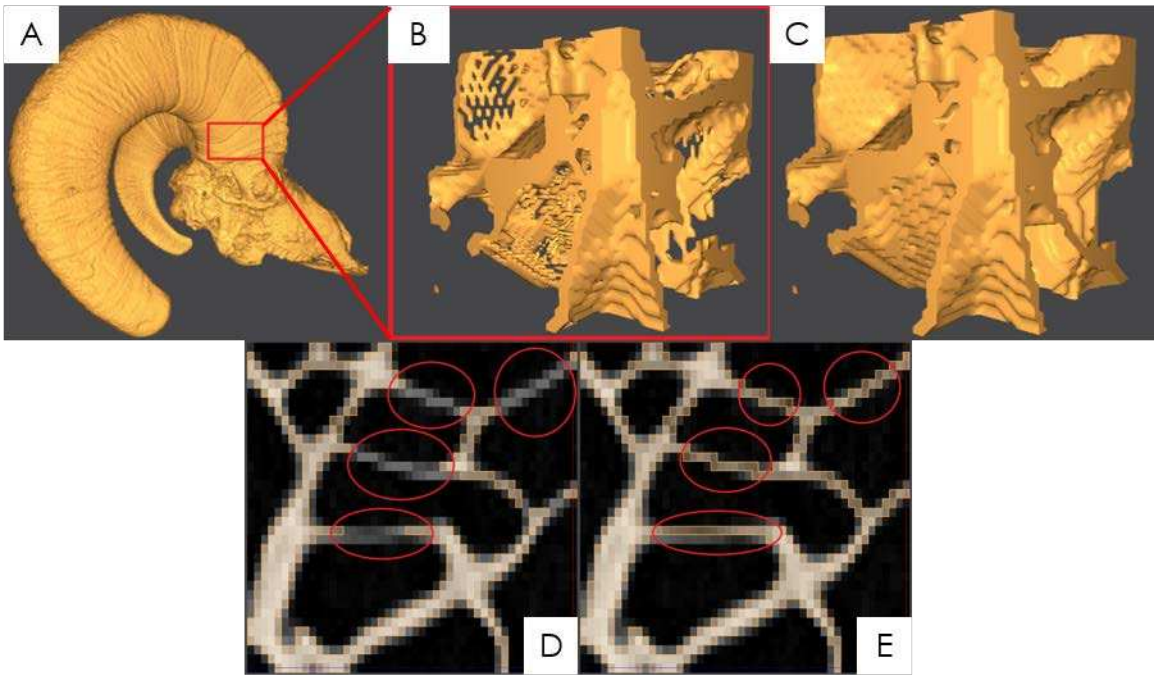

Figure 4-4: A) Binarized ram skull, B) velar cube cropped from the compressive region of horncore indicated in A, C) repaired velar cube, D) velae perforations in threshold mask layer, E) repaired perforations in the threshold mask layer.

MeshMixer (version 3, San Rafael, CA, USA) was used to isometrically scale the 45x45x45 mm cube (Figure 4-5A) to produce 20x20x20mm unit cell (Figure 4-5B), which were then mirrored across two mirror two planes to produce a 40x40x20mm geometry (Figure 4-5C). Scaling and mirroring provided mimic structures that preserved the natural velar bone architecture and were approximately the same thickness as a running shoe midsole. Additionally, this process allowed us to achieve continuum dimensions using only velar bone from the compressive region of the horncore. For trabecular bone, continuum dimensions have been estimated to be at least five trabecular spacings [88], therefore we assumed five velar spacings were adequate for the velar bone mimics. These mimicked geometries were exported in the ASCII STL file format for further processing.

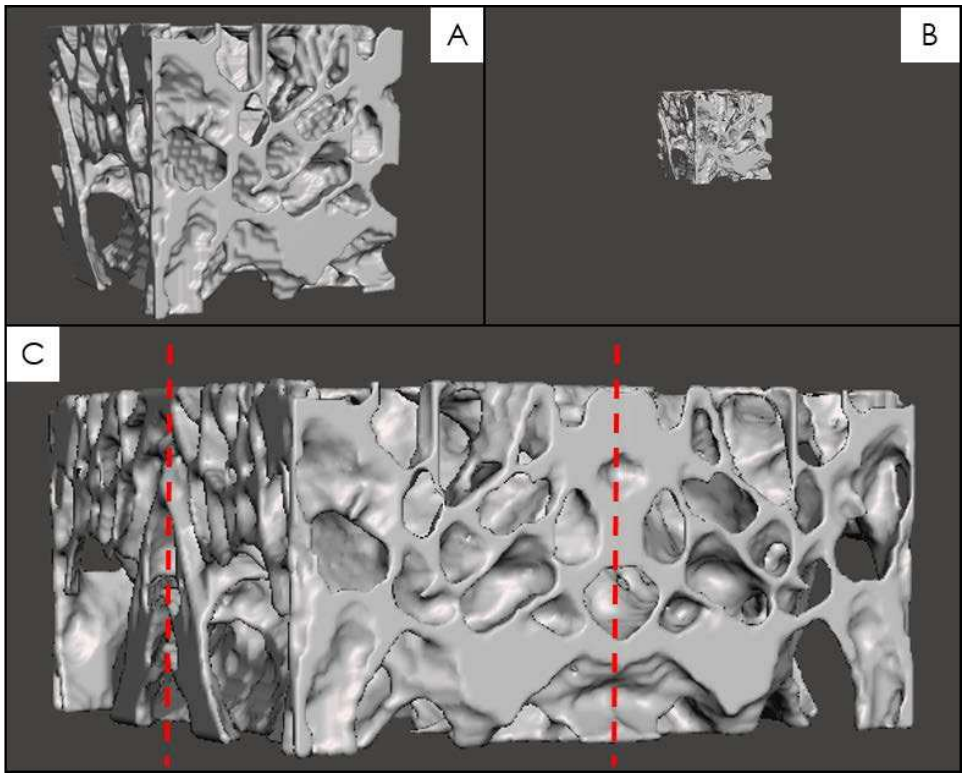

Figure 4-5: A) 45x45x45 mm unit cell cube cropped from compressive region of horncore and saved in ASCII STL file format, B) 20x20x20 mm scaled cube, C) mirrored scaled cube to produce 40x40x20 mm mimic structure. The dashed red lines in C) indicate lines of symmetry.

NetFabb (Autodesk, San Rafael, CA, USA) was used to further repair the mimic STL files using automated operations to fix errors during the surface triangulation process (i.e. remove duplicate and penetrating faces). In this step, a 2mm thick plate was added to the top and bottom to create a sandwich structure (Figure 4-6) to better approximate loading conditions of the velar bone mimic during use as a midsole. After repair, the final files were exported in the ASCII STL file format to be used in mesh generation for the FEA study and additive manufacturing.

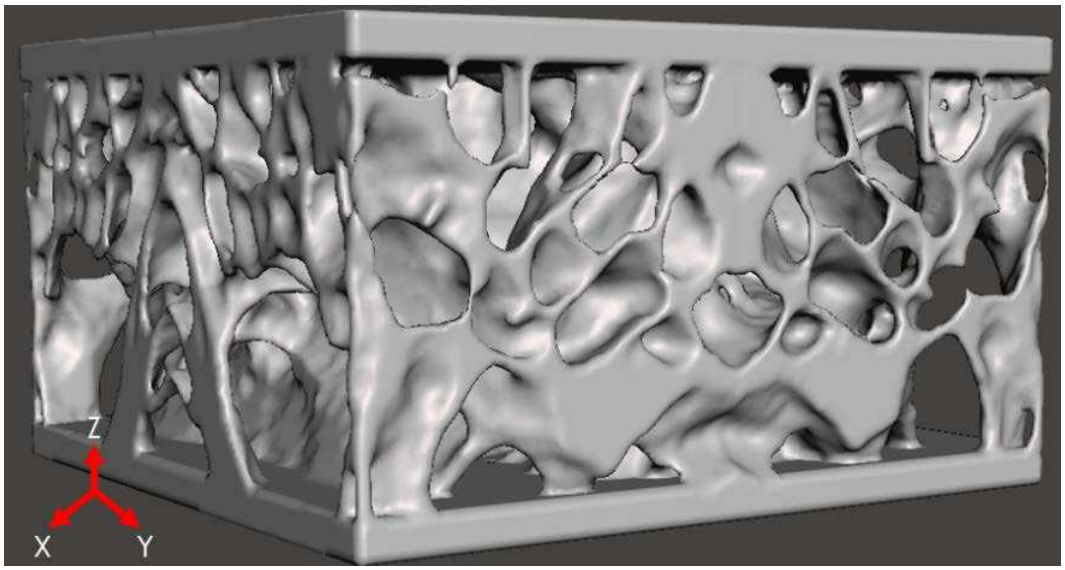

Figure 4-6: Velar bone mimic sandwich structure after STL file repair

4.1.4 **Velar bone mimic manufacture and mechanical test specimen**

The novel velar bone mimics developed in section 2.3 were 3D printed on a Carbon Speedcell™ using Elastomer Polyurethane (EPU) #40. Mimics were manufactured by Ramaco Carbon (Sheridan, WY, USA) and printed with 75-micron resolution in the x-y plane and 100-micron layer thickness where the build direction was coincident with anatomical loading during impact (z-direction Figure 4-6). For comparison to the velar architecture, three running shoe EVA

foams were tested. Running shoe midsole high-density (HD), medium-density (MD), and low-density (LD) EVA foam samples were mechanically tested to compare to the EPU VBMs. Seven coupons of each EVA foam and each VBM were used for both static and dynamic tests. All test coupons were 40x40x20 mm.

4.1.5 **Quasi-static compression testing**

Quasi-static compression tests were performed using a hydraulic load-frame (Instron model 8501, Norwood, MA, USA) in displacement control per ASTM D1621 [186]. Crosshead displacement rate was 5 mm per second, samples were compressed to 25% strain (5mm), and then released at 5 mm per second. This displacement was chosen as the maximum allowable displacement to ensure runner comfort [187]. Applied load and crosshead displacement were measured and used to compute energy absorption, specific energy absorption, and stiffness.

4.1.6 **Impact testing**

Dynamic impact tests were performed on custom drop tester (Figure 4-7) inspired by the design presented in ASTM F1976 [175]. The mass of the missile was 8.5 kg and was dropped from a height of 60 mm to provide an energy of 5 Joules at impact. Missile position was measured using a linear displacement transducer (176-0521-L3N, Firstmark Controls, Creedmoor, NC) and impact force was measured using an impact force transducer (200B05, PCB, Depew, NY). Impact force and displacement were used to compute the maximum impact force, energy absorption, and specific energy absorption.

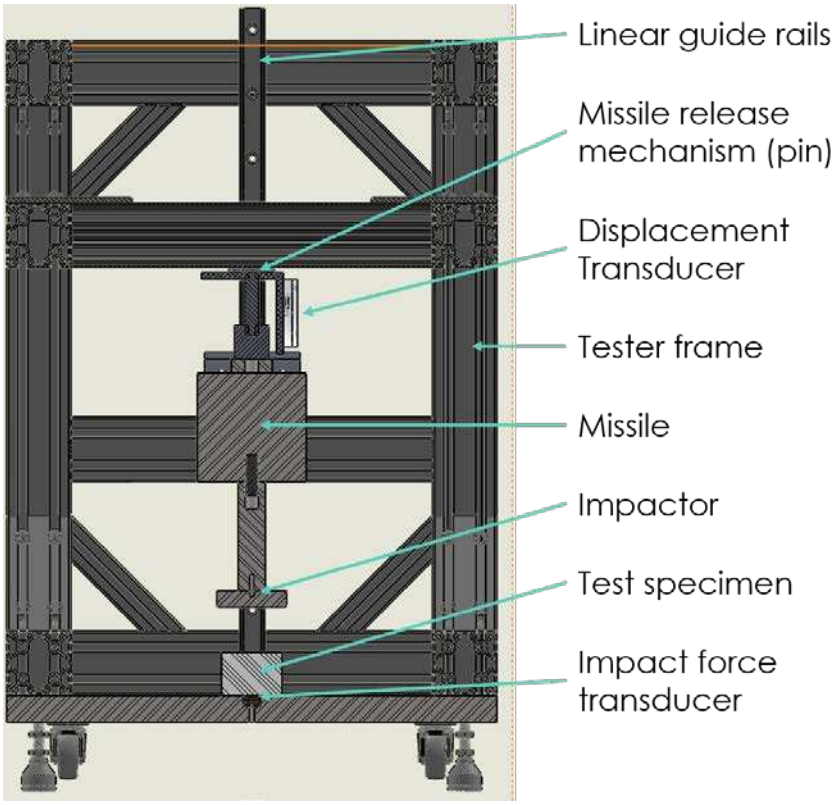

Figure 4-7: Custom designed drop tester

A substantial amount of engineering went into the design, selection of transducers, data acquisition, and assembly of the drop tester. There were two primary engineering problems after the drop tester was fully assembled. The first problem was the original release mechanism was an electromagnet. The solution initially required design of the missile bracket to concentrate the magnetic field and prevent eddy currents. Once this issue was fixed, the transducers attached, and the data acquisition hardware/software connected it became apparent that the electromagnet, when shut off, was causing interference in the collected data. This issue was then fixed by utilizing a mechanical release mechanism. The second problem was the impact force transducer. Initially the transducer would only registers impact forces of 20 N, which was too low for an impactor whose weight is 83. This issue was solved by designing a plate to evenly distribute the force over the measurement surface of the transducer.

4.1.7 **Equations**

Energy absorption (E_A) during quasi-static compression and impact was computed by numerically integrating the force-displacement loading curve (Equation 4-1), where F is the applied force and δ is the displacement.

$$E_A = \int_0^{\delta_{max}} F\delta \, d\delta \tag{4 - 1}$$

Due to differences in the volume of material present in each velar bone mimic and EVA foam, the specific energy absorption (W_s) was computed by numerically integrating (Equation 4-2 [188]). Where ϵ_{max} is the maximum strain, $\sigma(\varepsilon)$ is the stress at each value of the strain, $\Delta\rho$ is the relative density of the foam (BV/TV is equivalent), ρ_s and is the density of the material that the foam is comprised of.

$$W_s = \frac{\int_0^{\epsilon max} \sigma(\varepsilon) d\varepsilon}{\Delta\rho\rho_s} \tag{4 - 2}$$

4.1.8 **Finite element model generation for velar bone mimics**

Velar bone mimics were meshed in ICEM CFD (version 18.1, ANSYS, Canonsburg, PA, USA) to generate a linear triangular shell (S3) mesh and analyzed using Abaqus FEA (Dassualt Systems, Vélizy-Villacoublay, France, EU). Shell elements were chosen because these elements can accurately model the behavior of cellular solids in finite element models [188]. Shell element thickness varied between each velar bone mimic due to intrinsic differences in velar thickness between animals but did not vary within an individual finite element model. Quasi-static compression was simulated for each structure by placing the velar bone mimics between two rigid plates, applying an encastre boundary condition to the bottom plate, and allowing the top plate to translate in the z-direction only (Figure 4-8). From the starting configuration, the top plate was displaced at 5 mm per second for a total displacement of 5mm to simulate the mechanical testing

procedure. All finite element models used linear elastic material properties. For each velar bone mimic, the shell thickness was iterated until the simulated stiffness closely matched the experimentally measured stiffness [189]. Self-contact was used to capture the behavior of contact between locally buckled velae. In Abaqus, the interaction property was set to "ALL WITH SELF" using the general contact option. The tangential behavior was set with a friction penalty of 0.2 and normal behavior was set to hard contact [188]. To reduce computation time mass scaling was utilized; thus, the Dynamic/Explicit solver was used. To avoid small vibrations (oscillatory behavior) in the force-displacement curves caused by mass scaling, minimal damping was used ($\alpha = 1 \times 10^{-5}$) [190]. Models were given the experimentally determined properties of EPU 40 ($E = 6.81$ MPa and $\nu = 0.48$). Optimal mesh density was determined via a numerical convergence study [30], [89]. Five unique mesh densities ranging from 13 to 222 elements per cubic millimeter were created for VBM3, which had the smallest average velar thickness. To determine whether the mesh had converged, the change in strain energy between each mesh was analyzed and compared to the finest mesh as a percent difference using Equation 4-3.

$$\Delta = \frac{X_N - X_i}{X_N} 100\% \tag{4-3}$$

Where Δ is the percent difference and X is strain energy. X_N is strain energy for the finest mesh in the mesh convergence study and X_i is the strain energy for the other meshes used in the study. Convergence was achieved at a mesh density of 188 elements per cubic millimeter, which had a 2.16% difference from the finest mesh density of 222 elements per cubic millimeter.

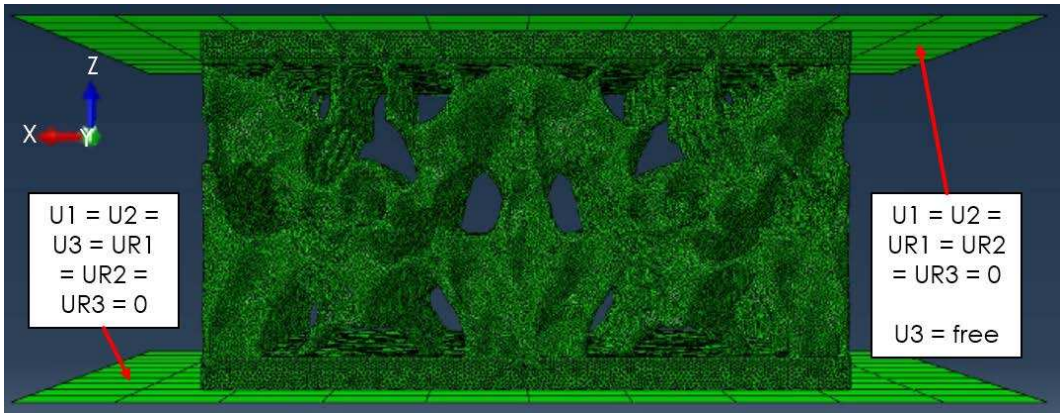

Figure 4-8: Velar bone mimic finite element model meshed with triangular shell (S3R) elements

4.1.9 **Velar bone mimic iterative design process**

After validating the finite element models with data from the quasi-static compression tests of the first-generation velar bone mimics, an iterative design process was used to improve the mechanical performance of the VBMs. Specifically, we wanted to increase energy storage, reduce impact force, and satisfy the stiffness requirements. We hypothesized that second generation VBMs made with new unit cells from the regions with the highest strain energy storage in the original VBMs would have improved energy absorption. We chose the quasi-static stiffness values of the HD and LD EVA foams as the upper and lower stiffness limits for the second generation VBMs. The iterative design process is depicted in Figure 4-9. First-generation VBM finite element models were visually interrogated to identify regions with the highest strain energy storage, as reported by the Abaqus strain energy color maps (Figure 4-9A). Regions with the highest energy absorption were visually correlated back to the original unit cell STL file and then isolated within the original unit cell (Figure 4-9B). The new unit cell was then used to construct the second generation of velar bone mimics (Figure 4-9C). Second-generation VBMs were then subjected to the same finite element modeling procedures as the first-generation VBMs (Figure 4-9D). Stiffness of second-generation VBMs were then compared to the EVA foam stiffness constraints (Figure

4-9E). This process was iterated until second-generation VBMs stiffness were within the range of the EVA foam stiffness constraints. These second-generation mimics were named as VBM-2G, and unit cell size ranged from 32-256 unit cells per mimic.

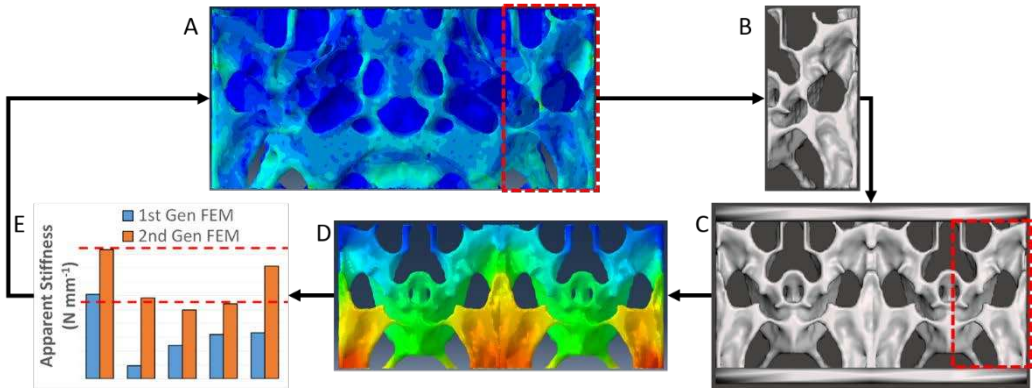

Figure 4-9: A) Unit cell encompassing regions with highest energy storage, B) isolate unit cell, C) generate 2nd gen VBM, D) finite element model, E) compare to experimental quasi-static compression results.

4.1.10 **Statistical analyses**

The velar bone architectural indices (BV/TV, V.Th, V.Sp, V.N, and Conn.D) were compared to trabecular bone architectural indices from the distal femur and proximal tibia of human [13] and sheep [11], [13], [191]–[193]. These anatomical locations were chosen because they experience impact loading during physical activities such as running and jumping. Analysis of variance (ANOVA, $\alpha = 0.05$) was used to compare the porous bone architectures of each species. Stepwise regressions ($\alpha = 0.05$) were used to determine the influence of velar architecture on mechanical performance of the VBMs during the compression and impact tests. For the stepwise regressions, the candidate independent variables were V.Th, V.Sp, and Conn.D measured from the velar bone mimics. V.N and BV/TV were excluded from the regression models to avoid collinearity since they are both correlated with V.Th, V.Sp and Conn.D. For the quasi-static compression tests, the dependent variables were stiffness, energy absorbed, and specific energy

absorbed. For the impact tests, the dependent variables were the maximum impact force, energy absorbed, and specific energy absorbed. ANOVAs ($\alpha = 0.05$) were used to compare from the VBMs and EVA samples for the impact and compression tests. The stepwise regressions and ANOVA were performed in Minitab (version 18, State College, PA, USA). Linear regressions were performed on the impact force and stiffness for EVA foams, the first-, and second-generation VBMs.

4.2 Results

4.2.1 Velar bone architectural quantification from large horncore section

Shown in Table 4-1 are the results of the velar bone architectural parameter quantification with the results of the single factor ANOVA. It is seen that there are no statistically significant differences between the compression region of left and right horns of these sheep when comparing the BV/TV, the velar number, velar spacing, and velar thickness. As result of this, only the left horn was used to generate velar bone mimics for mechanical testing and finite element models.

Table 4-1: Velar bone architectural indices from large horncore section

Sheep	BV/TV		Velar # (1/mm)		Velar Spacing (mm)		Velar Thickness (mm)	
	LH	RH	LH	RH	LH	RH	LH	RH
1	11.77%	15.50%	0.0723	0.0782	14.1205	13.5492	2.0884	1.7921
2	16.01%	17.52%	0.0650	0.0843	15.8386	11.7423	1.8973	1.8577
3	12.22%	13.61%	0.0939	0.0915	10.7882	10.9695	1.3874	1.4860
4	18.74%	16.10%	0.0929	0.0843	10.9511	12.7487	2.1321	2.1436
5	18.34%	15.51%	0.0761	0.0564	13.5029	18.2524	2.1683	2.2828
***p* - value**	0.72		0.79		0.76		0.86	

LH = left horn, RH = right horn

4.2.2 **Velar bone architectural quantification from isolated region of interest from the compressive region of the horncore**

Velar architectural index measurements are presented in Table 4-2. Velar bone volume fraction was not significantly different from human ($p = 0.992$) and sheep ($p = 0.851$) trabecular bone volume fraction. However, significant differences were found between velar thickness, spacing, number, and connectivity and trabecular thickness, spacing, number, and connectivity for sheep and humans ($p \leq 0.001$ for all).

Table 4-2: Velar bone architectural index measurements from isolated region of interest

Sheep	BV/TV (%)	V.Th (mm)	V.Sp (mm)	V.N (mm^{-1})	Conn.D (mm^{-3})
1	33.14	1.91	5.51	0.19	0.00041
2	21.11	1.40	11.12	0.18	0.00089
3	26.17	1.73	7.05	0.26	0.00068
4	29.72	1.71	6.01	0.29	0.00035
5	30.20	1.67	5.99	0.29	0.00022
Mean ± SD	28.07 ± 4.61	1.68 ± 0.18	7.13 ± 2.3	0.24 ± 0.05	0.00051 ± 0.00027

4.2.3 **Finite element modeling**

4.2.3.1 Mesh convergence

Shown in Figure 4-10 and Table 4-3 are the mesh (numerical) [89] convergence study results for sheep #2. This sheep was chosen because this geometry has the smallest average velar thickness. Figure 4-10 shows that 188 elements per cubic millimeter is a sufficient mesh density (2.16% difference in total internal strain energy from the finest mesh). Therefore, our assumption is that this mesh density was sufficient for velar bone mimics with larger velar thickness and was used because of decreased computation time for meshing and FE simulations.

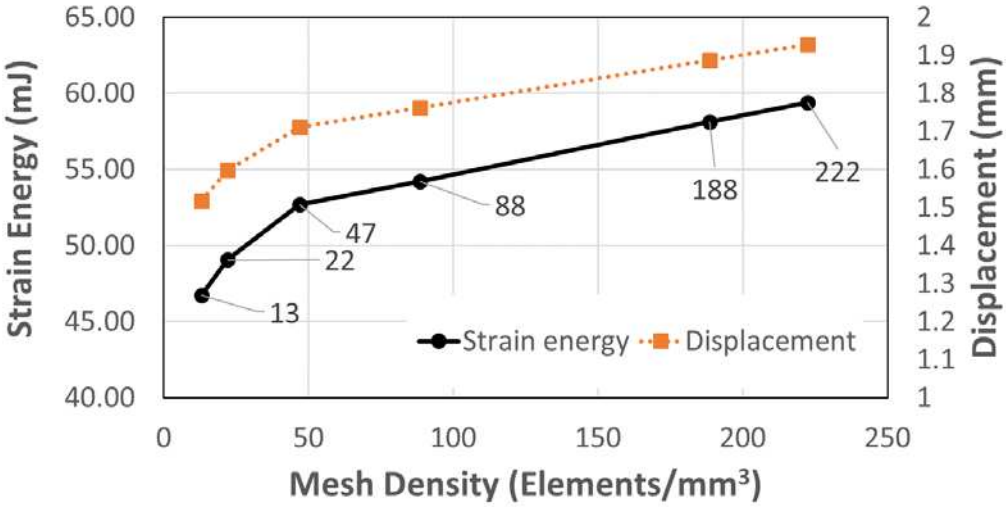

Figure 4-10: FEA mesh convergence study

Table 4-3: Mesh convergence study

Study #	Mesh Density (Elements/mm³)	Displacement (mm)	Displacement (% difference)	Strain Energy (mJ)	Peak Energy (% difference)
1	13	1.517	21.32%	46.7452	21.31%
2	22	1.597	17.17%	49.0901	17.36%
3	47	1.71	11.31%	52.7017	11.28%
4	88	1.761	8.66%	54.2043	8.75%
5	188	1.887	2.13%	58.1200	2.16%
6	222	1.928	0.00%	59.4010	0.00%

4.2.3.2 Finite element model validation

Simulated and experimentally measured stiffness showed excellent agreement, where the largest percent error was 0.64%. However, simulated energy absorption was much lower than the experimentally measured energy absorption with differences as large as ~60%. Energy absorption differences can be attributed to differences between the shape of the force-displacement curves. The finite element modeling results are shown in Figure 4-11.

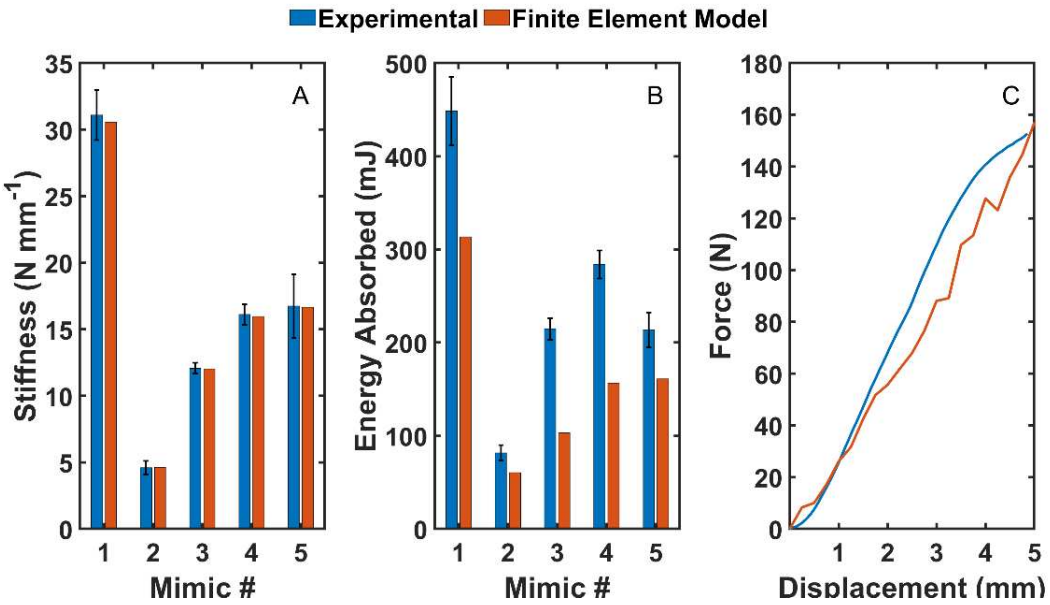

Figure 4-11: First-generation VBM finite element model validation. A) Stiffness, B) Energy absorption, and C) stress-strain curve comparison between finite element model and mechanical compression tests. The black error bars indicate +/- one standard deviation.

4.2.3.3 Finite element modeling of velar bone mimics

Shown in Figure 4-12 are comparisons of the stiffness and energy absorption of the first- and second-generation velar bone mimic finite element models. The results show that after the iterative design process, the second-generation velar bone mimics satisfy the stiffness constraints of the EVA foams and absorbed more energy than the first-generation velar bone mimics.

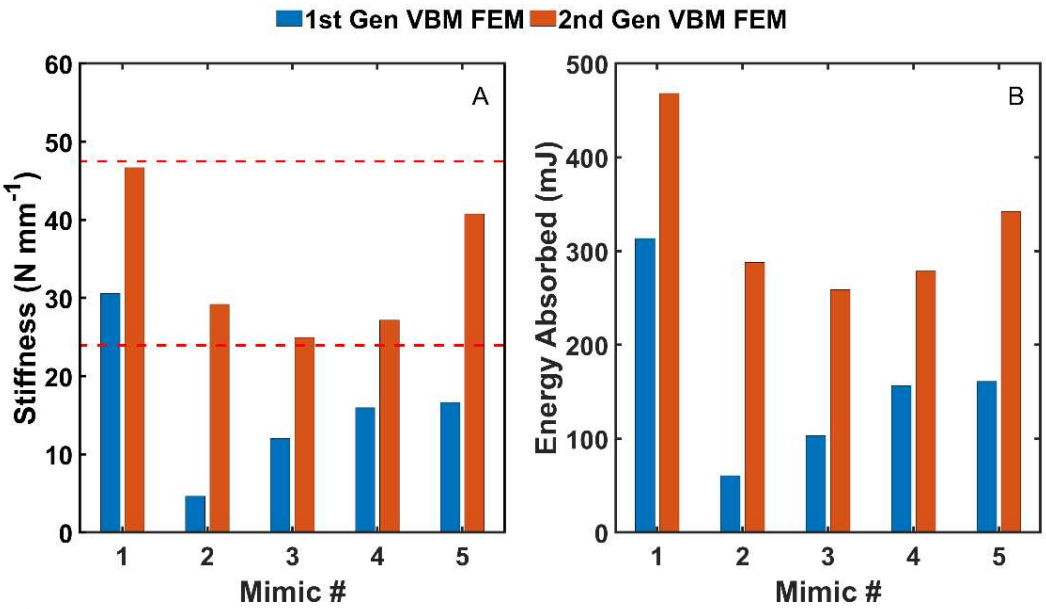

Figure 4-12: First and second generation VBM finite element model comparison. A) Stiffness and B) energy absorbed. The dashed lines indicate the EVA foam stiffness constraints.

4.2.4 **Compression testing**

Figure 4-13 shows stiffness, energy absorbed, and specific energy absorbed for EVA foams and velar bone mimics tested in quasi-static compression. Second-generation VBMs were stiffer than the first-generation velar bone mimics ($p < 0.001$) and EVA foams ($p = 0.001$) while first-generation VBMs were less stiff than the EVA foams ($p = 0.003$) (Figure 4-13A). Similar results were found for energy absorption, where the second-generation VBMs absorb more energy than the first-generation VBMs ($p < 0.001$) and the EVA foams ($p < 0.001$), but first-generation VBMs absorbed less energy than EVA foams ($p < 0.001$) (Figure 4-13B). Finally, EVA foams demonstrated greater specific energy absorption than the first ($p < 0.001$) and second ($p < 0.001$) generation VBMs. However, second generation velar bone mimics showed improved specific energy absorption compared to first-generation velar bone mimics ($p < 0.001$).

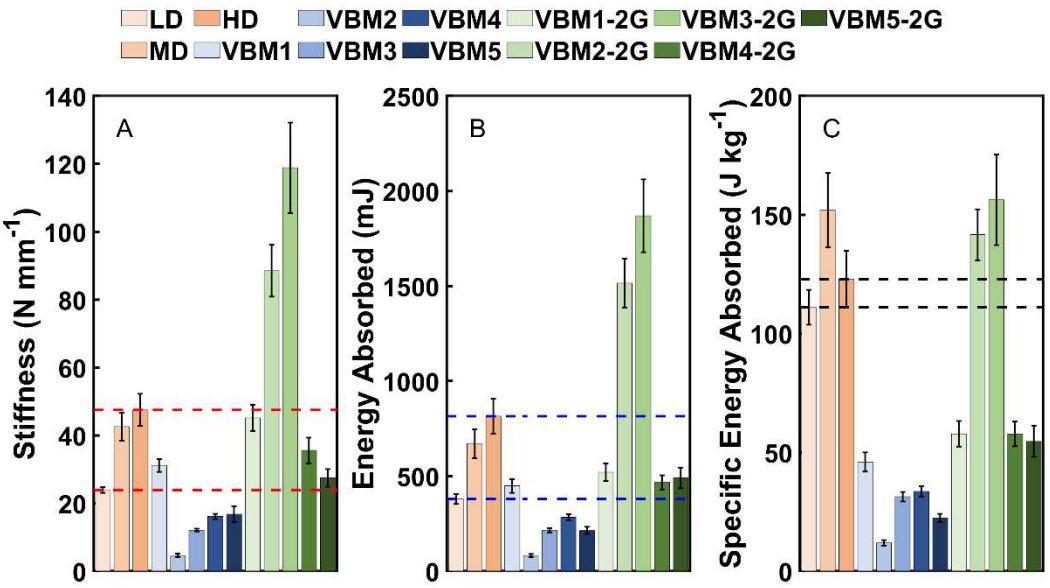

Figure 4-13: Compression test results. A) Stiffness, B) energy absorbed, and C) specific energy absorbed. The black error bars indicate +/- one standard deviation. The dashed lines indicate the ranges for the EVA foams. Red lines indicate design constraint, blue lines indicate value to optimize, and black lines are for comparative purposes.

4.2.5 **Impact testing**

Figure 4-14 shows impact force, energy absorbed, and specific energy absorbed for EVA foams and velar bone mimics tested under dynamic compression. Second-generation VBMs experience less impact force than the first-generation VBMs ($p = 0.001$) and comparable impact force to EVA foams ($p = 0.709$) while first-generation VBMs experience greater impact forces than the EVA foams ($p < 0.001$) (Figure 4-14A). Shown in Figure 4-14B, VBM-2G experience less displacement during impact than VBM-1G ($p < 0.001$) and the EVA foams ($p < 0.001$). Figure 4-14C shows that the first-generation ($p < 0.001$) and second-generation ($p < 0.001$) VBMs absorb less energy than the EVA foams. No significant difference was found between energy absorption of the first- and second-generation VBMs ($p = 0.840$). Figure 4-14D shows that first-generation ($p < 0.001$) and second-generation ($p < 0.001$) VBMs had less specific energy absorption than the EVA foams. However, second generation VBMs showed lower specific energy absorption than

the first-generation VBMs ($p = 0.003$). Lastly, shown in Figure 4-14D VBM-2G experience less displacement during impact than VBM-1G ($p < 0.001$) and the EVA foams ($p < 0.001$).

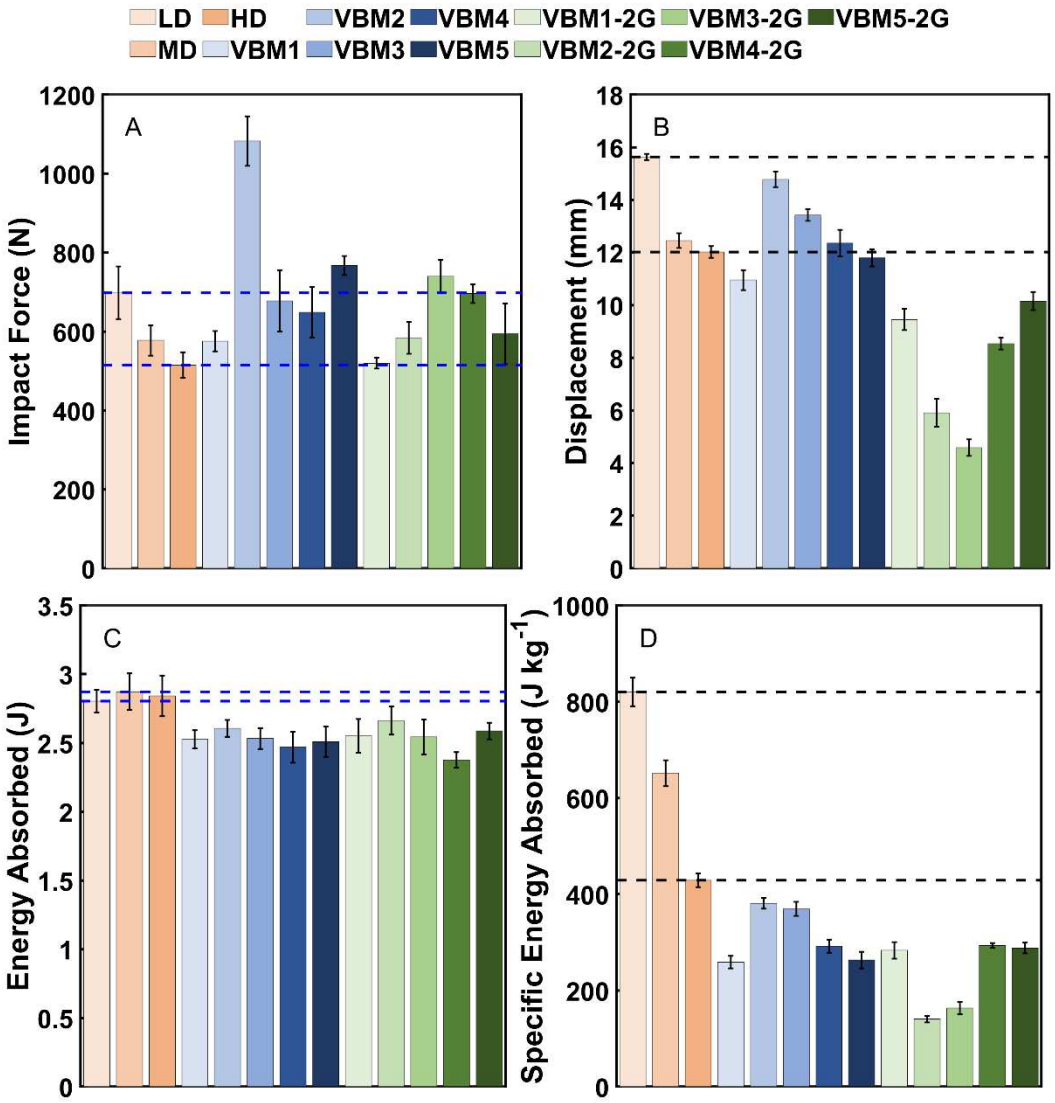

Figure 4-14: Impact testing of shoe foams and velar bone mimics. A) Impact force, B) displacement, C) energy absorbed, and D) specific energy absorption during impact. The black error bars indicate +/- one standard deviation. The dashed lines indicate the ranges for the shoe foams. Blue lines indicate value to optimize and black lines are for comparison purposes.

The relationship between stiffness and impact force was investigated by linear regressions (Figure 4-15). Impact force for the EVA foams (R^2 = 0.743, $p < 0.001$), first-generation (R^2 = 0.577, $p < 0.001$), and the second generation (R^2 = 0.178, $p = 0.057$) VBMs showed negative correlation with stiffness for values of stiffness below 60 N/mm. However, for stiffness above 80 N/mm the second-generation VBMs showed positive correlation with stiffness (R^2 = 0.670, $p < 0.001$). Therefore, first- and second-generation VBMs were grouped for a quadratic regression, which showed a significant ($p < 0.001$, R^2 = 0.502) quadratic relationship (Figure 4-15).

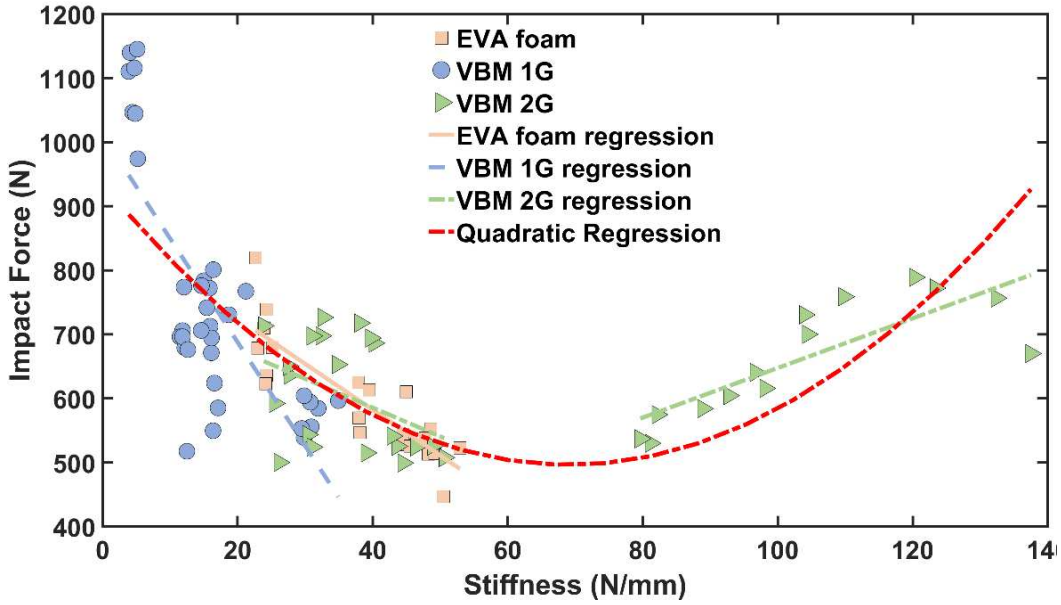

Figure 4-15: Impact force versus stiffness regressions

4.2.6 **Stepwise Regressions**

Strong correlations were found between the velar architectural indices of the VBMs and mechanical testing parameters (Table 4-4). Mechanical performance was positively correlated with velar thickness for both quasi-static compression and impact. Mechanical performance showed negative correlation during quasi-static compression and positive correlation during impact with both velar spacing and connectivity density.

Table 4-4: Stepwise regression coefficients and regression statistics. The dependent variables were the stiffness (k), energy absorbed (E_A), the specific energy absorbed (W_S), and the impact force (F_{impact}). The independent variables were velar thickness (V.Th), velar spacing (V.Sp), and connectivity density (Conn.D). The p-values for each regression coefficient are shown in italics.

Test	Parameter	V.Th	V.Sp	Conn.D	Regression statistics
Quasi-static	k	76.49	-11.79	-1728	$R^2 = 0.8525$, $p < 0.001$
		< 0.001	*< 0.001*	*0.012*	
	E_A	1.24	-0.19	-37.70	$R^2 = 0.8380$, $p < 0.001$
		< 0.001	*< 0.001*	*< 0.001*	
	W_S	105.3	-15.24	-1915	$R^2 = 0.8652$, $p < 0.001$
		< 0.001	< 0.001	0.045	
Impact	F_{impact}	214.7	98.99	- - -	$R^2 = 0.9701$, $p < 0.001$
		< 0.001	*< 0.001*	- - -	
	E_A =	1.32	0.18	24.26	$R^2 = 0.9907$, $p < 0.001$
		< 0.001	< 0.001	0.004	
	W_S	26.20	48.80	7644	$R^2 = 0.9643$, $p < 0.001$
		0.065	< 0.001	< 0.001	

4.3 Discussion

The mechanical performance of velar bone mimics was investigated to determine candidacy as a novel running midsole architecture. Previous studies of bighorn sheep have established that velar architecture stores energy during quasi-static [129] and impact [130] loading. However, there have not been any previous attempts to mimic this structure as has been done for other natural impact resistant and energy-absorbing materials such as nacre [135]–[141], mantis shrimp dactyl club [142], [143], woodpecker skull [144], conch shell [145], and beetle shell [146]. Our results show that velar architecture exhibits similar bone volume fraction, larger velar thickness and spacing, and lower velar number and connectivity density compared to the analogous architectural indices in human and sheep trabecular bone. This knowledge was used to design a novel biomimetic architecture that was mechanically tested and compared to EVA running shoe midsole foams. Through an iterative design process, we developed velar bone mimics which had greater stiffness and higher energy absorption during quasi-static compression than the EVA foams. Additionally, our results show that velar bone mimics can provide higher energy storage and comparable impact forces to the EVA foams during impact. These results support the hypothesis that velar architecture has the potential to improve the performance of athletic footwear.

One limitation of this study is the difference in geometry between the EVA foams and the velar bone mimics. Velar bone mimics are an open-cell foam whereas the EVA foams are closed-cell. Trapped air has been shown to increase stiffness in closed-cell foams. However, our study is valuable because our results indicate that, despite the difference in geometry, velar bone mimics show comparable stiffness, improved energy absorption in quasi-static compression and lowered impact forces during impact. Another limitation of this study is visual isolation of the second-generation VBMs. This method was used since Abaqus does not provide utility to physically crop sections from the mesh for mimic preparation. Despite this limitation, the second-generation

VBMs showed improved stiffness and energy storage over the first-generation VBMs. A final limitation of our study is knowledge of the herd dominance of each sheep. VBM1 and VBM1-2G samples experienced less impact force than the other mimics in their respective generation of velar bone mimics. The lower impact force indicates that this sheep may have been able to ram harder than other sheep thus implying dominance. If the sheep were the dominant male this could explain why VBM1 outperformed the other mimics. Nevertheless, our results show that velar architecture possess intrinsic energy storage capabilities.

Velar bone mimics were shown to be stiffer and absorb more energy during quasi-static compression than the EVA foams. Furthermore, the stiffness of most velar bone mimics were within the range of previously measured midsole stiffnesses (30-429 N/mm [171], [176]–[178]). These values include previous studies that tested midsoles from different manufacturers, different test geometries (whole shoe or midsole section), different materials (PU, EVA, or EPS), and with different mechanical testing procedures (displacement versus load-controlled compression). For energy absorption, our results are in the range of previously published values for energy absorption of midsole foams during quasi-static compression (960-1,680 mJ) [171]. However, specific energy absorption of the velar bone mimics is significantly lower than that of the EVA foams. These differences can be attributed to a variety of factors such as material density or intrinsic energy absorption of the material, but it seems the primary factor in this case is material architecture. The velar bone mimics are an open cell foam and the EVA foams are closed cell. It has been shown that elastic compression of trapped air within the foam cells contributes to ~22% of the stiffness and ~28% of the energy absorbed at 25% strain during compression [194]. Velar bone mimics were shown be stiffer than EVA foams but experience comparable impact forces. Impact forces ranged from 446-820N for the EVA foams and 499-1145N for the velar bone mimics. However,

these impact forces are on the low end of a previously reported range between 992 and 1,500N found in a study that followed the same testing procedures on different midsoles foams [176]. Additionally, velar bone mimics were shown experience less displacement during impact, which implies greater stiffness during impact and increased runner comfort. Furthermore, energy absorption shown for the velar bone mimics was within the range of published values for similar impact tests (2.2-3.0J) [176]. However, specific energy absorption was significantly higher in the EVA foams than in velar bone mimics. Like quasi-static compression, these differences are likely attributed to the differences in material architectures (closed-cell vs. open-cell structures) and may be improved upon through further design iteration.

Peak impact force during running is intrinsically linked to midsole stiffness [177], [195]. Contradicting studies have shown negative [196], no [197], [198], and positive [177], [199] correlation between midsole stiffness and impact force. Our data demonstrated impact force was negatively correlated with stiffness below ~ 60 N/mm and positively correlated with stiffness above ~80 N/mm that is explained by a quadratic relationship. This implies that impact force can by minimized by optimizing stiffness. However, care must be taken in interpreting the quadratic regression from our data since it encompasses different architectures from velar bone mimics unique to each horn. Nevertheless, our data indicate that a complex relationship between impact force and stiffness exists. This relationship is further complicated by results from the stepwise regressions. Strong dependence was found between impact force, energy storage, and velar architecture. Decreased impact force is achieved by increasing velar spacing and decreasing velar thickness, while increased energy absorption is achieved by increasing velar thickness and decreasing velar spacing. These contradictions suggest that velar bone adaptions are the result of a complex optimization process and that there are other aspects of the velar architecture that likely

play a role in impact force reduction and energy storage. For example, length, width, and curvature of velae have not yet been quantified and no automated procedure exists to quantify these parameters. Changes in velar length, thickness, and curvature would surely affect the mechanical response of the structure. Regardless, our data show that iterative design of velar bone mimics can reduce impact forces. Therefore, it is concluded that velar architecture is adapted for impact and mimicking this architecture may lead to novel structure designs for impact applications. However, desired results of reduced impact force and increased energy storage were not yet achieved for all velar bone mimics developed in this study. Despite this, we show that the second-generation VBMs have improved performance over first-gen VBMs, thereby indicating potential success of our iterative design process to guide the design of novel midsole structures. Broadly speaking, our findings have implications for the design of biomimetic material architectures with optimized parameters for impact force minimization. In the future, similar methodology can be used to guide further development of bighorn sheep velar bone bioinspired energy absorbing material architectures for other applications such has helmets, packing, and vehicle panels.

4.4 Conclusions

- Velar architecture is adapted for impact loading.
- Velar bone mimics are can reduce impact forces and displacements while maintaining stiffness to support body weight during standing and therefore are suitable for midsole architecture replacement.
- Impact force and midsole stiffness are quadratically related.

Chapter 5: Future Work

5.1 Velar bone mimics

5.1.1 ***Material choice***

One of the limitations of this study is that one material was used to create these architectures. A material with elastic modulus less than that of EVA (48 MPa) and greater than that of EPU 40 (~6.94 MPa) will have different performance and likely show better impact performance, likely a reduction in maximum impact force and an increase in impact energy absorption. This conclusion is made based on the material index for impact energy absorption on page 72 of [17].

5.1.2 ***Material enhancement***

Using shear lag analysis [200] to analyze potential fiber reinforcement it may be possible to reinforce EPU 40 with a reinforcing fiber. This method can be used to evaluate fibers that are introduced to matrix and are intended to act as reinforcement. In the mathematical analysis below (Figure 5-1) $E_{material}$ is the elastic modulus of the reinforced, $\nu_{material}$ is the Poissons ratio of the reinforced material, $G_{material}$ is the Shear Modulus of the reinforced material, l_{fiber} is the reinforcement fiber length, d_{fiber} is the reinforcement fiber diameter, A_{fiber} is the cross-sectional area of the reinforcement fiber, E_{fiber} is the elastic modulus of the reinforcement fiber, $\sigma_{ultimate\_fiber}$ is the ultimate strength of the reinforcement fiber, R_{matrix} is the radius of the matrix of material surrounding the reinforcement fiber, in this case the thickness of an singular velae, and $\sigma_{ultimate\_matrix}$ is the ultimate strength of the reinforced material. These values are used in the shear lag equations

presented in [200]. In the shear lag equations β is the load transfer parameter, τ_i is the shear stress transferred to the fiber from the matrix, and l_c is the critical length of the fiber.

Mathematical Approach

Known values

$E_{material} := 6.24MPa \qquad \nu_{material} := 0.48$

Assumed values (for computation check)

$l_{fiber} := 5mm \qquad d_{fiber} := 0.5mm \qquad A_{fiber} := \frac{\pi}{4} \cdot d_{fiber}^{2} \qquad E_{fiber} := 2MPa \qquad R_{matrix} := 0.5mm$

$\sigma_{ultimate\_matrix} := 12.755MPa \qquad \sigma_{ultimate\_fiber} := 2MPa$

Calculations:

$$G_{material} := \frac{E_{material}}{1 + \nu_{material}} \qquad \beta := \sqrt{\frac{2 \cdot \pi \cdot G_{material}}{E_{fiber} \cdot A_{fiber} \cdot \ln\left(\frac{R_{matrix}}{d_{fiber} \cdot 0.5}\right)}} = 9.002 \times 10^{3} \frac{1}{m}$$

$$\tau_i := \frac{\frac{d_{fiber}}{2} \cdot \sigma_{ultimate\_matrix} \cdot \beta}{2} \cdot \frac{\sinh\left[\beta \cdot \left(\frac{l_{fiber}}{2}\right)\right]}{\cosh\left[\beta \cdot \left(\frac{l_{fiber}}{2}\right)\right]} = 14.352 \cdot MPa$$

$$l_c := \frac{\sigma_{ultimate\_fiber}}{2 \cdot \tau_i} \cdot d_{fiber} = 0.035 \cdot mm$$

Figure 5-1: Shear lag analysis for improving the strength of velar bone mimics printed from EPU40.

Interpretation of these results is as follows: if the computed critical length is less than or equal to the length of the fiber you are reinforcing with, the fiber will act as a reinforcement. From manipulation of these equations one can conclude 1) Increasing the elastic modulus of the matrix decreases the critical length of the fiber, 2) increasing the elastic modulus of the fiber increases the critical length of the fiber, 3) increasing the ultimate strength of the fiber increases the critical length of the fiber, and 4) increasing the fiber diameter increases the critical length of the fiber. If it is necessary to design the elastic modulus of the fiber composite to be equivalent to the elastic modulus another material it is imperative to combine the above considerations with the

considerations shown in Figure 5-2. In this analysis the elastic modulus of the fiber reinforced composite material is set equal to the elastic modulus of EVA, a common running shoe midsole material, and then used to compute the fiber volume fraction necessary to achieve this equivalence of the elastic moduli. The mechanics of cellular solids equations [17] are used to compute the elastic modulus of EVA from the measured apparent elastic modulus. The Rule of Mixtures [200] calculations are used to compute the necessary fiber volume fraction. In the equations below $E_{apparent\_shoe}$ is the apparent elastic modulus measured from the running shoe midsole samples of this study (30 MPa), $\rho_{fractional\_shoe}$ is the volume fraction of material in the shoe (70%), E_{actual_shoe} is the computed material elastic modulus using the mechanics of cellular solids equations, E_{fiber} is the elastic modulus of the reinforcement fiber and for examples purposes is assumed to be 2 MPa, and E_{matrix} is the elastic modulus of the reinforced material (EPU 40, 6.94 MPa).

Calculations

from Gibson

$$\frac{E_{apparent\_shoe}}{E_{actual\_shoe}} = C_1 \cdot \left(\frac{\rho_{apparent\_shoe}}{\rho_{actual\_shoe}}\right)^2 = C_1 \cdot \left(\rho_{fractional\_shoe}\right)^2 \qquad C_1 := 1$$

$$\frac{E_{apparent\_shoe}}{E_{actual\_shoe}} = C_1 \cdot \left(\rho_{fractional\_shoe}\right)^2$$

$$E_{actual\_shoe} := \frac{E_{apparent\_shoe}}{C_1 \cdot \rho_{fractional\_shoe}^2} = 61.224 \cdot MPa$$

from Chawla

$$E_{composite} = f \cdot E_{fiber} + (1 - f) \cdot E_{matrix} = E_{actual\_shoe}$$

$$f := \frac{E_{actual\_shoe} - E_{fiber}}{E_{fiber} - E_{matrix}} = 0.261$$

Figure 5-2: Rule of mixture calculations to achieve equal elastic moduli between EVA and EPU40 using a reinforcement fiber.

From these calculations in is seen that a fiber volume fraction of ~26% is necessary to increase the elastic modulus of EPU40 to that of EVA. However, using fiber reinforcement is only possible if the matrix material wets the surface of the fiber. Otherwise, functionalization of the fiber surface such that it chemically attaches to the matrix would be necessary.

5.1.3 ***Optimize the angle for directional energy transfer***

Directional energy transfer is relatively new term that has been used to describe the transfer of energy from the input direction to another direction [201]. It has been shown that this can be optimized for energy transfer in the direction of running thus assist with athlete performance [187], [202]. This study found that my rotating the tubes by 18 degrees (Figure 5-3) that the energy stored during compression would help propel the runner forward when released.

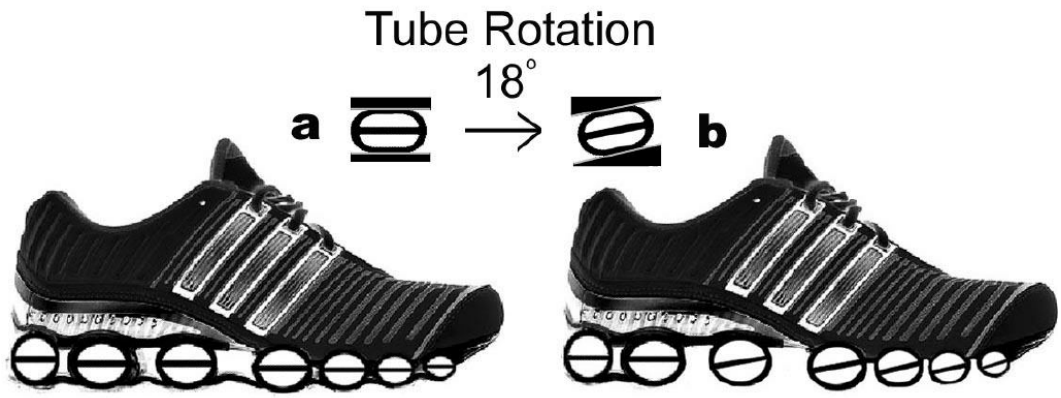

Figure 5-3: (a) Adidas bounce shoe and (b) Adidas bounce shoe with energy transfer optimized and maximize. Image adapted from [202]

A similar concept may apply to the velar bone mimics by rotating the cropped section such that the velar bone mimic experiences similar loading as to what is depicted in Figure 5-3. However, directional energy transfer control may be something that is more appropriately suited for regular geometries as presented in [187], [202].

5.1.4 ***Closed cell structure***

Polymeric foams are typically made through traditional foaming techniques where a physical or chemical blowing agent creates gas pockets that produce a random architecture [173]. Therefore, mechanical behavior can be described by two at least two unique components: a recoverable nonlinear elastic component due to the air compression and a non-recoverable ideal cushion due to the plastic and/or elastic collapse of the foam [194]. A potential method to create closed cell velar bone mimics is a 2-part manufacturing process: 1) 3D print these mimics from EPU40 (or stiffer material as mentioned in 5.1.1) with a 2mm thick side wall on the bottom, left, right, front, and back of the mimic and 2) 3D print a 2 mm wall and then adhere to the top of the mimic with acetone, an adhesive, or a vulcanizing agent to create the closed structure (Figure 5-4). If an airtight seal is created when adhering the top surface to the mimic the effects of the elastic air compression would be observed. One thing to consider here is that if produced using a Carbon Speedcell™ high suction forces are generated during printing and would cause warping of the box walls if the box is printed separately. Printing the box and the mimic simultaneously could solve any warping issues, assuming there is proper venting for uncured resin to flow out of the printed architecture.

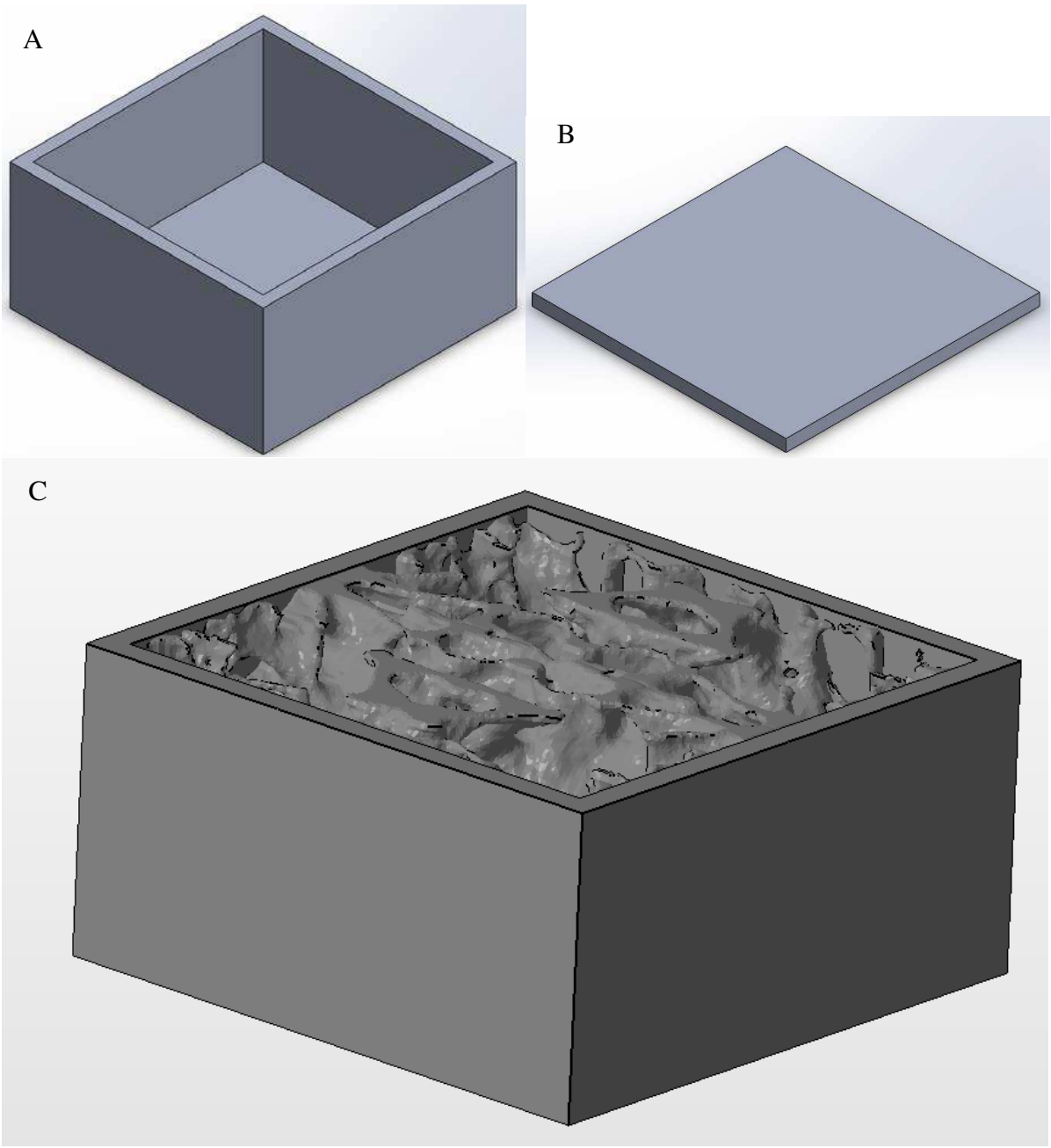

Figure 5-4 A) 44x44x22mm box with 2mm wall thickness, B) 44x44x2mm plate, and C) VBM1 inserted into the cutout of the box shown in A)

5.1.5 ***Topology optimization***

Topology optimization is a method for optimizing material location within a given design problem subject to a given set of constraints with the goal of optimizing strength, toughness, etc. while minimizing the amount of material used. Shown in Figure 5-5 [203] is an example of topology optimization performed on a cube in that is being compressed.

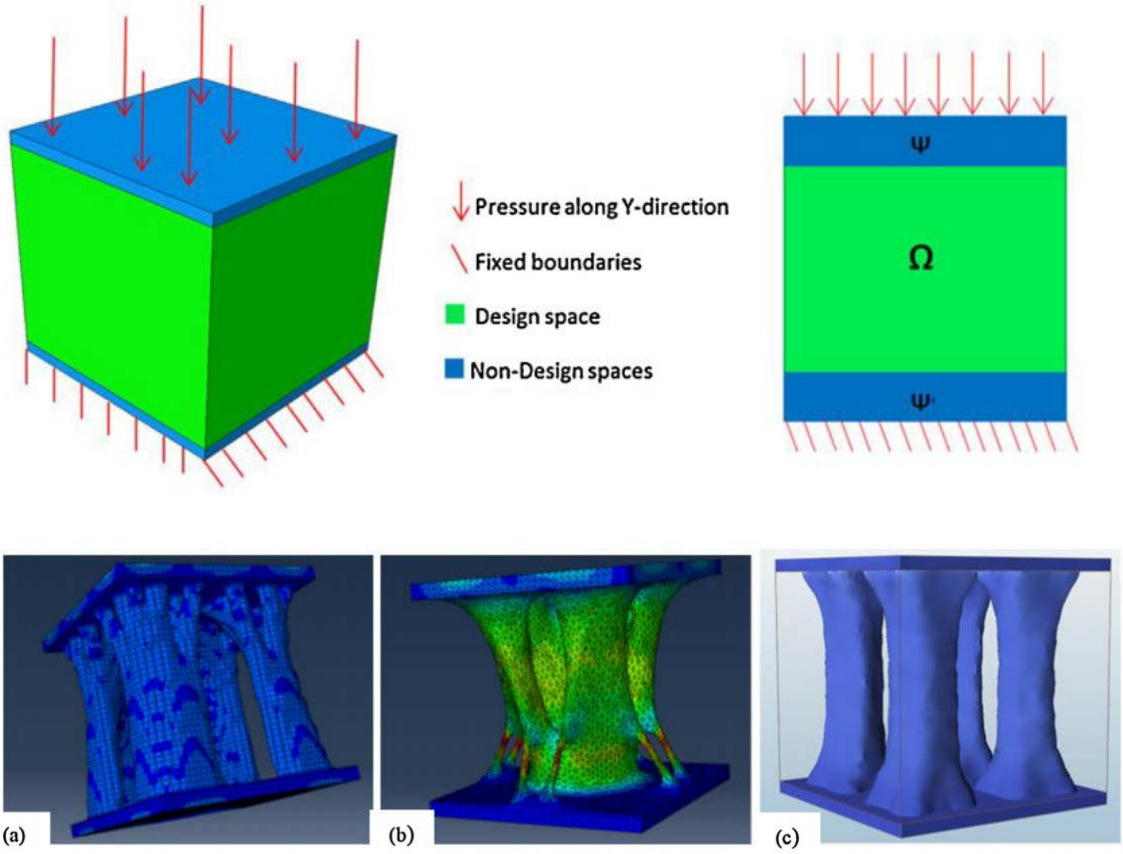

Figure 5-5: (Top) design space and constraints. Optimized structure from (a) Abaqus discrete compliance optimization, (b) and Abaqus stress-constrained optimization, and (c) Optistruct continuous compliance optimization. Image adapted from [203]

From Figure 5-5 the material within the design space was minimized three different ways subject to the three different constraints. This method maybe be able to improve on this work by optimizing the topology of the velar bone mimics.

5.1.6 ***Improved iterative design process***

The velar bone mimics of this study were modeled as linear elastic. A different constitutive model such as hyperelastic, hypoelastic, hyperfoam, or viscoelastic will show different behavior that the models of this study and possibly model behavior of the velar bone mimics in a more accurately. By utilizing a better constitutive model combined with impact finite element models the iterative design process could be improved upon.

5.1.7 ***Novel additive manufacturing technologies***

When the bulk of this work was performed the primary option for additive manufacturing of elastomeric velar bone mimics was using a Carbon Speedcell™. Additive manufacturing is a rapidly growing and changing industry, therefore as new technology is developed there may be more efficacious methods for additive manufacture of these structures. A potential option would be collaboration with Dr. Brett Compton[3] at the University of Tennessee-Knoxville in the Mechanical, Aerospace, and Biomedical Engineering Department. Dr. Compton is developing direct-write technology that is capable of printing closed cell elastomeric foams that cure in ambient conditions, i.e. oven or UV curing is not necessary. As the technology further develops and elastomeric printers with higher resolution are developed velar bone mimics can be made with more unit cells by isotropically scaling each unit cell to smaller size.

[3] https://mabe.utk.edu/people/brett-g-compton/

5.1.8 ***Shape memory alloys***

The shape memory effect is shown in materials whose crystallography allows for a thermo-elastic martensitic transformation [204], [205]. These materials exhibit not only superelasticity but recoverable plastic strains up to 10% and sometimes higher [206]. Shape memory alloys, such as Cu-Al-Ni or NiTi, show deformation recoverability when heated above the critical temperature where the material transforms back to its austenitic phase [207]. It has been shown that his heat can be generated through Joule (resistive) heating [208], [209]. Nickel-titanium foams have been shown to exhibit brittle behavior during compression testing [210], [211]. However, these foams were manufactured using spark plasma sintering (SPS). Since it is not well understood what effect the electric magnetic fields have on sintered samples it is possible that this influenced the integrity of the tested samples. Considering the complex geometry of the foams of this study SPS is not a suitable manufacturing method to create velar bone mimics. Therefore, it is suggested that a selective laser sintering process is used to consolidate shape memory alloy powders to create velar bone mimic specimen. It has been shown that selective laser sintering and selective laser melting are suitable methods for creating NiTi foams [212]–[214]

5.1.9 ***Impact force versus stiffness***

The data presented in the velar bone mimic study show that stiffness and impact force are quadratically related. By performing the same impact test on a foam that has been carefully designed such that the stiffness can be controlled would provide more insight into the relationship between stiffness and impact force (i.e. provided more resolution between 50 and 80 N/mm). This potential study could be used to optimize cushioning structures for athletic shoes, helmets, and shipping/packaging materials.

5.1.10 ***Midsole design approach 1***

One potential route for midsole design is shown in Figure 5-6. With knowledge of the runner's plantar pressure map, one could combine first- and second-generation velar bone mimics in parallel and/or series to achieve 70 N/mm stiffness to minimize impact force (494 N). This new structure could then be placed in high pressure regions with mimics around the periphery of the sole to provide support to the runner. For example, VBM5-1G in parallel with the series combination of 2x VBM3-2G in parallel and 2x VBM4-2G parallel has an effective stiffness of 70.64 N. An example calculation is shown in Figure 5-7.

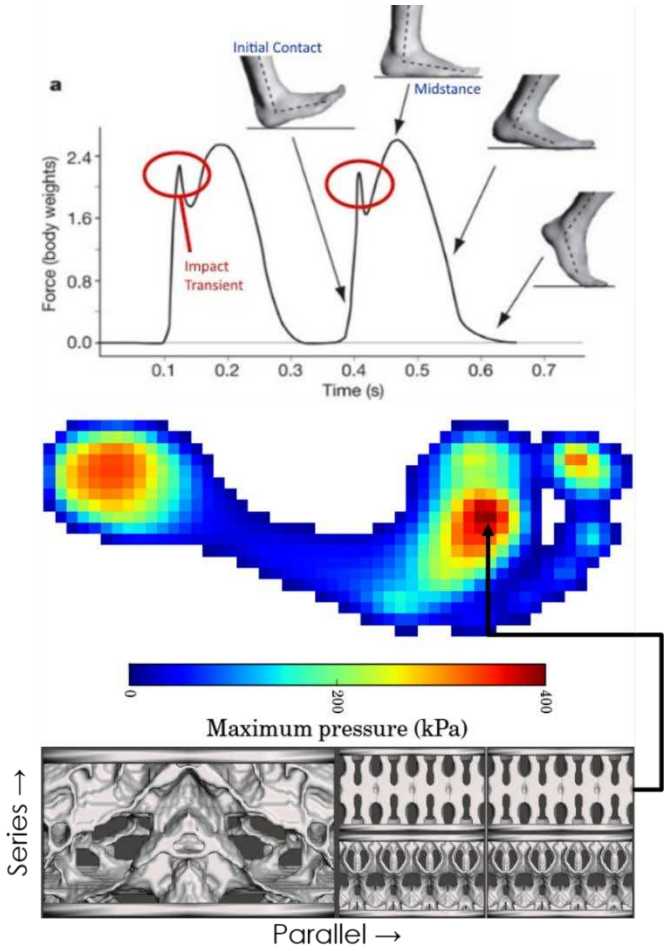

Figure 5-6: Potential shoe sole design approach 1. Image adapted from [215], [216]

$$k_{effective} := k_{VBM5\_1G} + \left(\frac{1}{k_{VBM4\_2G} + k_{VBM4\_2G}} + \frac{1}{k_{VBM3\_2G} + k_{VBM3\_2G}} \right)^{-1} = 70.642 \frac{N}{mm}$$

Figure 5-7: Example equivalent stiffness calculation

5.1.11 ***Midsole design approach 2***

A second potential route for midsole design is shown in Figure 5-8. In this approach, knowledge of the runner's plantar pressure map, one could combine VBM-1G and VBM-2G unit cells to provide the appropriate stiffness where it is needed. That is, the stiffest unit cell in high pressure regions and lowest stiffness unit cell in the area with the lowest pressure. This would create a sort of stepwise functionally graded midsole.

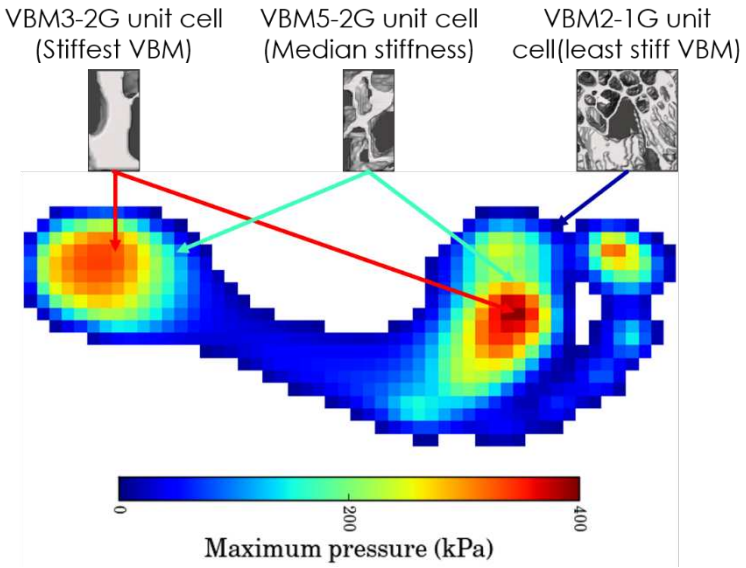

Figure 5-8: Potential shoe sole design approach 2. Image adapted from [216]

5.1.12 ***Midsole design approach 3***

Use the methods demonstrated in 5.1.10 to create a midsole with homogenous optimized stiffness.

5.2 Velar architecture in other species of bighorn sheep

Ovis canadensis canadensis is only one subspecies of one species of bighorn sheep. Table 5-1 lists additional bighorn sheep species and subspecies. It would be interesting to study the velar architecture in other species of bighorn sheep to determine differences/similarities in the velar architecture. It may be possible to find skulls of these animals at universities and museums in the respective regions.

Table 5-1: Species, subspecies, and region of various bighorn sheep

Species	Subspecies	Common Name	Region
Ovis canadensis	*O. c. sierrae*	Sierra Nevada bighorn sheep	California, North Dakota, BC Canada
	O. c. nelsoni	Nelson's bighorn sheep	California, Arizona
	O. c. mexicana	Mexican bighorn sheep	New Mexico, Chihuahua Mexico
	O. c. cremnobates	Peninsular bighorn sheep	Baja California Mexico
	O. c. weemsi	Weems' bighorn sheep	Baja California Mexico
Ovis dalli	*O. d. dalli*	Dall sheep	Alaska, Canada
	O. d. stonei	Stone Sheep	Alaska, Canada
Ovis nivicola	*O. n. koriakorum*	Koryak snow sheep	Kamchatka peninsula Russia
	O. n. ssp.	Kolyma snow sheep	Kolyma Mountains Russia
	O. n. alleni	Okhotsk snow sheep	Khabarovsk region Siberia
	O. n. lydekkeri	Yakutian snow sheep	Magadan region Russia
	O. n. nivicola	Kamchatkan snow sheep	Kamchatka peninsula Russia
	O. n. borealis	Putorana snow sheep	Taimyr Peninsula Russia
	O. n. tschuktschorum	Chukotka snow sheep	Chukotka Autonomous Region Russia

5.3 Strong and lightweight structures

5.3.1 ***Topology optimization***

As previously discussed in 5.1.5, the same principles apply to optimizing the trabecular bone of large mass animals for strong light weight structures.

5.3.2 ***Finite element modeling***

It has been shown that 3D printed trabecular bone shows higher stiffness during off-axis loading in sheep (*Ovis aries*) [217], where on-axis loading refers to loading in direction that physiological loading is experienced. In this study trabecular bone from the talus (ankle bone) were scanned in micro-CT and off-axis volumes of interest were virtually cropped from the images files by rotating the cropping cube (Figure 5-9).

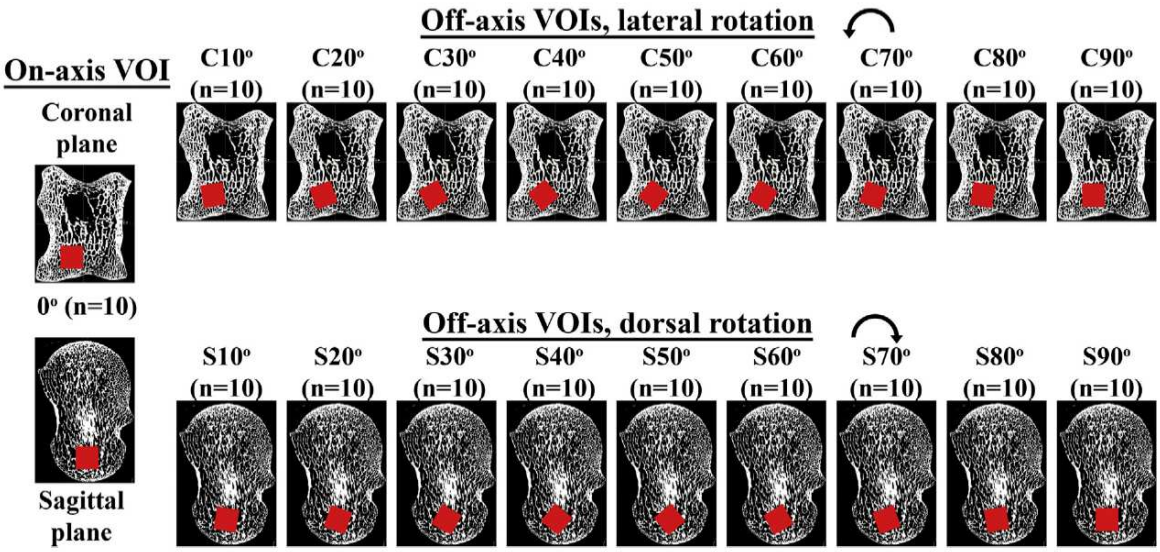

Figure 5-9: Creation of off-axis specimen for 3D printing. Image adapted from [217]

The findings of this study contradicted the author's hypothesis that trabecular bone would have higher stiffness when loaded on-axis as compared to off axis loading. This study investigated only one species. A similar study could be performed by investigating distal femur and proximal tibia trabecular architectures of a wide range of species, including species from this study as well as the trabecular architectures found at [12].

5.4 Allometric studies of the long bones of large mass animals

5.4.1 ***Trabecular bone in the femur/tibia of larger body mass dinosaurs***

This study was limited to animals who weighed up to ~10,000 kg. There are several species of dinosaur who would be candidates for this study. The species, body masses, references, museums, and bones are summarized below in Table 5-2. Other large body mass dinosaur fossils have been discovered but, in some cases, only vertebrae or bones outside the scope of this study have been discovered.

Table 5-2: Femurs and/or tibias of large body mass dinosaurs not included in present study

Dinosaur	Body mass (kg)	References	Museums	Bone
Argentinosaurus hinculensis	81,650	[218]–[220]	Museo Municipal Carmen Funes	Femur (partial)
Patagotitan mayorum	69,850	[221]	Field Museum of Natural History	Femur (whole)
Mamenchisaurus sinocanadorum	68,000	[222]	National Museum of Nature and Science	Skeleton (whole)
Alamosaurus sanjuanensis	66,200	[218], [219], [223]	New Mexico Museum of Natural History & Science	Femur (whole)
Apatosaurus ajax	66,200	[224]	Carnegie Museum of Natural History	Femur (distal)

5.4.2 ***Trabecular bone in other bones of larger body mass dinosaurs***

If further allometric studies similar to [11], [13] are to be performed several large body mass dinosaurs have been summarized in Table 5-3.

Table 5-3: Fossils of other large body mass animals.

Dinosaur	Body mass (kg)	References	Museums	Bone
Natocolossus gonzaleparejasi	68,850	[218]	Universidad Nacional De Cuyo	Humerus (whole)
Sauroposeidon proteles	54,400	[219], [225], [226]	Oklahoma Museum of Natural History	Vertebrae
Dreadnoughtus schrani	53,500	[218], [227]	Museo Padre Molina	Humerus (distal condyle)
Paralititan stromeri	53,500	[219], [228]	Egyptian Geological Museum	Humerus (whole)

In addition to the above various bones or CT scans from different species of dinosaurs of smaller body masses can be possibly obtained by contacting the authors of any of studies cited in this work or journal articles accessed through Wikipedia[4,5]. Additionally, contacting Mr. Bill Wahl[6] at the Wyoming Dinosaur Center, Dr. Laura Vietti[7] in the Geology and Geophysics Department at the University of Wyoming, and/or Dr. Marieka Arksey[8] in the Department of Anthropology at the University of Wyoming could yield additional fossil samples.

[4] https://en.wikipedia.org/wiki/Dinosaur
[5] https://en.wikipedia.org/wiki/Dinosaur_size#Heaviest_sauropodomorphs
[6] https://wyomingdinosaurcenter.org/
[7] http://www.uwyo.edu/geolgeophys/people/faculty/laura-vietti.html
[8] http://www.uwyo.edu/anthropology/directory/m-arskey.html

Works cited

[1] J. D. Currey, "The many adaptations of bone," *Journal of Biomechanics*, vol. 36, no. 10, pp. 1487–1495, Oct. 2003, doi: 10.1016/S0021-9290(03)00124-6.

[2] P. J. Bishop *et al.*, "Cancellous bone and theropod dinosaur locomotion. Part I—an examination of cancellous bone architecture in the hindlimb bones of theropods," *PeerJ*, vol. 6, p. e5778, a2018, doi: 10.7717/peerj.5778.

[3] A. Odgaard, J. Kabel, B. van Rietbergen, M. Dalstra, and R. Huiskes, "Fabric and elastic principal directions of cancellous bone are closely related," *Journal of Biomechanics*, vol. 30, no. 5, pp. 487–495, May 1997, doi: 10.1016/S0021-9290(96)00177-7.

[4] R. Oftadeh, M. Perez-Viloria, J. C. Villa-Camacho, A. Vaziri, and A. Nazarian, "Biomechanics and Mechanobiology of Trabecular Bone: A Review," *Journal of Biomechanical Engineering*, vol. 137, no. 1, p. 010802, Jan. 2015, doi: 10.1115/1.4029176.

[5] D. R. Carter, W. E. Caler, D. M. Spengler, and V. H. Frankel, "Fatigue Behavior of Adult Cortical Bone: The Influence of Mean Strain and Strain Range," *Acta Orthopaedica Scandinavica*, vol. 52, no. 5, pp. 481–490, Jan. 1981, doi: 10.3109/17453678108992136.

[6] B. Martin, "Mathematical model for repair of fatigue damage and stress fracture in osteonal bone," *Journal of Orthopaedic Research*, vol. 13, no. 3, pp. 309–316, May 1995, doi: 10.1002/jor.1100130303.

[7] B. Martin, "Fatigue Damage, Remodeling, and the Minimization of Skeletal Weight," *Journal of Theoretical Biology*, vol. 220, no. 2, pp. 271–276, Jan. 2003, doi: 10.1006/jtbi.2003.3148.

[8] K. J. Motyl, A. R. Guntur, A. L. Carvalho, and C. J. Rosen, "Energy Metabolism of Bone," *Toxicologic Pathology*, vol. 45, no. 7, pp. 887–893, Oct. 2017, doi: 10.1177/0192623317737065.

[9] D. E. Lieberman, "Optimization of bone growth and remodeling in response to loading in tapered mammalian limbs," *Journal of Experimental Biology*, vol. 206, no. 18, pp. 3125–3138, Sep. 2003, doi: 10.1242/jeb.00514.

[10] D. Wu, P. Isaksson, S. J. Ferguson, and C. Persson, "Young's modulus of trabecular bone at the tissue level: A review," *Acta Biomaterialia*, vol. 78, pp. 1–12, Sep. 2018, doi: 10.1016/j.actbio.2018.08.001.

[11] M. Doube, M. M. Klosowski, A. M. Wiktorowicz-Conroy, J. R. Hutchinson, and S. J. Shefelbine, "Trabecular bone scales allometrically in mammals and birds," *Proceedings of the Royal Society B: Biological Sciences*, vol. 278, no. 1721, pp. 3067–3073, Oct. 2011, doi: 10.1098/rspb.2011.0069.

[12] M. Doube, M. M. Kłosowski, J. Hutchinson, and S. J. Shefelbine, "X-ray microtomography images of trabecular bone from the femoral head and condyle of 18 avian, 72 mammalian and one crocodilian species." Oct. 30, 2018, doi: 10.6084/m9.figshare.7257179.v1.

[13] M. M. Barak, D. E. Lieberman, and J.-J. Hublin, "Of mice, rats and men: Trabecular bone architecture in mammals scales to body mass with negative allometry," *Journal of Structural Biology*, vol. 183, no. 2, pp. 123–131, Aug. 2013, doi: 10.1016/j.jsb.2013.04.009.

[14] H. Chen, X. Zhou, H. Fujita, M. Onozuka, and K.-Y. Kubo, "Age-Related Changes in Trabecular and Cortical Bone Microstructure," *International Journal of Endocrinology*, 2013. https://www.hindawi.com/journals/ije/2013/213234/ (accessed Apr. 12, 2019).

[15] H. Chen, X. Zhou, S. Shoumura, S. Emura, and Y. Bunai, "Age- and gender-dependent changes in three-dimensional microstructure of cortical and trabecular bone at the human femoral neck," *Osteoporosis International*, vol. 21, no. 4, pp. 627–636, Apr. 2010, doi: 10.1007/s00198-009-0993-z.

[16] H. Chen, S. Shoumura, S. Emura, and Y. Bunai, "Regional variations of vertebral trabecular bone microstructure with age and gender," *Osteoporosis International*, vol. 19, no. 10, pp. 1473–1483, Oct. 2008, doi: 10.1007/s00198-008-0593-3.

[17] L. J. Gibson, M. F. Ashby, and B. A. Harley, *Cellular Materials in Nature and Medicine*. Cambridge University Press, 2010.

[18] Li. Mosekilde, "Age-related changes in vertebral trabecular bone architecture—assessed by a new method," *Bone*, vol. 9, no. 4, pp. 247–250, 1988, doi: 10.1016/8756-3282(88)90038-5.

[19] A. M. Parfitt, C. H. Mathews, A. R. Villanueva, M. Kleerekoper, B. Frame, and D. S. Rao, "Relationships between surface, volume, and thickness of iliac trabecular bone in aging and in osteoporosis. Implications for the microanatomic and cellular mechanisms of bone loss.," Oct. 01, 1983. https://www.jci.org/articles/view/111096/pdf (accessed Apr. 12, 2019).

[20] M. J. Silva and L. J. Gibson, "Modeling the mechanical behavior of vertebral trabecular bone: Effects of age-related changes in microstructure," *Bone*, vol. 21, no. 2, pp. 191–199, Aug. 1997, doi: 10.1016/S8756-3282(97)00100-2.

[21] J. W. Pugh, R. M. Rose, and E. L. Radin, "Elastic and viscoelastic properties of trabecular bone: Dependence on structure," *Journal of Biomechanics*, vol. 6, no. 5, pp. 475–485, Sep. 1973, doi: 10.1016/0021-9290(73)90006-7.

[22] T. R. Chandrupatla and A. D. Belegundu, *Introduction to Finite Elements in Engineering*, 3rd ed. Upper Saddle River, New Jersey: Prentice - Hall, 2002.

[23] A. A. Alghamdi and H. A. Alharthi, "Multiscale 3D finite-element modelling of the thermal conductivity of clay brick walls," *Construction and Building Materials*, vol. 157, pp. 1–9, Dec. 2017, doi: 10.1016/j.conbuildmat.2017.09.081.

[24] J. Zhu and W. Rodi, "Zonal finite-volume computations of incompressible flows," *Computers & Fluids*, vol. 20, no. 4, pp. 411–420, Jan. 1991, doi: 10.1016/0045-7930(91)90082-S.

[25] S. Klinkel and R. Reichel, "A finite element formulation in boundary representation for the analysis of nonlinear problems in solid mechanics," *Computer Methods in Applied Mechanics and Engineering*, vol. 347, pp. 295–315, Apr. 2019, doi: 10.1016/j.cma.2018.12.020.

[26] H. H. Bayraktar, E. F. Morgan, G. L. Niebur, G. E. Morris, E. K. Wong, and T. M. Keaveny, "Comparison of the elastic and yield properties of human femoral trabecular and cortical bone tissue," *Journal of Biomechanics*, vol. 37, no. 1, pp. 27–35, Jan. 2004, doi: 10.1016/S0021-9290(03)00257-4.

[27] S. K. Eswaran, A. Gupta, M. F. Adams, and T. M. Keaveny, "Cortical and trabecular load sharing in the human vertebral body," *J. Bone Miner. Res.*, vol. 21, no. 2, pp. 307–314, Feb. 2006, doi: 10.1359/jbmr.2006.21.2.307.

[28] M. G. Goff, F. M. Lambers, R. M. Sorna, T. M. Keaveny, and C. J. Hernandez, "Finite element models predict the location of microdamage in cancellous bone following uniaxial loading," *Journal of Biomechanics*, vol. 48, no. 15, pp. 4142–4148, Nov. 2015, doi: 10.1016/j.jbiomech.2015.10.023.

[29] S. Nawathe, B. P. Nguyen, N. Barzanian, H. Akhlaghpour, M. L. Bouxsein, and T. M. Keaveny, "Cortical and trabecular load sharing in the human femoral neck," *Journal of Biomechanics*, vol. 48, no. 5, pp. 816–822, Mar. 2015, doi: 10.1016/j.jbiomech.2014.12.022.
[30] G. L. Niebur, J. C. Yuen, A. C. Hsia, and T. M. Keaveny, "Convergence Behavior of High-Resolution Finite Element Models of Trabecular Bone," *Journal of Biomechanical Engineering*, vol. 121, no. 6, p. 629, 1999, doi: 10.1115/1.2800865.
[31] J. Wang *et al.*, "Trabecular plates and rods determine elastic modulus and yield strength of human trabecular bone," *Bone*, vol. 72, pp. 71–80, Mar. 2015, doi: 10.1016/j.bone.2014.11.006.
[32] M. A. Meyers and K. K. Chawla, *Mechanical Behavior of Materials*. Upper Saddle River, New Jersey: Prentice - Hall, 1999.
[33] J. H. Keyak and S. A. Rossi, "Prediction of femoral fracture load using finite element models: an examination of stress- and strain-based failure theories," *Journal of Biomechanics*, p. 6, 2000.
[34] T. M. Keaveny, E. F. Wachtel, C. M. Ford, and W. C. Hayes, "Differences between the tensile and compressive strengths of bovine tibial trabecular bone depend on modulus," *Journal of Biomechanics*, vol. 27, no. 9, pp. 1137–1146, Sep. 1994, doi: 10.1016/0021-9290(94)90054-X.
[35] E. F. Morgan and T. M. Keaveny, "Dependence of yield strain of human trabecular bone on anatomic site," *Journal of Biomechanics*, vol. 34, no. 5, pp. 569–577, May 2001, doi: 10.1016/S0021-9290(01)00011-2.
[36] S. W. Tsai and E. M. Wu, "A General Theory of Strength for Anisotropic Materials," p. 23, 1970.
[37] S. C. Cowin, "Fabric dependence of an anisotropic strength criterion," *Mechanics of Materials*, vol. 5, no. 3, pp. 251–260, Sep. 1986, doi: 10.1016/0167-6636(86)90022-0.
[38] T. M. Keaveny, E. F. Wachtel, S. P. Zadesky, and Y. P. Arramon, "Application of the Tsai–Wu Quadratic Multiaxial Failure Criterion to Bovine Trabecular Bone," *J Biomech Eng*, vol. 121, no. 1, pp. 99–107, Feb. 1999, doi: 10.1115/1.2798051.
[39] G. L. Niebur, M. J. Feldstein, and T. M. Keaveny, "Biaxial Failure Behavior of Bovine Tibial Trabecular Bone," *Journal of Biomechanical Engineering*, vol. 124, no. 6, p. 699, 2002, doi: 10.1115/1.1517566.
[40] L. J. Gibson, M. F. Ashby, J. Zhang, and T. C. Triantafillou, "Failure surfaces for cellular materials under multiaxial loads—I.Modelling," *International Journal of Mechanical Sciences*, vol. 31, no. 9, pp. 635–663, Jan. 1989, doi: 10.1016/S0020-7403(89)80001-3.
[41] V. Pettarin, L. A. Fasce, and P. M. Frontini, "Assessment of Multiaxial Mechanical Response of Rigid Polyurethane Foams," *Journal of Materials Engineering and Performance*, vol. 23, no. 2, pp. 477–485, Feb. 2014, doi: 10.1007/s11665-013-0542-y.
[42] T. C. Triantafillou and L. J. Gibson, "Multiaxial failure criteria for brittle foams," *International Journal of Mechanical Sciences*, vol. 32, no. 6, pp. 479–496, Jan. 1990, doi: 10.1016/0020-7403(90)90154-B.
[43] H. H. Bayraktar, "The Modified Super-Ellipsoid Yield Criterion for Human Trabecular Bone," *Journal of Biomechanical Engineering*, vol. 126, no. 6, p. 677, Dec. 2004, doi: 10.1115/1.1763177.
[44] D. A. Eberth and D. C. Evans, *Hadrosaurs*. Indiana University Press, 2014.

[45] D. M. Lovelace, S. A. Hartman, and W. R. Wahl, “Morphology of a specimen of supersaurus (dinosauria sauropoda) from the Morrison Formation of Wyoming and a re-revaluation of diplodocid phylogeny,” *Arquivos do Museu Nacional, Rio de Janeiro*, vol. 65, no. 4, pp. 527–544, Nov. 2007.
[46] M. J. Benton, *Prehistoric Life.* Edinburgh, Scotland: Dorling Kindersley, 2012.
[47] J. Foster, *Jurassic West: The Dinosaurs of the Morrison Formation and Their World*. Indiana University Press, 2007.
[48] F. Seebacher, “A new method to calculate allometric length-mass relationships of dinosaurs,” *Journal of Vertebrate Paleontology*, vol. 21, no. 1, pp. 51–60, Mar. 2001, doi: 10.1671/0272-4634(2001)021[0051:ANMTCA]2.0.CO;2.
[49] R. T. Bakker and P. M. Galton, “Dinosaur Monophyly and a New Class of Vertebrates,” *Nature*, vol. 248, no. 5444, p. 168, Mar. 1974, doi: 10.1038/248168a0.
[50] P. R. Bell and E. Snively, “Polar dinosaurs on parade: a review of dinosaur migration,” *Alcheringa: An Australasian Journal of Palaeontology*, vol. 32, no. 3, pp. 271–284, Sep. 2008, doi: 10.1080/03115510802096101.
[51] M. T. Carrano, “Homoplasy and the evolution of dinosaur locomotion,” *Paleobiology*, vol. 26, no. 3, pp. 489–512, Sep. 2000, doi: 10.1666/0094-8373(2000)026<0489:HATEOD>2.0.CO;2.
[52] S. M. Gatesy and K. M. Middleton, “Bipedalism, flight, and the evolution of theropod locomotor diversity,” *Journal of Vertebrate Paleontology*, vol. 17, no. 2, pp. 308–329, Jun. 1997, doi: 10.1080/02724634.1997.10010977.
[53] S. Maidment and P. Barrett, “Osteological correlates for quadrupedality in ornithischian dinosaurs,” *Acta Palaeontologica Polonica*, 2012, doi: 10.4202/app.2012.0065.
[54] K. Middleton, “Theropod forelimb design and evolution,” *Zoological Journal of the Linnean Society*, vol. 128, no. 2, pp. 149–187, Jan. 2000, doi: 10.1006/zjls.1998.0193.
[55] F. E. Novas, “Dinosaur monophyly,” *Journal of Vertebrate Paleontology*, vol. 16, no. 4, pp. 723–741, Dec. 1996, doi: 10.1080/02724634.1996.10011361.
[56] H. Pontzer, V. Allen, and J. R. Hutchinson, “Biomechanics of Running Indicates Endothermy in Bipedal Dinosaurs,” *PLoS ONE*, vol. 4, no. 11, p. e7783, Nov. 2009, doi: 10.1371/journal.pone.0007783.
[57] D. A. Thomas and J. O. Farlow, “Tracking a Dinosaur Attack,” *Scientific American*, vol. 277, no. 6, pp. 74–79, Dec. 1997, doi: 10.1038/scientificamerican1297-74.
[58] R. A. Thulborn, “Preferred gaits of bipedal dinosaurs,” *Alcheringa: An Australasian Journal of Palaeontology*, vol. 8, no. 3, pp. 243–252, Jan. 1984, doi: 10.1080/03115518408618947.
[59] L. Maiorino, A. A. Farke, T. Kotsakis, L. Teresi, and P. Piras, “Variation in the shape and mechanical performance of the lower jaws in ceratopsid dinosaurs (Ornithischia, Ceratopsia),” *Journal of Anatomy*, vol. 227, no. 5, pp. 631–646, 2015, doi: 10.1111/joa.12374.
[60] L. Maiorino, A. A. Farke, T. Kotsakis, P. Raia, and P. Piras, “Who is the most stressed? Morphological disparity and mechanical behavior of the feeding apparatus of ceratopsian dinosaurs (Ornithischia, Marginocephalia),” *Cretaceous Research*, vol. 84, pp. 483–500, Apr. 2018, doi: 10.1016/j.cretres.2017.11.012.
[61] J. C. Mallon and J. S. Anderson, “Jaw mechanics and evolutionary paleoecology of the megaherbivorous dinosaurs from the Dinosaur Park Formation (upper Campanian) of Alberta, Canada,” *Journal of Vertebrate Paleontology*, vol. 35, no. 2, p. e904323, Mar. 2015, doi: 10.1080/02724634.2014.904323.

[62] M. Sakamoto, “Jaw biomechanics and the evolution of biting performance in theropod dinosaurs,” *Proceedings of the Royal Society B: Biological Sciences*, vol. 277, no. 1698, pp. 3327–3333, Nov. 2010, doi: 10.1098/rspb.2010.0794.

[63] K. Tanoue, B. S. Grandstaff, H.-L. You, and P. Dodson, “Jaw Mechanics in Basal Ceratopsia (Ornithischia, Dinosauria),” *The Anatomical Record*, vol. 292, no. 9, pp. 1352–1369, 2009, doi: 10.1002/ar.20979.

[64] A. Torices, R. Wilkinson, V. M. Arbour, J. I. Ruiz-Omeñaca, and P. J. Currie, “Puncture-and-Pull Biomechanics in the Teeth of Predatory Coelurosaurian Dinosaurs,” *Current Biology*, vol. 28, no. 9, pp. 1467-1474.e2, May 2018, doi: 10.1016/j.cub.2018.03.042.

[65] U. Witzel and H. Preuschoft, “Finite-element model construction for the virtual synthesis of the skulls in vertebrates: Case study of Diplodocus,” *The Anatomical Record Part A: Discoveries in Molecular, Cellular, and Evolutionary Biology*, vol. 283A, no. 2, pp. 391–401, Apr. 2005, doi: 10.1002/ar.a.20174.

[66] P. J. Bishop, S. A. Hocknull, C. J. Clemente, J. R. Hutchinson, R. S. Barrett, and D. G. Lloyd, “Cancellous bone and theropod dinosaur locomotion. Part II—a new approach to inferring posture and locomotor biomechanics in extinct tetrapod vertebrates,” *PeerJ*, vol. 6, p. e5779, b2018, doi: 10.7717/peerj.5779.

[67] P. J. Bishop *et al.*, “Cancellous bone and theropod dinosaur locomotion. Part III—Inferring posture and locomotor biomechanics in extinct theropods, and its evolution on the line to birds,” *PeerJ*, vol. 6, p. e5777, c2018, doi: 10.7717/peerj.5777.

[68] FI-AeroWeb, “U.S. Commercial Aircraft Fleet 2017 | By Model, Type and Airline,” 2018. http://www.fi-aeroweb.com/US-Commercial-Aircraft-Fleet.html (accessed Apr. 04, 2019).

[69] B. P. Bhatta, “Pay-as-you-weigh pricing of an air ticket,” *Journal of Air Transport Management*, vol. 18, no. 1, pp. 30–33, Jan. 2012, doi: 10.1016/j.jairtraman.2011.07.003.

[70] “NASA - Advanced Space Transportation Program fact sheet,” 2008. https://www.nasa.gov/centers/marshall/news/background/facts/astp.html (accessed Apr. 04, 2019).

[71] T. Dursun and C. Soutis, “Recent developments in advanced aircraft aluminium alloys,” *Materials & Design (1980-2015)*, vol. 56, pp. 862–871, Apr. 2014, doi: 10.1016/j.matdes.2013.12.002.

[72] J. C. Williams and E. A. Starke, “Progress in structural materials for aerospace systems11The Golden Jubilee Issue—Selected topics in Materials Science and Engineering: Past, Present and Future, edited by S. Suresh.,” *Acta Materialia*, vol. 51, no. 19, pp. 5775–5799, Nov. 2003, doi: 10.1016/j.actamat.2003.08.023.

[73] D. A. Necsulescu, “THE EFFECTS OF CORROSION ON THE MECHANICAL PROPERTIES OF ALUMINIUM ALLOY 7075-T6,” *UPD Scientific Bulletin*, vol. 73, no. 1, p. 7, 2011.

[74] X. Zhang, Y. Chen, and J. Hu, “Recent advances in the development of aerospace materials,” *Progress in Aerospace Sciences*, vol. 97, pp. 22–34, Feb. 2018, doi: 10.1016/j.paerosci.2018.01.001.

[75] V. Rahul *et al.*, “Structural health monitoring of aerospace composites,” in *Structural Health Monitoring of Biocomposites, Fibre-Reinforced Composites and Hybrid Composites*, Elsevier, 2019, pp. 33–52.

[76] E. Kappel, “Distortions of composite aerospace frames due to processing, thermal loads and trimming operations and an assessment from an assembly perspective | Elsevier Enhanced

Reader," *Composite Structures*, 2019, doi: https://doi.org/10.1016/j.compstruct.2019.03.099.
[77] "Beyond the Boomers – Institute for Advanced Composites Manufacturing Innovation – IACMI," 2018. https://iacmi.org/2018/09/04/beyond-the-boomers/ (accessed Apr. 05, 2019).
[78] "Is a composites technical talent shortage looming? : CompositesWorld," 2015. https://www.compositesworld.com/articles/is-a-composites-technical-talent-shortage-looming (accessed Apr. 05, 2019).
[79] X. Xu, Q. Tan, C. Sullivan, F. Han, and D. Xiao, "A Short-Armed Troodontid Dinosaur from the Upper Cretaceous of Inner Mongolia and Its Implications for Troodontid Evolution," *PLoS ONE*, vol. 6, no. 9, p. e22916, Sep. 2011, doi: 10.1371/journal.pone.0022916.
[80] Y. Yu *et al.*, "A new caenagnathid dinosaur from the Upper Cretaceous Wangshi Group of Shandong, China, with comments on size variation among oviraptorosaurs," *Scientific Reports*, vol. 8, no. 1, Dec. 2018, doi: 10.1038/s41598-018-23252-2.
[81] S. Lautenschlager, E. J. Rayfield, P. Altangerel, L. E. Zanno, and L. M. Witmer, "The Endocranial Anatomy of Therizinosauria and Its Implications for Sensory and Cognitive Function," *PLoS ONE*, vol. 7, no. 12, p. e52289, Dec. 2012, doi: 10.1371/journal.pone.0052289.
[82] L. E. Zanno and P. J. Makovicky, "No evidence for directional evolution of body mass in herbivorous theropod dinosaurs," *Proceedings of the Royal Society B: Biological Sciences*, vol. 280, no. 1751, pp. 20122526–20122526, Nov. 2012, doi: 10.1098/rspb.2012.2526.
[83] A. Lister and P. Bahn, *Mammoths: Giants of the Ice Age*. University of California Press, 1994.
[84] M. E. McGee, K. W. Magic, D. L. Miller, A. J. Maki, and S. W. Donahue, "Black bear femoral porosity decreases and mechanical properties increase with age despite annual periods of disuse (hibernation)," *Engineering Fracture Mechanics*, vol. 74, no. 12, pp. 1942–1952, Aug. 2007, doi: 10.1016/j.engfracmech.2006.05.010.
[85] A. K. Hunter and W. D. McDavid, "Characterization and correction of cupping effect artefacts in cone beam CT," *Dentomaxillofac Radiol*, vol. 41, no. 3, pp. 217–223, Mar. 2012, doi: 10.1259/dmfr/19015946.
[86] M. Doube *et al.*, "BoneJ: Free and extensible bone image analysis in ImageJ," *Bone*, vol. 47, no. 6, pp. 1076–1079, Dec. 2010, doi: 10.1016/j.bone.2010.08.023.
[87] T. Hildebrand, A. Laib, R. Müller, J. Dequeker, and P. Rüegsegger, "Direct Three-Dimensional Morphometric Analysis of Human Cancellous Bone: Microstructural Data from Spine, Femur, Iliac Crest, and Calcaneus," *Journal of Bone and Mineral Research*, vol. 14, no. 7, pp. 1167–1174, Jul. 1999, doi: 10.1359/jbmr.1999.14.7.1167.
[88] R. B. Martin, D. B. Burr, and N. A. Sharkey, *Skeletal Tissue Mechanics*. Springer Science & Business Media, 1998.
[89] B. B. Wheatley, K. M. Fischenich, K. D. Button, R. C. Haut, and T. L. Haut Donahue, "An optimized transversely isotropic, hyper-poro-viscoelastic finite element model of the meniscus to evaluate mechanical degradation following traumatic loading," *Journal of Biomechanics*, vol. 48, no. 8, pp. 1454–1460, Jun. 2015, doi: 10.1016/j.jbiomech.2015.02.028.

[90] A. Lipphaus and U. Witzel, “Finite element syntheses of callus and bone remodeling: Biomechanical study of fracture healing in long bones,” *The Anatomical Record*, vol. 0, no. ja, Oct. 2018, doi: 10.1002/ar.23893.
[91] D. l. Logan, *A First Course in the Finite Element Method*, 3rd ed. Brooks/Cole, 2002.
[92] A. P. Boresi and R. J. Schmidt, *Advanced mechanics of materials*, 6th ed. New York: John Wiley & Sons, 2003.
[93] M. L. Bucalem and K.-J. Bathe, *The mechanics of solids and structures: hierarchical modeling and the finite element solution*. Heidelberg: Springer, 2011.
[94] R. J. Roark, W. C. Young, and R. G. Budynas, *Roark’s formulas for stress and strain*, 7th ed. New York: McGraw-Hill, 2002.
[95] H. H. Bayraktar and T. M. Keaveny, “Mechanisms of uniformity of yield strains for trabecular bone,” *Journal of Biomechanics*, vol. 37, no. 11, pp. 1671–1678, Nov. 2004, doi: 10.1016/j.jbiomech.2004.02.045.
[96] D. L. Kopperdahl and T. M. Keaveny, “Yield strain behavior of trabecular bone,” *Journal of Biomechanics*, vol. 31, no. 7, pp. 601–608, Jul. 1998, doi: 10.1016/S0021-9290(98)00057-8.
[97] G. C. Packard, “On the use of log-transformation versus nonlinear regression for analyzing biological power laws: Analyzing Biological Power Laws,” *Biol J Linn Soc Lond*, vol. 113, no. 4, pp. 1167–1178, Dec. 2014, doi: 10.1111/bij.12396.
[98] J. G. Skedros *et al.*, “Scaling of Haversian canal surface area to secondary osteon bone volume in ribs and limb bones,” *American Journal of Physical Anthropology*, vol. 151, no. 2, pp. 230–244, 2013, doi: 10.1002/ajpa.22270.
[99] J. H. Kim and I. Choi, “Choosing the Level of Significance: A Decision-theoretic Approach,” *Abacus*, doi: 10.1111/abac.12172.
[100] R. L. Wasserstein and N. A. Lazar, “The ASA Statement on p -Values: Context, Process, and Purpose,” *The American Statistician*, vol. 70, no. 2, pp. 129–133, Apr. 2016, doi: 10.1080/00031305.2016.1154108.
[101] R. L. Wasserstein, A. L. Schirm, and N. A. Lazar, “Moving to a World Beyond ‘p < 0.05,’” *The American Statistician*, vol. 73, no. sup1, pp. 1–19, Mar. 2019, doi: 10.1080/00031305.2019.1583913.
[102] T. Seek W., “Exploration of Unique Porous Bone Materials for Candidacy in Bioinspired Material Design,” Colorado State University, Fort Collins, 2018.
[103] C. T. Rubin, “Skeletal strain and the functional significance of bone architecture,” *Calcif. Tissue Int.*, vol. 36 Suppl 1, pp. S11-18, 1984.
[104] C. T. Rubin and L. E. Lanyon, “Dynamic strain similarity in vertebrates; an alternative to allometric limb bone scaling,” *Journal of Theoretical Biology*, vol. 107, no. 2, pp. 321–327, Mar. 1984, doi: 10.1016/S0022-5193(84)80031-4.
[105] K. L. Lewton, “In vitro bone strain distributions in a sample of primate pelves,” *Journal of Anatomy*, vol. 226, no. 5, pp. 458–477, 2015, doi: 10.1111/joa.12294.
[106] T. Sugiyama, L. B. Meakin, W. J. Browne, G. L. Galea, J. S. Price, and L. E. Lanyon, “Bones’ adaptive response to mechanical loading is essentially linear between the low strains associated with disuse and the high strains associated with the lamellar/woven bone transition,” *Journal of Bone and Mineral Research*, vol. 27, no. 8, pp. 1784–1793, 2012, doi: 10.1002/jbmr.1599.

[107] T. Sugiyama, J. S. Price, and L. E. Lanyon, "Functional adaptation to mechanical loading in both cortical and cancellous bone is controlled locally and is confined to the loaded bones," *Bone*, vol. 46, no. 2, pp. 314–321, Feb. 2010, doi: 10.1016/j.bone.2009.08.054.
[108] F. Gröning, M. Fagan, and P. O'higgins, "Comparing the Distribution of Strains with the Distribution of Bone Tissue in a Human Mandible: A Finite Element Study," *The Anatomical Record*, vol. 296, no. 1, pp. 9–18, 2013, doi: 10.1002/ar.22597.
[109] J. D. Currey, *Bones: Structure and Mechanics*, 2nd. Princeton University Press, 2002.
[110] D. R. Carter and G. S. Beaupre, *Skeletal Function and Form: Mechanobiology of Skeletal Development, Aging, and Regeneration*. Cambridge: Cambridge University Press, 2001.
[111] S. Nagaraja, T. L. Couse, and R. E. Guldberg, "Trabecular bone microdamage and microstructural stresses under uniaxial compression," *Journal of Biomechanics*, vol. 38, no. 4, pp. 707–716, Apr. 2005, doi: 10.1016/j.jbiomech.2004.05.013.
[112] M. Squire, A. Brazin, Y. Keng, and S. Judex, "Baseline bone morphometry and cellular activity modulate the degree of bone loss in the appendicular skeleton during disuse," *Bone*, vol. 42, no. 2, pp. 341–349, Feb. 2008, doi: 10.1016/j.bone.2007.09.052.
[113] G. Boivin and P. J. Meunier, "The Degree of Mineralization of Bone Tissue Measured by Computerized Quantitative Contact Microradiography," *Calcif Tissue Int*, vol. 70, no. 6, pp. 503–511, Jun. 2002, doi: 10.1007/s00223-001-2048-0.
[114] H. Follet, G. Boivin, C. Rumelhart, and P. J. Meunier, "The degree of mineralization is a determinant of bone strength: a study on human calcanei," *Bone*, vol. 34, no. 5, pp. 783–789, May 2004, doi: 10.1016/j.bone.2003.12.012.
[115] H. Fonseca, D. Moreira-Gonçalves, H.-J. A. Coriolano, and J. A. Duarte, "Bone Quality: The Determinants of Bone Strength and Fragility," *Sports Med*, vol. 44, no. 1, pp. 37–53, Jan. 2014, doi: 10.1007/s40279-013-0100-7.
[116] M. Unal, A. Creecy, and J. S. Nyman, "The Role of Matrix Composition in the Mechanical Behavior of Bone," *Curr Osteoporos Rep*, vol. 16, no. 3, pp. 205–215, Jun. 2018, doi: 10.1007/s11914-018-0433-0.
[117] X. Banse, T. J. Sims, and A. J. Bailey, "Mechanical Properties of Adult Vertebral Cancellous Bone: Correlation With Collagen Intermolecular Cross-Links," *Journal of Bone and Mineral Research*, vol. 17, no. 9, pp. 1621–1628, 2002, doi: 10.1359/jbmr.2002.17.9.1621.
[118] A. J. Bailey, T. J. Sims, E. N. Ebbesen, J. P. Mansell, J. S. Thomsen, and Li. Mosekilde, "Age-Related Changes in the Biochemical Properties of Human Cancellous Bone Collagen: Relationship to Bone Strength," *Calcified Tissue International*, vol. 65, no. 3, pp. 203–210, Sep. 1999, doi: 10.1007/s002239900683.
[119] A. Boskey, "Bone mineral crystal size," *Osteoporosis International*, vol. 14, no. 0, pp. 16–21, Sep. 2003, doi: 10.1007/s00198-003-1468-2.
[120] M. L. Bouxsein, "Bone quality: where do we go from here?," *Osteoporosis International*, vol. 14, no. 0, pp. 118–127, Sep. 2003, doi: 10.1007/s00198-003-1489-x.
[121] J. S. Yerramshetty and O. Akkus, "The associations between mineral crystallinity and the mechanical properties of human cortical bone," *Bone*, vol. 42, no. 3, pp. 476–482, Mar. 2008, doi: 10.1016/j.bone.2007.12.001.
[122] E. Lefèvre *et al.*, "Compositional and mechanical properties of growing cortical bone tissue: a study of the human fibula," *Sci Rep*, vol. 9, no. 1, p. 17629, Dec. 2019, doi: 10.1038/s41598-019-54016-1.

[123] K. J. Jepsen, M. B. Schaffler, J. L. Kuhn, R. W. Goulet, J. Bonadio, and S. A. Goldstein, "Type I collagen mutation alters the strength and fatigue behavior of Mov13 cortical tissue," *Journal of Biomechanics*, vol. 30, no. 11–12, pp. 1141–1147, Nov. 1997, doi: 10.1016/S0021-9290(97)00088-2.

[124] C. Wynnyckyj, T. L. Willett, S. Omelon, J. Wang, Z. Wang, and M. D. Grynpas, "Changes in bone fatigue resistance due to collagen degradation," *Journal of Orthopaedic Research*, vol. 29, no. 2, pp. 197–203, 2011, doi: 10.1002/jor.21228.

[125] H. K. Buechner, "Mountain Sheep. A Study in Behavior and Evolution. Valerius Geist," *The Quarterly Review of Biology*, vol. 49, no. 2, pp. 168–169, Jun. 1974, doi: 10.1086/408061.

[126] A. A. Farke, "Frontal sinuses and head-butting in goats: a finite element analysis," *Journal of Experimental Biology*, vol. 211, no. 19, pp. 3085–3094, Oct. 2008, doi: 10.1242/jeb.019042.

[127] A. Kitchener, "An analysis of the forces of fighting of the blackbuck (Antilope cervicapra) and the bighorn sheep (Ovis canadensis) and the mechanical design of the horn of bovids," *Journal of Zoology*, vol. 214, no. 1, pp. 1–20, Jan. 1988, doi: 10.1111/j.1469-7998.1988.tb04983.x.

[128] A. Kitchener, "Fracture toughness of horns and a reinterpretation of the horning behaviour of bovids," *Journal of Zoology*, vol. 213, no. 4, pp. 621–639, Dec. 1987, doi: 10.1111/j.1469-7998.1987.tb03730.x.

[129] P. Maity and S. A. Tekalur, "Finite Element Analysis of Ramming in Ovis canadensis," *J Biomech Eng*, vol. 133, no. 2, pp. 021009-021009–9, Jan. 2011, doi: 10.1115/1.4003321.

[130] A. Drake, T. L. Haut Donahue, M. Stansloski, K. Fox, B. B. Wheatley, and S. W. Donahue, "Horn and horn core trabecular bone of bighorn sheep rams absorbs impact energy and reduces brain cavity accelerations during high impact ramming of the skull," *Acta Biomaterialia*, vol. 44, pp. 41–50, Oct. 2016, doi: 10.1016/j.actbio.2016.08.019.

[131] D. C. Viano *et al.*, "Concussion in Professional Football: Comparison with Boxing Head Impacts—Part 10," *Neurosurgery*, vol. 57, no. 6, pp. 1154–1172, Dec. 2005, doi: 10.1227/01.NEU.0000187541.87937.D9.

[132] J. R. Kulbe and E. D. Hall, "Chronic traumatic encephalopathy-integration of canonical traumatic brain injury secondary injury mechanisms with tau pathology," *Progress in Neurobiology*, Aug. 2017, doi: 10.1016/j.pneurobio.2017.08.003.

[133] A. C. McKee *et al.*, "Chronic traumatic encephalopathy in athletes: progressive tauopathy after repetitive head injury," *J. Neuropathol. Exp. Neurol.*, vol. 68, no. 7, pp. 709–735, Jul. 2009, doi: 10.1097/NEN.0b013e3181a9d503.

[134] L. Tombolato, E. E. Novitskaya, P.-Y. Chen, F. A. Sheppard, and J. McKittrick, "Microstructure, elastic properties and deformation mechanisms of horn keratin," *Acta Biomaterialia*, vol. 6, no. 2, pp. 319–330, Feb. 2010, doi: 10.1016/j.actbio.2009.06.033.

[135] S. Lee *et al.*, "Impact testing of structural biological materials," *Materials Science and Engineering: C*, vol. 31, no. 4, pp. 730–739, May 2011, doi: 10.1016/j.msec.2010.10.017.

[136] F. Bouville, E. Maire, S. Meille, B. Van de Moortèle, A. J. Stevenson, and S. Deville, "Strong, tough and stiff bioinspired ceramics from brittle constituents," *Nature Materials*, vol. 13, no. 5, pp. 508–514, Mar. 2014, doi: 10.1038/nmat3915.

[137] P.-Y. Chen, J. McKittrick, and M. A. Meyers, "Biological materials: Functional adaptations and bioinspired designs," *Progress in Materials Science*, vol. 57, no. 8, pp. 1492–1704, Nov. 2012, doi: 10.1016/j.pmatsci.2012.03.001.

[138] P. Tran, T. D. Ngo, A. Ghazlan, and D. Hui, "Bimaterial 3D printing and numerical analysis of bio-inspired composite structures under in-plane and transverse loadings," *Composites Part B: Engineering*, vol. 108, pp. 210–223, Jan. 2017, doi: 10.1016/j.compositesb.2016.09.083.
[139] Z. Wang, Y. Sun, H. Wu, and C. Zhang, "Low velocity impact resistance of bio-inspired building ceramic composites with nacre-like structure," *Construction and Building Materials*, vol. 169, pp. 851–858, Apr. 2018, doi: 10.1016/j.conbuildmat.2018.03.043.
[140] Z. Xin, X. Zhang, Y. Duan, and W. Xu, "Nacre-inspired design of CFRP composite for improved energy absorption properties," *Composite Structures*, vol. 184, pp. 102–109, Jan. 2018, doi: 10.1016/j.compstruct.2017.09.075.
[141] N. A. Yaraghi and D. Kisailus, "Biomimetic Structural Materials: Inspiration from Design and Assembly," *Annual Review of Physical Chemistry*, vol. 69, no. 1, pp. 23–57, Apr. 2018, doi: 10.1146/annurev-physchem-040215-112621.
[142] L. K. Grunenfelder *et al.*, "Bio-inspired impact-resistant composites," *Acta Biomaterialia*, vol. 10, no. 9, pp. 3997–4008, Sep. 2014, doi: 10.1016/j.actbio.2014.03.022.
[143] X. Yang, J. Ma, Y. Shi, Y. Sun, and J. Yang, "Crashworthiness investigation of the bio-inspired bi-directionally corrugated core sandwich panel under quasi-static crushing load," *Materials & Design*, vol. 135, pp. 275–290, Dec. 2017, doi: 10.1016/j.matdes.2017.09.040.
[144] S. H. Abo Sabah, A. B. H. Kueh, and M. Y. Al-Fasih, "Bio-inspired vs. conventional sandwich beams: A low-velocity repeated impact behavior exploration," *Construction and Building Materials*, vol. 169, pp. 193–204, Apr. 2018, doi: 10.1016/j.conbuildmat.2018.02.201.
[145] G. X. Gu, M. Takaffoli, and M. J. Buehler, "Hierarchically Enhanced Impact Resistance of Bioinspired Composites," *Advanced Materials*, vol. 29, no. 28, p. 1700060, Jul. 2017, doi: 10.1002/adma.201700060.
[146] X. Yu, L. Pan, J. Chen, X. Zhang, and P. Wei, "Experimental and numerical study on the energy absorption abilities of trabecular–honeycomb biomimetic structures inspired by beetle elytra," *Journal of Materials Science*, vol. 54, no. 3, pp. 2193–2204, Feb. 2019, doi: 10.1007/s10853-018-2958-0.
[147] M. M. Peden and World Health Organization, Eds., *World report on road traffic injury prevention*. Geneva: World Health Organization, 2004.
[148] E. Olofsson, O. Bunketorp, and A.-L. Andersson, "Helmet use and injuries in children's bicycle crashes in the Gothenburg region," *Safety Science*, vol. 92, pp. 311–317, Feb. 2017, doi: 10.1016/j.ssci.2015.11.024.
[149] K. Hansen *et al.*, "Angular Impact Mitigation system for bicycle helmets to reduce head acceleration and risk of traumatic brain injury," *Accident Analysis & Prevention*, vol. 59, pp. 109–117, Oct. 2013, doi: 10.1016/j.aap.2013.05.019.
[150] S. P. Broglio, J. J. Sosnoff, S. Shin, X. He, C. Alcaraz, and J. Zimmerman, "Head impacts during high school football: a biomechanical assessment," *Journal of athletic training*, vol. 44, no. 4, pp. 342–349, 2009.
[151] K. M. Guskiewicz *et al.*, "Measurement of Head Impacts in Collegiate Football Players: Relationship Between Head Impact Biomechanics and Acute Clinical Outcome After Concussion," *Neurosurgery*, vol. 6, no. 6, 2007.
[152] P. Brolinson, S. Manoogian, D. McNeely, M. Goforth, R. Greenwald, and S. Duma, "Analysis of Linear Head Accelerations from Collegiate Football Impacts," *Current sports*

medicine reports, vol. 5, pp. 23–8, Mar. 2006, doi: 10.1097/01.CSMR.0000306515.87053.fa.

[153] B. Schnebel, J. T. Gwin, S. Anderson, and R. Gatlin, "In Vivo Study of Head Impacts in Football: A Comparison of National Collegiate Athletic Association Division I versus High School Impacts," *Yearbook of Sports Medicine*, vol. 2008, pp. 17–18, Jan. 2008, doi: 10.1016/S0162-0908(08)79112-8.

[154] S. G. Kulkarni, X.-L. Gao, S. E. Horner, J. Q. Zheng, and N. V. David, "Ballistic helmets–their design, materials, and performance against traumatic brain injury," *Composite Structures*, vol. 101, pp. 313–331, 2013.

[155] L. Vargas-Gonzalez, S. M. Walsh, and J. Wolbert, "Impact and ballistic response of hybridized thermoplastic laminates," ARMY RESEARCH LAB ABERDEEN PROVING GROUND MD WEAPONS AND MATERIALS RESEARCH DIRECTORATE, 2011.

[156] *Vicis*. Vicis, 2017.

[157] J. Baltich, C. Maurer, and B. M. Nigg, "Increased Vertical Impact Forces and Altered Running Mechanics with Softer Midsole Shoes," *PLOS ONE*, vol. 10, no. 4, p. e0125196, Apr. 2015, doi: 10.1371/journal.pone.0125196.

[158] S. L. Winter and J. H. Challis, "Classifying the variability in impact and active peak vertical ground reaction forces during running using DFA and ARFIMA models," *Human Movement Science*, vol. 51, pp. 153–160, Jan. 2017, doi: 10.1016/j.humov.2016.12.003.

[159] D. D. D'Lima, N. Steklov, S. Patil, and C. W. Colwell, "The Mark Coventry Award: In Vivo Knee Forces During Recreation and Exercise After Knee Arthroplasty," *Clinical Orthopaedics and Related Research*, vol. 466, no. 11, pp. 2605–2611, Nov. 2008, doi: 10.1007/s11999-008-0345-x.

[160] S. J. G. Taylor and P. S. Walker, "Forces and moments telemetered from two distal femoral replacements during various activities," *Journal of Biomechanics*, vol. 34, no. 7, pp. 839–848, Jul. 2001, doi: 10.1016/S0021-9290(01)00042-2.

[161] G. Giarmatzis, I. Jonkers, M. Wesseling, S. V. Rossom, and S. Verschueren, "Loading of Hip Measured by Hip Contact Forces at Different Speeds of Walking and Running," *Journal of Bone and Mineral Research*, vol. 30, no. 8, pp. 1431–1440, 2015, doi: 10.1002/jbmr.2483.

[162] A. Fong Yan, R. M. Smith, C. E. Hiller, and P. J. Sinclair, "Impact attenuation properties of jazz shoes alter lower limb joint stiffness during jump landings," *Journal of Science and Medicine in Sport*, vol. 20, no. 5, pp. 464–468, May 2017, doi: 10.1016/j.jsams.2016.09.011.

[163] H. Nevzat Özgüven and N. Berme, "An experimental and analytical study of impact forces during human jumping," *Journal of Biomechanics*, vol. 21, no. 12, pp. 1061–1066, Jan. 1988, doi: 10.1016/0021-9290(88)90252-7.

[164] M. F. Heller, J. H. Challis, and N. A. Sharkey, "Changes in postural sway as a consequence of wearing a military backpack," *Gait & Posture*, vol. 30, no. 1, pp. 115–117, Jul. 2009, doi: 10.1016/j.gaitpost.2009.02.015.

[165] M. W. Creaby and S. J. Dixon, "External Frontal Plane Loads May Be Associated with Tibial Stress Fracture," *Medicine & Science in Sports & Exercise*, vol. 40, no. 9, pp. 1669–1674, Sep. 2008, doi: 10.1249/MSS.0b013e31817571ae.

[166] L. E. Hart, "Exercise and soft tissue injury," *Baillière's Clinical Rheumatology*, vol. 8, no. 1, pp. 137–148, Feb. 1994, doi: 10.1016/S0950-3579(05)80228-6.

[167] A. Besselink, "Running Injuries: A Multi-Billion Dollar Problem With A Simple Solution," Sep. 24, 2012. http://www.allanbesselink.com/blog/smart/1086-running-injuries-a-multi-billion-dollar-problem-with-a-simple-solution (accessed Nov. 06, 2017).
[168] B. M. Nigg and B. Segesser, "Biomechanical and orthopedic concepts in sport shoe construction," *Medicine and Science in Sports and Exercise*, vol. 24, no. 5, pp. 595–602, 1992.
[169] R. Verdejo and N. J. Mills, "Heel-shoe interactions and the durability of EVA foam running-shoe midsoles," *J Biomech*, vol. 37, no. 9, pp. 1379–1386, Sep. 2004, doi: 10.1016/j.jbiomech.2003.12.022.
[170] M. Gagliardi and M. Paggi, "Long-term EVA degradation simulation: Climatic zones comparison and possible revision of accelerated tests," *Solar Energy*, vol. 159, pp. 882–897, Jan. 2018, doi: 10.1016/j.solener.2017.10.081.
[171] K. Brückner, S. Odenwald, S. Schwanitz, J. Heidenfelder, and T. Milani, "Polyurethane-foam midsoles in running shoes - impact energy and damping," *Procedia Engineering*, vol. 2, no. 2, pp. 2789–2793, Jun. 2010, doi: 10.1016/j.proeng.2010.04.067.
[172] Z. Yao, D. Wu, C. Chen, and M. Zhang, "Creep behavior of polyurethane nanocomposites with carbon nanotubes," *Composites Part A: Applied Science and Manufacturing*, vol. 50, pp. 65–72, Jul. 2013, doi: 10.1016/j.compositesa.2013.03.015.
[173] N. Mills, *Polymer foams handbook: engineering and biomechanics applications and design guide*. Elsevier, 2007.
[174] B. Notario, J. Pinto, and M. A. Rodríguez-Pérez, "Towards a new generation of polymeric foams: PMMA nanocellular foams with enhanced physical properties," *Polymer*, vol. 63, pp. 116–126, Apr. 2015, doi: 10.1016/j.polymer.2015.03.003.
[175] ASTM F1976, *Standard Test Method for Impact Attenuation of Athletic Shoe Cushioning Systems and Materials*. 2013.
[176] S. Schwanitz, S. Möser, and S. Odenwald, "Comparison of test methods to quantify shock attenuating properties of athletic footwear," *Procedia Engineering*, vol. 2, no. 2, pp. 2805–2810, Jun. 2010, doi: 10.1016/j.proeng.2010.04.070.
[177] M. R. Shorten and M. I. V. Mientjes, "The 'heel impact' force peak during running is neither 'heel' nor 'impact' and does not quantify shoe cushioning effects," *Footwear Science*, vol. 3, no. 1, pp. 41–58, Mar. 2011, doi: 10.1080/19424280.2010.542186.
[178] Q. H. Ly, A. Alaoui, S. Erlicher, and L. Baly, "Towards a footwear design tool: Influence of shoe midsole properties and ground stiffness on the impact force during running," *Journal of Biomechanics*, vol. 43, no. 2, pp. 310–317, Jan. 2010, doi: 10.1016/j.jbiomech.2009.08.029.
[179] IIHS HLDI, "General statistics," *IIHS*, 2016. http://www.iihs.org/iihs/topics/t/general-statistics/fatalityfacts/state-by-state-overview/2015 (accessed Nov. 06, 2017).
[180] G. Belingardi, A. T. Beyene, E. G. Koricho, and B. Martorana, "12 - Lightweight solutions for vehicle frontal bumper: Crash design and manufacturing issues," in *Dynamic Response and Failure of Composite Materials and Structures*, Woodhead Publishing, 2017, pp. 365–393.
[181] N. Tanlak, F. O. Sonmez, and M. Senaltun, "Shape optimization of bumper beams under high-velocity impact loads," *Engineering Structures*, vol. 95, no. Supplement C, pp. 49–60, Jul. 2015, doi: 10.1016/j.engstruct.2015.03.046.

[182] D. K. Park, C. D. Jang, S. B. Lee, S. J. Heo, H. J. Yim, and M. S. Kim, "Optimizing the shape of a bumper beam section considering pedestrian protection," *Int.J Automot. Technol.*, vol. 11, no. 4, pp. 489–494, Aug. 2010, doi: 10.1007/s12239-010-0060-y.
[183] R. Hosseinzadeh, M. M. Shokrieh, and L. B. Lessard, "Parametric study of automotive composite bumper beams subjected to low-velocity impacts," *Composite Structures*, vol. 68, no. 4, pp. 419–427, May 2005, doi: 10.1016/j.compstruct.2004.04.008.
[184] S. M. Sapuan, M. A. Maleque, M. Hameedullah, M. N. Suddin, and N. Ismail, "A note on the conceptual design of polymeric composite automotive bumper system," *Journal of Materials Processing Technology*, vol. 159, no. 2, pp. 145–151, Jan. 2005, doi: 10.1016/j.jmatprotec.2004.01.063.
[185] Z. Xiao, J. Fang, G. Sun, and Q. Li, "Crashworthiness design for functionally graded foam-filled bumper beam," *Advances in Engineering Software*, vol. 85, no. Supplement C, pp. 81–95, Jul. 2015, doi: 10.1016/j.advengsoft.2015.03.005.
[186] D20 Committee, "Test Method for Compressive Properties of Rigid Cellular Plastics," *ASTM International F1621-16*, doi: 10.1520/D1621-16.
[187] M. J. Dickson and F. K. Fuss, "Effect of acceleration on optimization of Adidas Bounce shoes," *Procedia Engineering*, vol. 13, pp. 107–112, 2011, doi: 10.1016/j.proeng.2011.05.059.
[188] A. Ingrole, A. Hao, and R. Liang, "Design and modeling of auxetic and hybrid honeycomb structures for in-plane property enhancement," *Materials & Design*, vol. 117, pp. 72–83, Mar. 2017, doi: 10.1016/j.matdes.2016.12.067.
[189] N. El-Abbasi and S. A. Meguid, "A new shell element accounting for through-thickness deformation," *Computer Methods in Applied Mechanics and Engineering*, vol. 189, no. 3, pp. 841–862, Sep. 2000, doi: 10.1016/S0045-7825(99)00348-5.
[190] P. A. Tobias and D. C. Trindade, *Applied Reliability, Third Edition*, 3rd ed. CRC Press.
[191] P. Augat, S. Schorlemmer, C. Gohl, S. Iwabu, A. Ignatius, and L. Claes, "Glucocorticoid-treated sheep as a model for osteopenic trabecular bone in biomaterials research," *Journal of Biomedical Materials Research Part A*, vol. 66A, no. 3, pp. 457–462, 2003, doi: 10.1002/jbm.a.10601.
[192] A. Nafei, J. Kabel, A. Odgaard, F. Linde, and I. Hvid, "Properties of growing trabecular ovine bone: PART II: Architectural and mechanical properties," *The Journal of Bone and Joint Surgery. British volume*, vol. 82-B, no. 6, pp. 921–927, Aug. 2000, doi: 10.1302/0301-620X.82B6.0820921.
[193] C. Rubin *et al.*, "Quantity and Quality of Trabecular Bone in the Femur Are Enhanced by a Strongly Anabolic, Noninvasive Mechanical Intervention," *Journal of Bone and Mineral Research*, vol. 17, no. 2, pp. 349–357, 2002, doi: 10.1359/jbmr.2002.17.2.349.
[194] A. Castiglioni, L. Castellani, G. Cuder, and S. Comba, "Relevant materials parameters in cushioning for EPS foams," *Colloids and Surfaces A: Physicochemical and Engineering Aspects*, vol. 534, pp. 71–77, Dec. 2017, doi: 10.1016/j.colsurfa.2017.03.049.
[195] M. R. Shorten, "Running shoe design: protection and performance," *The Royal Society of Medicine*, pp. 156–169, 2000.
[196] T. L. Milani, E. M. Henning, and M. A. Lafortune, "Perceptual and biomechanical variables for running in identical shoe constructions with varying midsole hardness," *Clinical Biomechanics*, vol. 12, no. 5, pp. 2945–300, 1997.

[197] J. Heidenfelder, T. Sterzing, and T. L. Milani, “Systematically modified crash-pad reduces impact shock in running shoes,” *Footwear Science*, vol. 2, no. 2, pp. 85–91, Jun. 2010, doi: 10.1080/19424281003781543.
[198] B. M. Nigg, H. A. Bahlsen, S. M. Luethi, and S. Stokes, “The influence of running velocity and midsole hardness on external impact forces in heel-toe running,” *Journal of Biomechanics*, vol. 20, no. 10, pp. 951–959, Jan. 1987, doi: 10.1016/0021-9290(87)90324-1.
[199] M. R. Shorten and M. I. V. Mientjes, “The effects of shoe cushioning on impact force during running,” *Proceedings of the 6th ISB Symposium. Footwear Biomechanics, University of Otago, New Zealand*, p. 2, 2003.
[200] K. K. Chawla, *Ceramic Matrix Composites*. Springer US, 1993.
[201] D. J. Stefanyshyn and B. M. Nigg, “Energy and Performance Aspects in Sport Surfaces,” *Presented at the 3rd Symposium on Sports Surfaces, University of Calgary. Online: http://www.isss-sportsurfacescience.org/downloads/documents/8P0VK79N7A_Nigg_EnergyandPerform.pdf*, pp. 31–46, 2003.
[202] M. J. Dickson and F. K. Fuss, “Optimization of directional energy transfer in Adidas bounce tubes,” *Procedia Engineering*, vol. 2, no. 2, pp. 2795–2800, Jun. 2010, doi: 10.1016/j.proeng.2010.04.068.
[203] Y. Saadlaoui, J.-L. Milan, J.-M. Rossi, and P. Chabrand, “Topology optimization and additive manufacturing: Comparison of conception methods using industrial codes,” *Journal of Manufacturing Systems*, vol. 43, pp. 178–186, Apr. 2017, doi: 10.1016/j.jmsy.2017.03.006.
[204] A. Agrawal and R. K. Dube, “Methods of fabricating Cu-Al-Ni shape memory alloys,” *Journal of Alloys and Compounds*, vol. 750, pp. 235–247, Jun. 2018, doi: 10.1016/j.jallcom.2018.03.390.
[205] C. Velmurugan, V. Senthilkumar, K. Biswas, and S. Yadav, “Densification and microstructural evolution of spark plasma sintered NiTi shape memory alloy,” *Advanced Powder Technology*, vol. 29, no. 10, pp. 2456–2462, Oct. 2018, doi: 10.1016/j.apt.2018.06.026.
[206] L. Lecce and A. Concilio, Eds., *Shape Memory Alloy Engineering for Aerospace, Structural, and Biomedical Applications*. Elsevier, 2015.
[207] T. Duerig and A. Pelton, “Ti-Ni shape memory alloys,” in *Materials Properties Handbook: Titanium Alloys*, G. Welsch, R. Boyer, and E. Collings, Eds. American Society of Metals, pp. 1035–1048.
[208] W. L. Benard, H. Kahn, A. H. Heuer, and M. A. Huff, “A titanium-nickel shape-memory alloy actuated micropump,” in *Proceedings of International Solid State Sensors and Actuators Conference (Transducers ’97)*, Jun. 1997, vol. 1, pp. 361–364 vol.1, doi: 10.1109/SENSOR.1997.613659.
[209] K. Haldar and D. C. Lagoudas, “Dynamic magnetic shape memory alloys responses: Eddy current effect and Joule heating,” *Journal of Magnetism and Magnetic Materials*, vol. 465, pp. 278–289, Nov. 2018, doi: 10.1016/j.jmmm.2018.05.107.
[210] P. Nivala, “Processing and properties of metall open-cell foams with periodic topology,” Colorado State University, 2018.

[211] P. T. Nivala and S. P. James, “Metal open-cell foams with periodic topology fabricated by spark plasma sintering,” *Materialia*, vol. 8, p. 100428, Dec. 2019, doi: 10.1016/j.mtla.2019.100428.
[212] Z. Khoo, Y. Liu, J. An, C. Chua, Y. Shen, and C. Kuo, “A Review of Selective Laser Melted NiTi Shape Memory Alloy,” *Materials*, vol. 11, no. 4, p. 519, Mar. 2018, doi: 10.3390/ma11040519.
[213] I. Shishkovsky, V. Sherbakoff, I. Yadroitsev, and I. Smurov, “Peculiar features of electrical resistivity and phase structure in 3-D porous nitinol after selective laser sintering/melting process,” *Proceedings of the Institution of Mechanical Engineers, Part C: Journal of Mechanical Engineering Science*, vol. 226, no. 12, pp. 2982–2989, Dec. 2012, doi: 10.1177/0954406212440766.
[214] I. V. Shishkovsky, L. T. Volova, M. V. Kuznetsov, Yu. G. Morozov, and I. P. Parkin, “Porous biocompatible implants and tissue scaffolds synthesized by selective laser sintering from Ti and NiTi,” *Journal of Materials Chemistry*, vol. 18, no. 12, p. 1309, 2008, doi: 10.1039/b715313a.
[215] “Running Barefoot: Biomechanics of Foot Strike.” http://barefootrunning.fas.harvard.edu/4BiomechanicsofFootStrike.html (accessed Apr. 12, 2020).
[216] “Pedobarography,” *Wikipedia*. Oct. 14, 2019, Accessed: Apr. 12, 2020. [Online]. Available: https://en.wikipedia.org/w/index.php?title=Pedobarography&oldid=921246308.
[217] Z. Wood, L. Lynn, J. T. Nguyen, M. A. Black, M. Patel, and M. M. Barak, “Are we crying Wolff? 3D printed replicas of trabecular bone structure demonstrate higher stiffness and strength during off-axis loading,” *Bone*, vol. 127, pp. 635–645, Oct. 2019, doi: 10.1016/j.bone.2019.08.002.
[218] B. J. González Riga, M. C. Lamanna, L. D. Ortiz David, J. O. Calvo, and J. P. Coria, “A gigantic new dinosaur from Argentina and the evolution of the sauropod hind foot,” *Sci Rep*, vol. 6, Jan. 2016, doi: 10.1038/srep19165.
[219] G. S. Paul, *The Princeton Field Guide to Dinosaurs*, 2nd ed. Princeton University Press, 2016.
[220] R. B. J. Benson *et al.*, “Rates of Dinosaur Body Mass Evolution Indicate 170 Million Years of Sustained Ecological Innovation on the Avian Stem Lineage,” *PLoS Biol*, vol. 12, no. 5, May 2014, doi: 10.1371/journal.pbio.1001853.
[221] J. L. Carballido *et al.*, “A new giant titanosaur sheds light on body mass evolution among sauropod dinosaurs,” *Proc. R. Soc. B*, vol. 284, no. 1860, p. 20171219, Aug. 2017, doi: 10.1098/rspb.2017.1219.
[222] G. Paul, “Determining the Largest Known Land Animal: A Critical Comparison of Differing Methods for Restoring the Volume and Mass of Extinct Animals,” *Annals of Carnegie Museum*, vol. 85, no. 4, p. 335, Dec. 2019, doi: 10.2992/007.085.0403.
[223] G. V. Mazzetta, P. Christiansen, and R. A. Fariña, “Giants and Bizarres: Body Size of Some Southern South American Cretaceous Dinosaurs,” *Historical Biology*, vol. 16, no. 2–4, pp. 71–83, Jun. 2004, doi: 10.1080/08912960410001715132.
[224] M. J. Wedel, “A giant, skeletally immature individual of Apatosaurus from the Morrison Formation of Oklahoma,” presented at the The Annual Symposium of Vertebrate Palaeontology and Comparative Anatomy, 2013, [Online]. Available: https://web.archive.org/web/20140907100443/http://svpca.org/years/2013_edinburgh/abstracts.pdf.

[225] M. J. Wedel, R. L. Cifelli, and R. K. Sanders, “Osteology, paleobiology, and relationships of the sauropod dinosaur Sauroposeidon,” *ACTA PALAEONTOLOGICA POLONICA*, vol. 45, no. 4, pp. 343–388, 2000.

[226] M. J. Wedel and R. L. Cifelli, “Sauroposeidon: Oklahoma’s Native Giant,” *Oklahoma Geology Notes*, vol. 65, no. 2, 2005, [Online]. Available: https://www.academia.edu/6341578/Sauroposeidon_Oklahomas_Native_Giant?auto=download.

[227] K. T. Bates, P. L. Falkingham, S. Macaulay, C. Brassey, and S. C. R. Maidment, “Downsizing a giant: re-evaluating Dreadnoughtus body mass,” *Biol Lett*, vol. 11, no. 6, Jun. 2015, doi: 10.1098/rsbl.2015.0215.

[228] G. P. Burness, J. Diamond, and T. Flannery, “Dinosaurs, dragons, and dwarfs: The evolution of maximal body size,” *Proc Natl Acad Sci U S A*, vol. 98, no. 25, pp. 14518–14523, Dec. 2001, doi: 10.1073/pnas.251548698.